國立成功大學
太空與電漿科學研究所
碩士論文

National Cheng Kung University
Institute of Space and Plasma Sciences
Master Thesis

由兩相對電漿噴流對撞產生之滯留電漿密度量測

Density measurement of the stagnated plasma from the collision of two counter propagating plasma jets

研究生 (Author) :劉哲宇 Che-Yu Liu
指導老師 (Advisor) : 張博宇博士 Dr. Po-Yu Chang
中華民國一百一十二年七月 July, 2023

國立成功大學

碩士論文

由兩相對電漿噴流對撞產生之滯留電漿密度量測

Density measurement of the stagnated plasma from the collision of two counter propagating plasma jets

研究生：劉哲宇

本論文業經審查及口試合格特此證明

論文考試委員：

張博宇　曲克宇

劉耀澧

指導教授：張博宇

單位主管：電漿所所長河林榮一郎

（單位主管是否簽章授權由各院、系（所、學位學程）自訂）

中 華 民 國 112 年 7 月 5 日

摘要

本論文中我們研究透過兩正向碰撞的電漿噴流產生的滯留電漿，可以用來模擬銀河系及恆星形成區等大尺度且難以研究的天文物理現象。實驗是使用 1-kJ 的高壓脈衝功率系統，並透過雷射及可見光相機系統進行量測。系統放電時可產生一個峰值約爲 123.5 kA 的脈衝電流，且上升時間約爲 1592 ns，用於驅動一對彼此相對的錐形導線陣列所組成的雙錐形導線陣列。爲了使雷射不會受系統放電所產生的電磁脈衝訊號影響，我們設計了一個八級的高壓脈衝產生器來改善我們用於觸發系統放電的多級高壓觸發系統，改善後的觸發系統的延遲時間爲 230±90 ns。最後我們透過分析雷射相機系統所拍攝的影像，得到各時間點上方電漿噴流的長度後，將其長度對應時間做線性擬合，並將線性擬合的斜率定義爲平均速度，得到的速值約爲 17.2±4 km/s。除此之外，我們透過干涉儀所拍攝的影像，得到因雷射穿過電漿而產生的相位變化圖片，求得各時間點電漿噴流的寬度變化，發現在628.8 ns時上下兩電漿噴流的寬度都減少。透過相位變化的圖片，我們可以得到電漿密度，再將其從上到下分成七個區域觀察電漿密度的變化，發現在約 600 ns後，電漿會開始推積在雙錐形線陣列的中間並形成密度約在 10^{22} 每立方公尺的滯留電漿，因此根據密度的變化以及寬度的變化，意味著電漿噴流會受到軸向壓縮的效應影響，累積在正中心。

關鍵字：錐形導線陣列，電漿噴流，正向碰撞，軸向壓縮，脈衝功率系統

Abstract

In this thesis, we study the stagnated plasma produced by two colliding plasma jets, which can be used to simulate large-scale and difficult-to-study astrophysical phenomena such as the Milky Way and star-forming regions. The experiment was performed using a 1-kJ high-voltage pulsed-power system and measured through a laser and visible light camera system. When the system discharges, it generates a pulse current with a peak value of approximately 123.5 kA and a rise time of approximately 1592 ns, which is used to drive a bi-conical-wire array consisting of a pair of conical-wire arrays facing each other. In order to prevent the laser from being affected by the electromagnetic pulse signal generated by system discharge, we designed an eight-stage high-voltage pulse generator to improve our multi-stage high-voltage trigger system. The delay of the system with the improved triggering system is 230 ± 90 ns. Finally, by analyzing the images captured by the laser camera system, we obtained the length of the plasma jet at different times. Then, we made a linear fitting to the length corresponding to different times. And we defined the slope of the linear fitting as the averaged jet speed. The averaged speed is about 17.2±4 km/s. Through the images taken by the interferometer, we can obtain the time dependent density and the width of the plasma jets. We found that the widths of the top and down plasma jets both decreased after 628.8 ns. In addition, we divide the bi-conical-wire array in seven regions from top to bottom to observe the change of the plasma density. We found that after about 600 ns, the plasma started to pile up in the middle plane of the bi-conical-wire array and formed a stagnanted plasma with a density of about 10^{22} per m^3. It suggests that the stagnated plasma not only came from the plasma jets but also from the ablated plasma from the tungsten wires of the bi-conical-wire array.

Keyword : Conical-wire array, Plasma jet, Head-on collision, Z-pinch, Pulsed-power system

致謝

很開心能夠加入成大電漿所張博宇老師的實驗室，並度過這碩班的兩年時光，非常感謝老師對我們的耐心教導，讓我不光是在面對實驗問題上的解決能力到生活上的大小事都獲益良多。另外也要感謝實驗室的學長承翰、名翔、嘉楷以及俊宇在我剛進實驗室的時候，耐心回答我的問題和給予實驗上的建議及幫助，並且常常揪團吃飯及看電影。感謝在實驗室一起度過的夥伴致賢、奕佐、奕翔、永葳、松逸及德岳，在不管是實驗還是生活上都給予我許多的幫助，在實驗不順時陪伴我聊天以及聚餐都讓我繼續堅持下去。還要感謝我圖書館的同事們，在上下班的時間帶給我許多歡樂。另外特別感謝奇異鳥這款遊戲遊玩他的同時我感覺自己也化身成了一隻快樂的奇異鳥到處快樂的遊玩，每送出一封信都有滿滿的成就感。最後感謝我的家人給予我一路成長上的幫助。

Contents

List of Figures

List of Tables

1 Introduction

We are studying the astronomical phenomenon by simulation experiments using plasma jets and stagnated plasmas in the laboratory. In this work, the tungsten plasma was generated by heated wires, pushed to the center of the conical-wire array due to the Lorentz force, and formed the plasma jet. When two plasma jets were generated by a bi-conical-wire array consisted of two identical conical-wire arrays facing each other, the stagnated plasma was generated when two plasma jets collide with each other. In this chapter, the background of simulation experiments in astrophysical physics is given. In section 1.1, the astronomical phenomenon will be introduced. In section 1.2, laboratory-astrophysics experiments will be introduced. In section 1.3, the way of generating plasma will be introduced. In section 1.4, the bi-conical-wire array will be introduced. Finally, the goal of this thesis will be given.

1.1 Astronomical phenomenon

The outflow of the plasma jet and the plasma disk generated by the collision of two plasma jets are general astronomical phenomena. They can be observed in relativistic jets, star-forming, planetary nebulae, solar winds, active galactic nucleis (AGNs), etc. The mechanism of relativistic jets generated by the AGNs and supermassive black holes is still a mystery. However, forming a relativistic jet requires an accretion disk around black hole and a strong magnetic field[2]. There are several models to describe relativistic jets. All of them consider relativistic jets getting energy from the rotating accretion disk in different ways. Figure 1(a) shows the jet generated from the center of M87. Figure 1(b) shows the magnetohydrodynamical simulation of the yellow ergo surface as a rotating black hole. Red lines show the magnetic field lines crossing through the ergo sphere, while green lines show magnetic field lines that don't cross through it. Therefore, understanding the angular momentum of the rotating plasma may help to understand the details of how the relativistic jets were generated.

(a) (b)

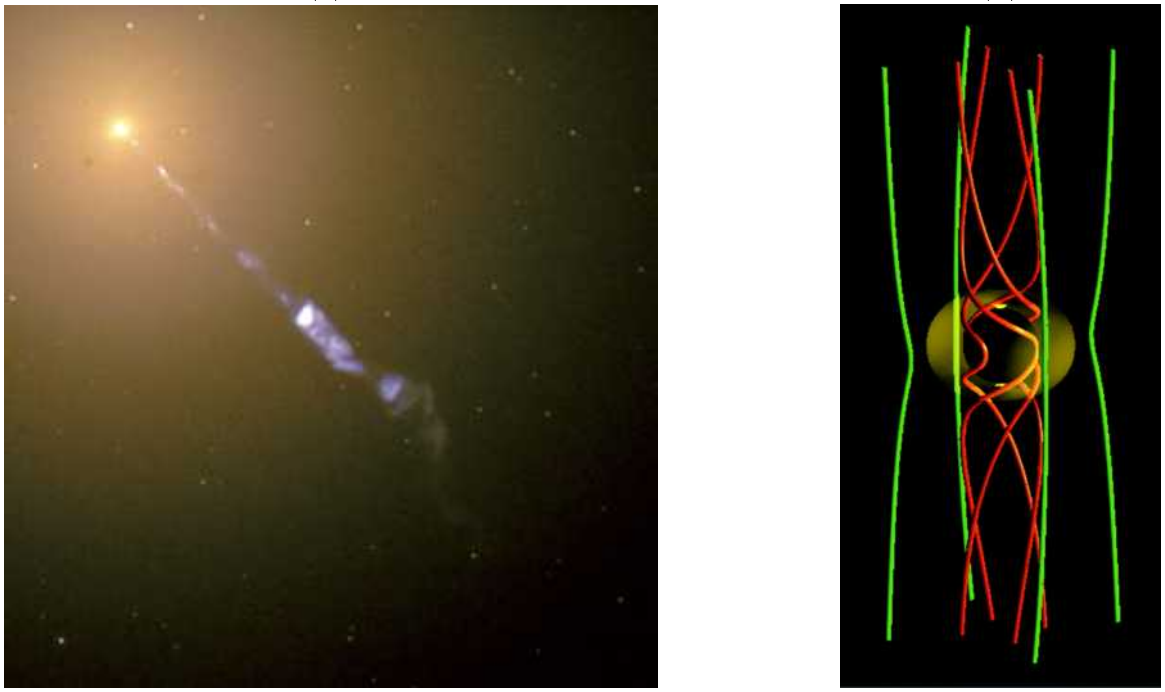

Figure 1: (a)The jet generated from M87[1]. (b)The magnetohydrodynamical simulation of roating black hole[2].

1.2 Laboratory-astrophysical experiments

Astrophysical objects are difficult to observe due to their distance being far away from the earth. Therefore, laboratory experiments are often used to simulate astrophysical phenomena. In order to make quantitative interpretations of these phenomena, we would like to use the hydrodynamic similarity between two systems. If two systems, one in the laboratory and the other one in the astrophysical phenomena, have similar geometries and Euler numbers, which is defined as

$$Eu \equiv v^* \sqrt{\frac{\rho^*}{p^*}}. \tag{1}$$

where v^*, $\rho^*$and p^* are characteristic velocity, density and pressure of two systems , respectively[14], the laboratory experiment results can be used to interpret astrophysical phenomena quantitatively. Table 1, as an example, shows the characteristic parameters in the space environment and in the laboratory condition [12, 13]. Two systems have comparable Euler numbers and are hydrodynamieally similar.

Table 1: Characteristic parameters in the space environment and the laboratory condition.[12, 13]

Physical quantities	Symbol	Value in the space	Expected value of laboratory
Scaleheight (cm)	r	7×10^8	10^{-2}
Drive velocity ($\frac{km}{s}$)	v	430	200
Timescale (s)	$\frac{r}{v}$	16	5×10^{-10}
Mass density ($\frac{g}{cm^3}$)	ρ	5×10^{-24}	10^{-3}
Pressure ($\frac{dyn}{cm^2}$)	p	2.5×10^{-11}	8×10^8
Euler number	$v\sqrt{\frac{\rho}{P}}$	19	22

1.3 Ways of generating high-energy-density plasma

Plasma is the fourth state of matter. It is basically a mixture of charge particles. There are many research areas related to plasma such as medical treatments, nuclear fusions, ion thrusters, etc. When the pressure of the plasma is higher than 1 MBar, it is called high-energy-density plasma (HEDP). There are many ways to generate HEDP. One way is using high-power lasers to ionize the target, which can be either a solid or gas. Figure 2(a) shows the plasma generated by the high-power laser of Laser Mégajoule (LMJ)[3]. Another way is using a pulsed-power system to generate plasma. A pulsed-power system uses capacitors to store energy, and release the energe in a short period of time to heat the taget. Figure 2(b) shows the discharge in the Z Pulsed-Power Facility. We are using a pulsed-power system in our experiments.

(a)	(b)
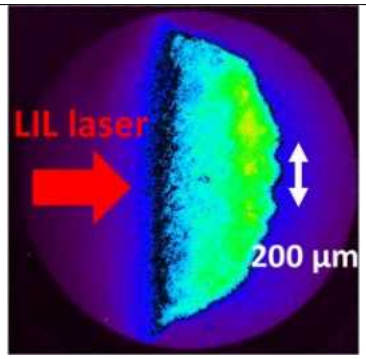	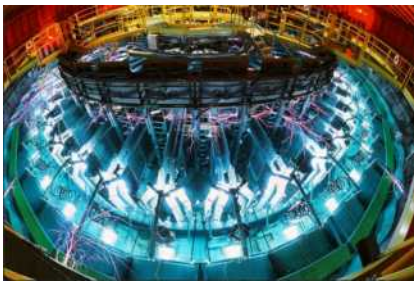

Figure 2: (a)The shock generate by high power laser[3] (b)The view of Z Pulsed Power Facility[4]

1.4 The bi-conical-wire array

The bi-conical-wire array consists of two identical conical-wire arrays facing each other. Both conical-wire arrays use four tungsten wires with 20 um in diameter. The inclination angles and

the height of the conical-wire arrays are 30 ° and ∼10 mm, respectively. Figure 3(a) shows the cross-section of the bi-conical-wire array we used in this thesis. Figure 3(b) shows the actual look of the bi-conical-wire array.

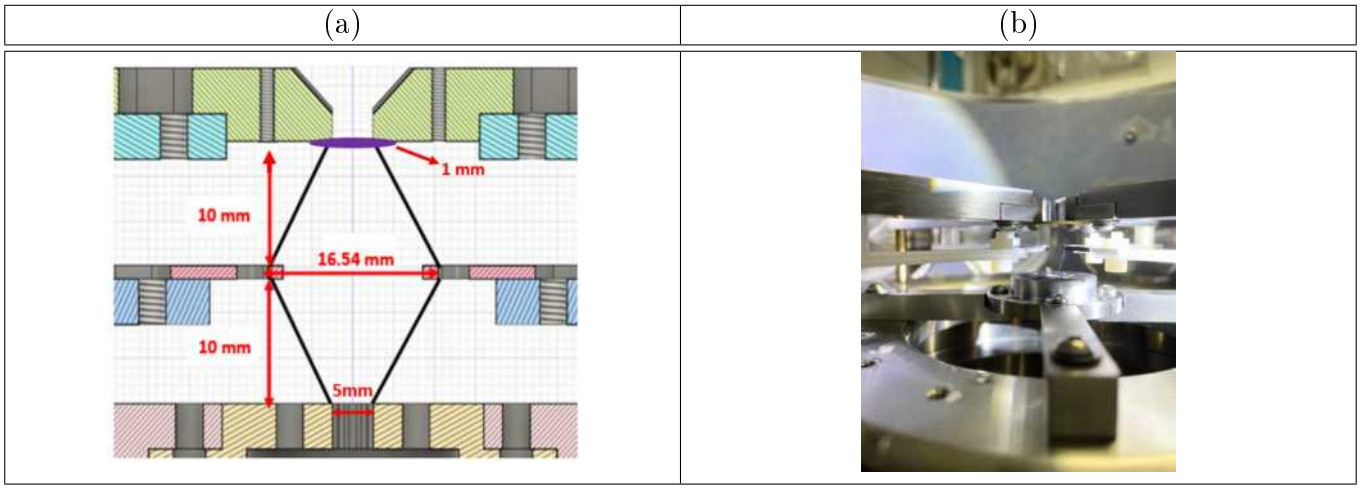

Figure 3: (a) The cross-section of the bi-conical-wire array. (b) The photo of the bi-concial-wire array.

In each conical-wire array, the radii at the bottom of both conical-wire arrays are 5 mm. When the current passes though wires, the wires are heated and ablate plasma. The current also generates an azimuthal magnetic field. The plasma is pushed toward the center due to the j×B force. When they collide at the center with an inclination angle, a plasma jet going upward is generated as shown in Figure 4. One plasma jet is generated from each conical-wire array of the bi-conical-wire array. When two plasma jets collide with each other, the plasma is stagnated at the center of the bi-conical-wire array.

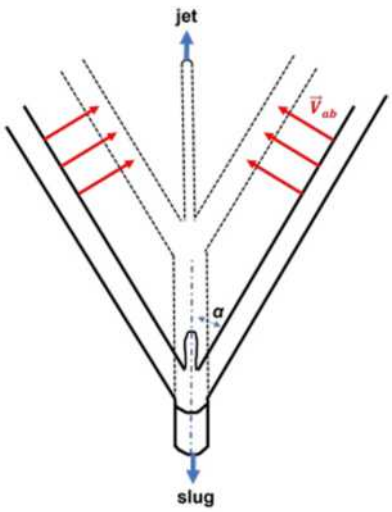

Figure 4: The schematic of generating the plasma jet[5].

1.5 The goal of the thesis

The goal of this thesis is to measure the plasma density and observe the dynamics of the non-rotating plasma jets generated by the bi-conical-wire array and how the plasma stagnates. To conduct experiments, we used the 1-kJ pulse-power system to provide a pulsed current to drive the bi-conical-wire array. In chapter 2, I will introduce the pulsed-power system and the improvement of the multistep triggering system. In chapter 3, the details of the stagnated plasma and the data analysis result will be given. In chapter 4, future work will be suggested . Finally, the summary of the thesis will be given in chapter 5.

2 The pulsed-power system

The pulsed-power system is the main experimental platform in this work. It is used to generate the plasma jet and the stagnated plasma by driving the bi-conical-wire array. In order to reduce the timing jitter of the system, I upgraded the triggering system. In section 2.1, the 1-kJ pulsed-power system will be introduced. In section 2.2, the multistep high-voltage trigger system used to trigger the pulsed-power system will be introduced. In section 2.3 the Marx generator which was the second stage of the multistep high-voltage trigger system will be introduced. In section 2.4, the eight-stage high-voltage pulse generator which reduced the jitter of the 1-kJ pulsed-power system from ±400 ns to ±90 ns is described. In section 2.5, the synchronization between the laser and the pulsed-power system will be given. It is much less complicated with the new multistep triggering system. Finally, the laser and the visible light camera system will be introduced.

2.1 The 1-kJ pulsed-power system

The 1-kJ pulsed-power system utilizes a capacitor bank with a total capacitance of 5 μF to store the energy when it is charged to the operation voltage 20 kV. The system can generate a pulsed current of 123.5 ± 1 kA with a risetime of 1592 ± 3 ns[6]. We use the multistep high-voltage trigger system to activate the rail-gap switches in the pulsed-power system. When the rail-gap switches are triggered, the current passes through the parallel-plate transmission line into the chamber, and drives the load for experiments. The load is located inside the chamber, which is pumped down to $\sim 10^{-6}$ Torr for experiments. Figure 5(a) shows the computer aided design (CAD) diagram of the pulsed-power system. Figure 5(b) shows the cross section of the pulsed-power system. The red arrows show how the current goes from the capacitor bank to the load in the chamber and comes back to the capacitor bank.

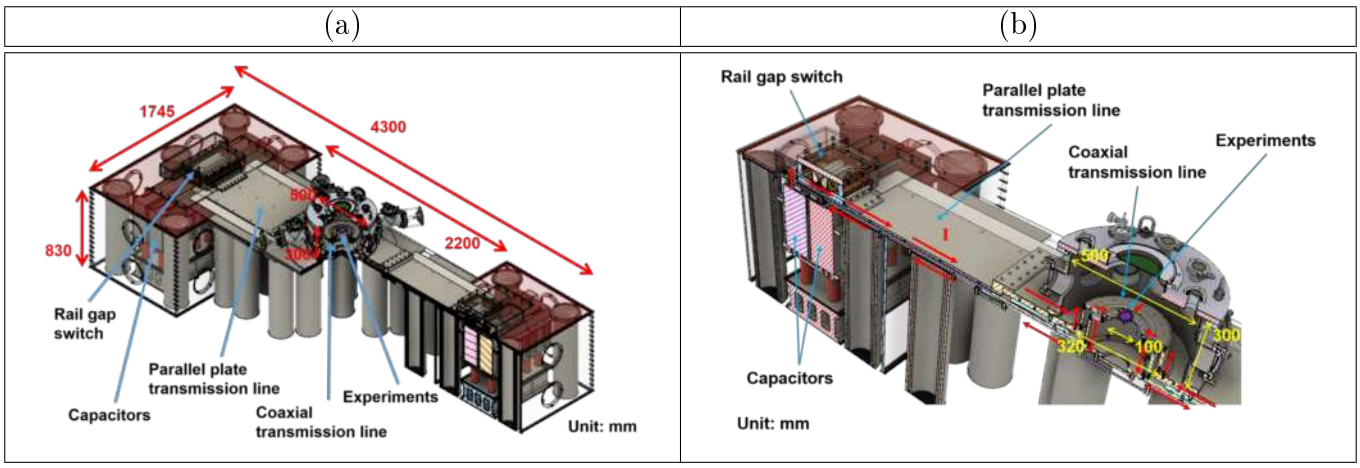

Figure 5: (a) The CAD drawing of the pulsed-power system [6]. (b) The cross section of pulsed-power system and current path[6].

2.2 The multistep high-voltage trigger system

To trigger the rail-gap switch, a trigger pulse with a falling speed higher than 5 kV/ns is needed. Therefore, the multistep high-voltage trigger system is used[7]. The original multistep high-voltage trigger system has three stages. The first stage is an optical trigger-pulse generator. The second stage is a slow high-voltage pulse generator. The third stage is a Marx generator. The slow high-voltage pulse generator can generate a negative pulse of less than -20 kV with a falling time of 55.5 $\pm$ 0.4 μs. The jitter ($\pm$0.4 μs) is much larger than the jitter of triggering the Q-switch laser, which is about 1 ns. Therefore, in order to take images with the accuracy in the order of nanosecond, we used a pickup-coil to detect the time that the pulsed-power system was triggered. Then, we used the pickup-coil signal to trigger the Q-switch laser with a proper delay as shown in Figure 6. In other words, although the whole system had a jitter of $\pm$0.4 μs, the Q-switch laser followed the pulsed-current so that the jitter between the current and the laser was in the order of 1 ns. However huge electromagnetic pulse (EMP) noise went into the laser system, probably through the pickup-coil or the delay generator. As a result, the Q-switch laser was not triggered or triggered randomly in time. Thus, we designed the eight-stage high-voltage pulse generator to replace the slow high-voltage generator. The detail of the eight-stage high-voltage pulse generator will be provided in section 2.4. As a result, the eight-stage generates a pulse about -5900 V with a falling time of 128.2 $\pm$ 1 ns. Although the pulse has lower jitter compared to the slow high-voltage pulse generator, the voltage of the pulse is higher than the pulse generated by the slow high-voltage pulse generator voltage.

Therefore, the gap of the trigatron switch in the first stage of the Marx generator was modified from 10 mm to 8.5 mm. As a result, when the signal is sent from the delay generator, it triggers the eight-stage high-voltage pulse generator. Than, output of the Marx generator produces a pulse with the falling speed higher than 5 kV/ns. Finally the rail-gap switch is triggered with a delay time of 230 $\pm$ 90 ns, where the delay time is defined as the time difference between signal sent from the delay generator to the triggering time of the rail gap switch. The updated triggering sequence now is illustrated in Figure 7.

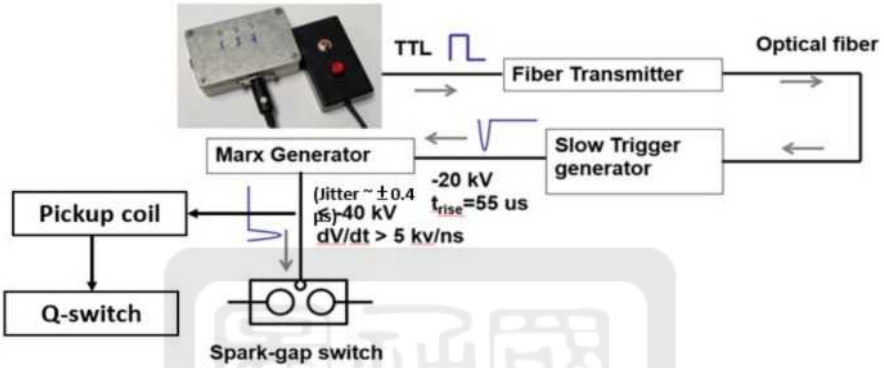

Figure 6: The trigger flow of previous multistep high-voltage trigger system.

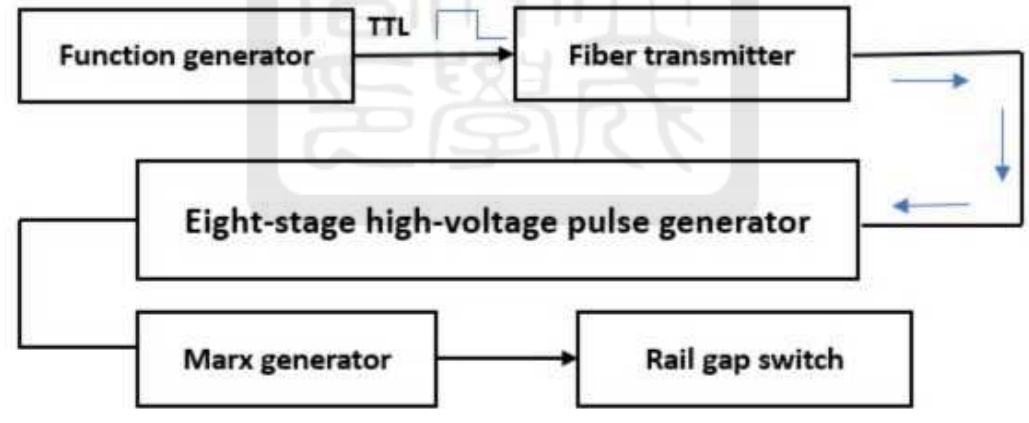

Figure 7: Trigger flow of multistep high voltage trigging system.

2.3 Marx generator

The basic principle of the Marx generator is when the capacitors in the Marx generator are being charged, they are connected in parallel. On the contrary, the capacitors are connected in series during the discharge. Therefore, it can generate a pulse with a voltage N times of the charged voltage, where N is the number of stages. The Marx generator we use has three stages and four spark-gaps as switched as shown in Figure 8(a). The gap distance in each

spark gap is 10 mm. The first spark-gap switch is a trigatron controlled by the output of the eight-stage high-voltage pulse generator or the slow trigger generator. The other switches are self-breakdown spark-gap switches. However, the minimum voltage of the pulse generated by the eight-stage high-voltage pulse generator (∼-5.9 kV) is higher than that of the slow high-voltage pulse generator (∼-20 kV). Therefore, we changed the gap distance of the trigatron in the first stage of the Marx generator from 10 mm to 8.5 mm as shown in Figure 8(b).

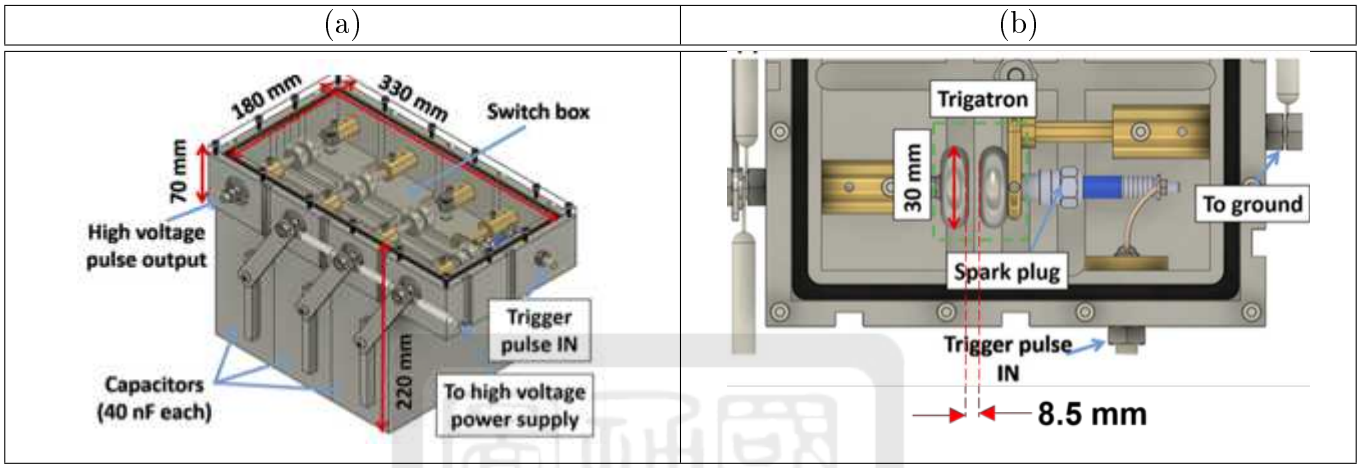

Figure 8: (a)The CAD drawing of the Marx generator.[7] (b)The CAD drawing the first stage of Marx generator.[7]

2.4 Eight-stage high-voltage pulse generator

In order to reduce the temporal jitter in experiments, the eight-stage high-voltage pulse generator was designed to replace the slow high-voltage pulse generator. The eight-stage high-voltage pulse generator consists of a pulse generator and a low-pass filter. It can generate a pulse about -5900 V with a falling time of 128 ± 1 ns.

2.4.1 Determining the required output voltage for the eight-stage high-voltage pulse generator

First, we need to know what is the breakdown voltage of the trigatron in the Marx generator. To find the trigger voltage of the trigatron in the Marx generator, I looked at the experimental data done by the former student Cheng-Han Du, which is stored in the folder:/Experiments/2020_cdu/20210916_Helmholtz coil discharge test. In this experiment, we measured the output of the slow high-voltage output shown in Figure 9.

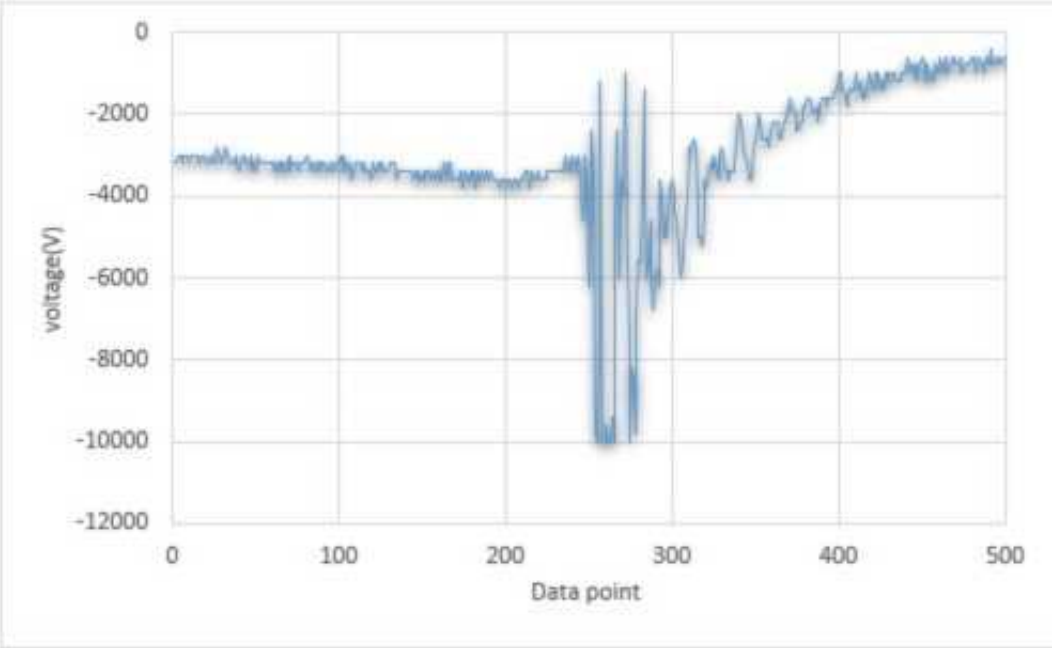

Figure 9: Output voltage of slow high-voltage generator.

We found that the breakdown always happened about after the data point 225 where lots of high-voltage noise occured. In other words, the voltage right before the high-voltage noise was the breakdown voltage of the trigatron. Therefore, we tried to obtain the voltage right before the noise started. First, we took the averaged of the data before point 225 defined as $\bar{V}$ with the standard deviation σ. Notice that data point 225 is only valid for this example. It varied a little bit between different shots. Then, we substrate three standard deviations from $\bar{V}$ and defined $V_{3\sigma} = \bar{V} + 3\sigma$. As a result, we used $V_{3\sigma}$ as the threshold to determine the noise. For any points with voltage higher than $V_{3\sigma}$, they were replaced by 1. On the contrary, if the voltage was lower than $V_{3\sigma}$, they were replaced by 0. The converted result is shown in Figure 10 and the green arrow points to the first 0 point. It is defined as the first point of the high-voltage noise. Then, the voltage of the point right before the high-voltage noise ocurred is defined as the breakdown voltage.

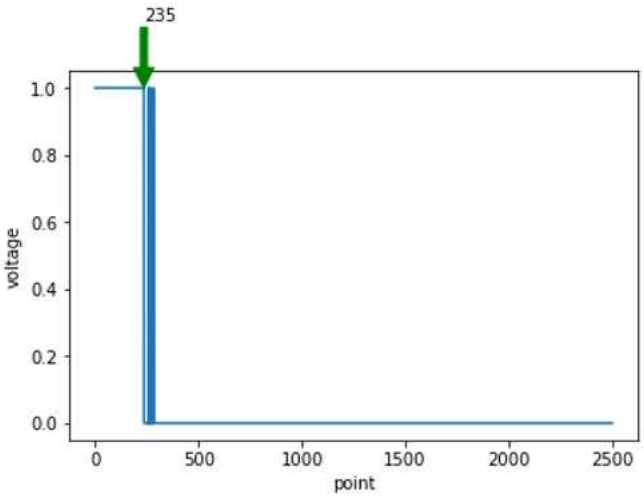

Figure 10: After transform to 1 and 0.

Therefore, we defined the first 0 point to be P_0. Then, we calculated the average of the voltages of the 10 data points prior to P_0 as the breakdown voltage V_b. Table 2 shows the averaged breakdown voltage V_b from 16 shots. Figure 11 shows the averaged breakdown voltage V_b plus three standard deviations. Ultimately, the lowest breakdown voltage was -4020 V. In other words, if the triggering pulse provide a high-voltage pulse lower than -4020 V, the trigatron is definitely activated.

Table 2: Average break down voltage from each data.

Data	V-avg(V)	Data	V-avg(V)
F0005	-3220	F0013	-2620
F0006	-3040	F0014	-3920
F0007	-2980	F0015	-3500
F0008	-4020	F0016	-3900
F0009	-3300	F0017	-3580
F0010	-3800	F0018	-3540
F0011	-3200	F0019	-3900
F0012	-4020	F0020	-3760

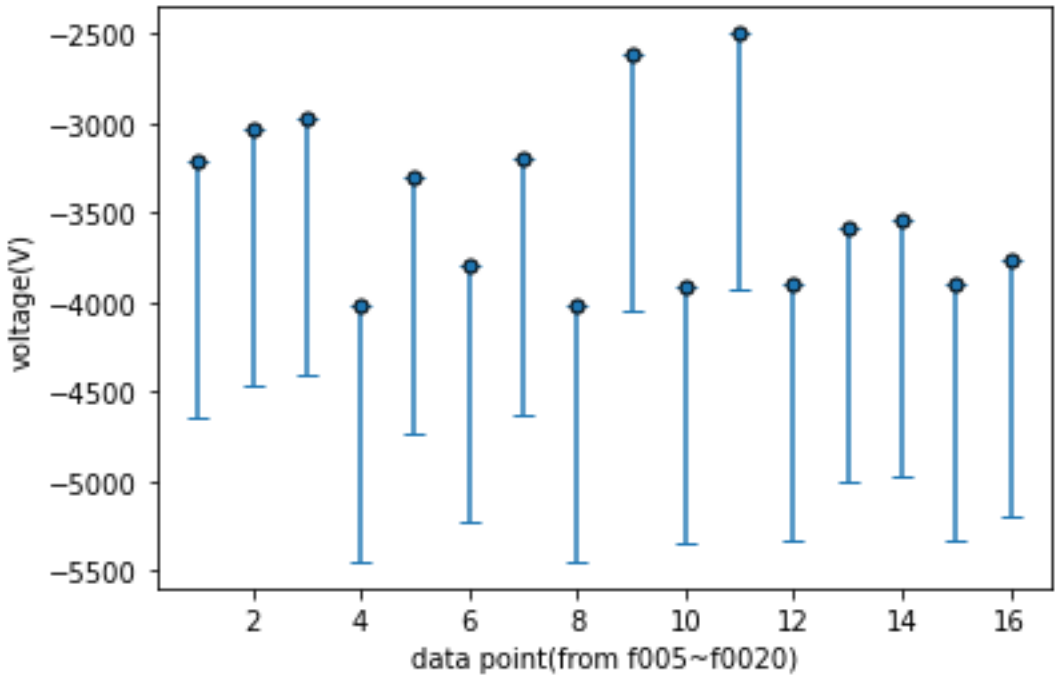

Figure 11: Average break down voltage plus three standard deviations.

2.4.2 The design of eight-stage high-voltage pulse generator

The circuit of the eight-stage high-voltage pulse generator is shown in Figure 12. It consists of eight MOSFETs ($Q_1 \sim Q_8$) as switches.[15] The capacitor C9 (11 nF) is used to store energy. It is charged to ∼8 kV. Nine 10-MΩ resistors are for the voltage divider so the voltage across the drain and the source of each MOSFET is $\frac{1}{9}$ Vcc. Therefore, capacitors C8, C7, ..., C2 are charged to $\frac{1}{9}$ Vcc, $\frac{2}{9}$ Vcc, ..., $\frac{8}{9}$ Vcc, respectively. When Q1 is activated by a 20-V trigger pulse, the voltage V1 is pulled down to 0 V. Then the capactior C8, initially charged to $\frac{1}{9}$ Vcc, will charge the effective capactior Cgs2 between the gate-source terminals of Q2 such that Vgs2 becomes 20 V. Figure 13 shows the equivalent circuit of the capactior Q2 charging the effective capactior Cgs2. When the voltage V1 in Figure 12 equals to 0, the switch S1 in Figure 13 will be closed. Then, the capactior C8 will charge the effective capactior Cgs. Finally, voltage of Cgs after the switch is closed rised from 0 to V_{cgs}.

$$V_{cgs} = V_2 \times \frac{C_8}{C_8 + C_{gs}}. \tag{2}$$

As long as V_{cgs} is larger than the required activating voltage V_{act} of the MOSFET (20 V in this case), the MOSFET is activated.

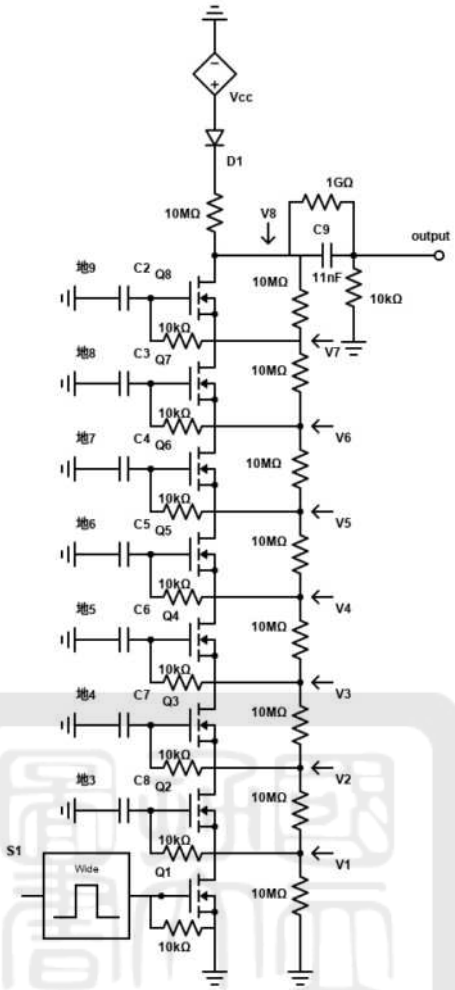

Figure 12: Eight stages pulse generator circuit.

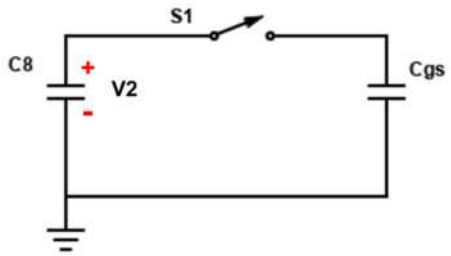

Figure 13: The equivalent circuit of the capactior chargeing the effective capactior Cgs of the MOSFET.

Consequently, Q2 is activated so that the voltage of the drain becomes the same to the source, i.e., the terminal of Q3 (V2) is pulled down to 0 V. Then, similar process happens in Q3. As a result, Q3 $\sim$ Q8 are actived sequentially. Finally, the drain terminal of Q8 (V8) is pulled down to 0 V and a negative high voltage is provided at the output. The MOSFET

we used was TSM1NB60. The capacitance of the effective capactior between the gate-source terminals is calculated by using Eq 3 where C_{iss} is 1700 , VGS_{max} is 1200, VG_{max} is 25 and C_{rss} is 25 depend on the MOSFETs.

$$C_{mos} = C_{iss} + (\frac{VGS_{max}}{VG_{max}} \times C_{rss}). \tag{3}$$

As a result, we can calculated the capacitance C2 to C8 by using Eq 4 where V_i is the voltage depends on which stage, V_{act} = 20 V is the voltage the effective capactior of MOSFET will be charged.

$$C_i = \frac{C_{mos} \times V_{act}}{V_i - V_{act}}. \tag{4}$$

Table 3 shows the capacitance C2 to C8. Figure 14 shows the output of the eight-stage high-voltage pulse generator. It was a pulse with a minimum voltage less than -5 kV. The falling time was about 140 ns. However, the output had some oscillating noises.

Table 3: The capacitance of C2 to C8.

C2(pF)	C3(pF)	C4(pF)	C5(pF)	C6(pF)	C7(pF)	C8(pF)
60	30	20	15	10	9	9

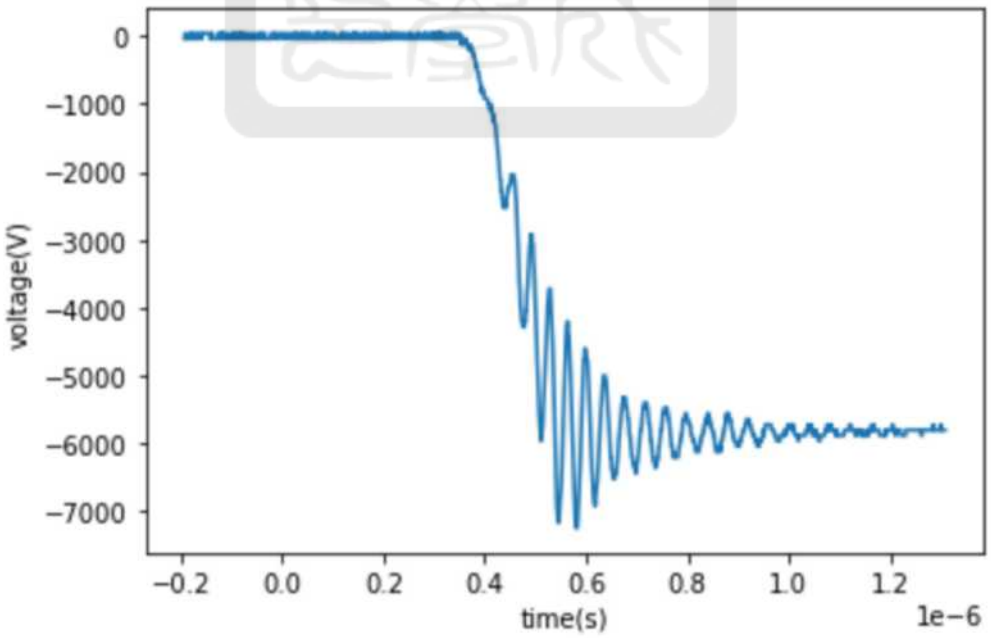

Figure 14: Pulse generated by eight stages pulse generator.

2.4.3 The low-pass filter of the eight-stage high-voltage pulse generator

In order to generate a smooth output using the eight-stage pulse high-voltage generator, a filter was built using a resisitor R_f and a capacitor C_f shown as Figure 15.

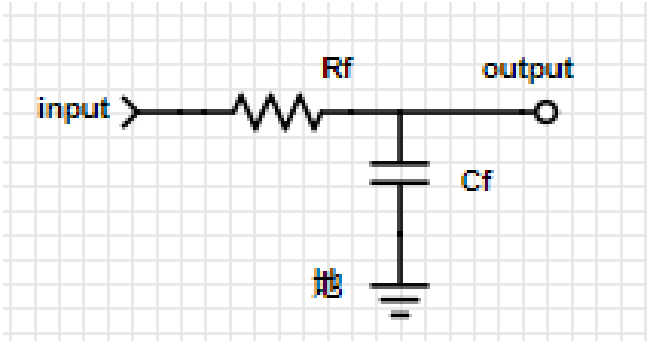

Figure 15: The circuit of low-pass filter.

For an alternating current (AC) signal, the capacitive reactance Xc can be caculated as $\frac{1}{j\omega C_f}$ where j is the imaginary number, ω is the angular frequency of the AC signal, and C_f is the capacitance. The absolute of the capacitive reactance (Xc) needs to be much smaller than R_f so that the high-frequency noise can be filtered out. The first thing to do is to find the noise frequency. Therefore, we took the Fourier transform using python to convert the data from the time domain to the frequency domain. Figure 16(a) shows the Fourier-transformed result of the voltage in Figure 14.

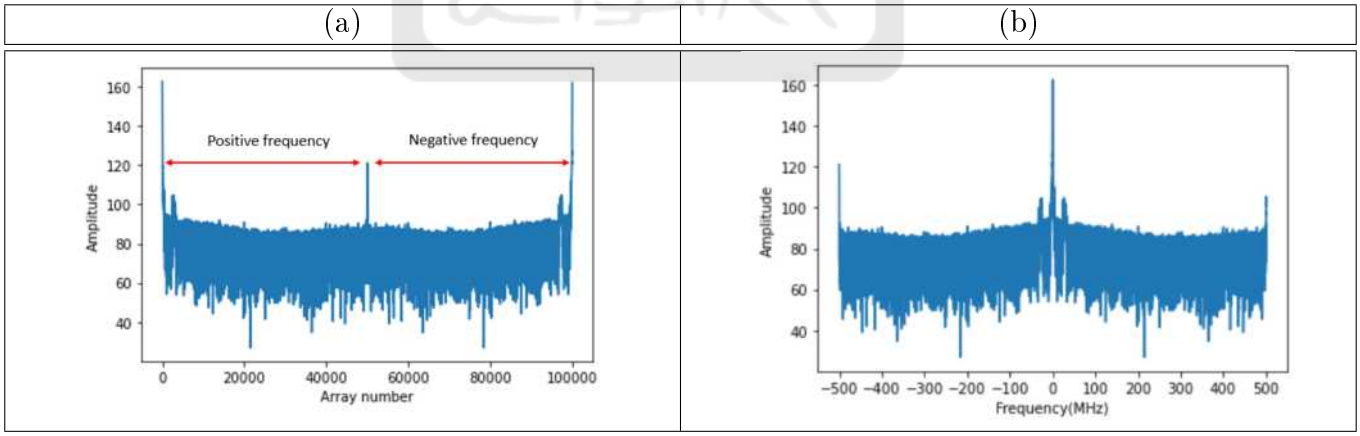

Figure 16: (a) The raw array of the Fourier-transformed signal in Figure 14. (b)We rearranged the positive and the negative frequency in to the correct position.

Since the negative and the positive frequences were in the opposited positions as shown in Figure 16(a), the negative frequence needed to be moved from the right half of the array in Fourier doman to the left half of the array as shown in Figure 16(b). Then, we can see that the noise frequency was about 30 MHz as shown in Figure 17.

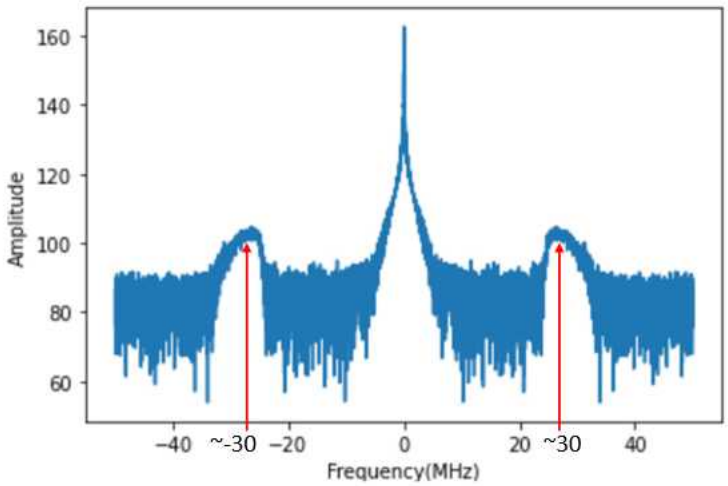

Figure 17: The noise frequency

We would like to test if the curve is smoothed when the noise is filtered out. To filter out the noise, we used a super-gaussian function as the filtering function. The super-gaussian functior is

$$filter(f) = \exp\left(-abs\left(\frac{(x-d)^e}{(2*f)^e}\right)\right). \tag{5}$$

Figure 18 shows the data with super-gaussian filter with $d = 50000$, $e = 6$, and $f = 1100$.

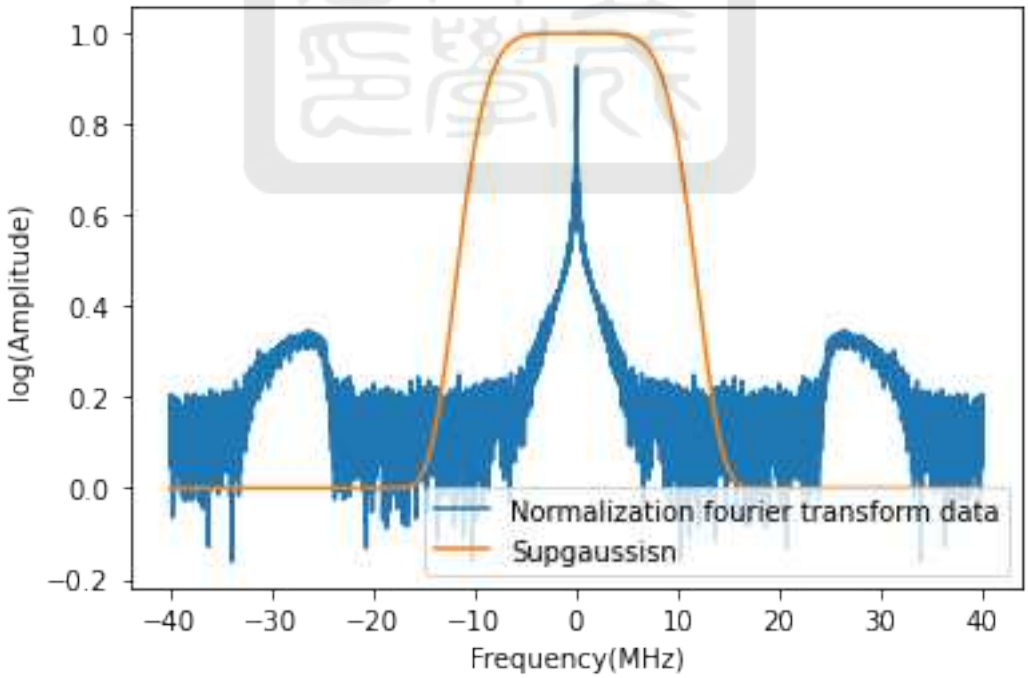

Figure 18: The normalized data with the super gaussian function.

The width of the super gaussian function in the number of array elements was set to 2200. The corresponding cut-off frequency was 10 MHz. After taking the inversed Fourier transform

of the filtered spectrum, the data was smoothed as the blue curve shown in Figure 19.

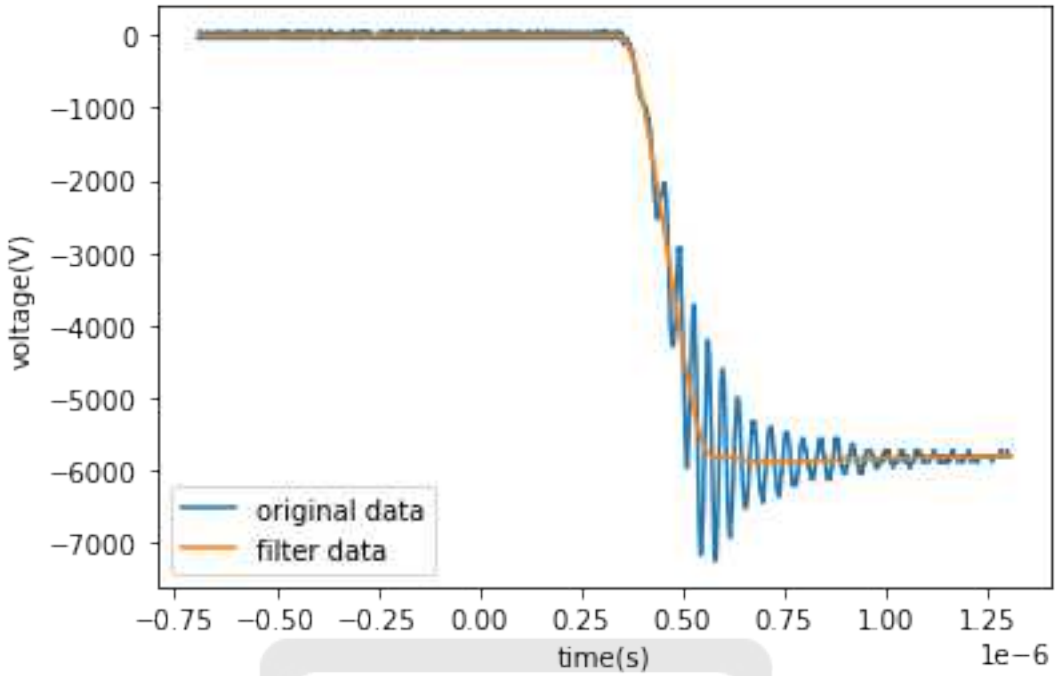

Figure 19: The data after being filtered by a super-gaussian function with a cut-off frequence of 10 MHz

The capacitance and the resistance of the filter was 1.5 pF and 1 kΩ, respatively. However, a single 1.5-pF capacitor which can withstand 6 kV was hard to be found. Therefore, the capacitor was obtained by using six 10-pF capacitors connected in series and the capacitance was 1.65 pF measured by the RLC meter. Finally, the circuit with the filter is shown in Figure 20.

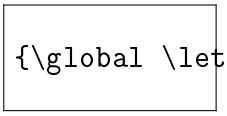

Figure 20: The circuit of eight-stage high-voltage pulse generator with low pass filter

The output of the eight-stage high-voltage pulse generator is shown as the blue curve in Figure 21(a). The moving averaged of the output is the curve in red. We defined the falling time of the pulse as the time at 10 % of the pulse to the time at 90 % of the pulse. On the other hand, the red line in Figure 21(b) fitted by Eq 6 is the sequare pulse we sent to trigger the eight-stage high-voltage pulse generator.

$$\frac{a}{2} * \pi * arctan(\frac{x-d}{b}) + c. \tag{6}$$

The blue line is the output of the eight-stage high-voltage pulse generator, which was filtered by a low-pass filter with the moving-averaged technique. The number of the averaged data point is ±5. We defined the start time of the square pulse as the time for the square pulse rise to half of the peak. Further, we defined the output time of the eight-stage high-voltage pulse generator as the time at 60 % of the pulse. Then, the delay time is defined as the output time of the eight-stage high-voltage pulse generator to the start time of the square pulse. Finally, the falling time and the delay time is given in Table 4. As a result, the jitter of the eight-stage high-voltage generator was 3 ns. The falling time of the pulse was 128.1 ± 1 ns and the delay time was 431 ± 3 ns with the minimum output voltage of -5900 ± 10 V which was averaged from the minimum voltage after fitting with moving-average. The raw data is stored in the NAS folder " Experiments\2021_cliu2\20220810八級濾波成功 ".

Table 4: The falling time and delay time of the eight-stage high-voltage pulse generator.

Falling time (ns)	Delay time (ns)	Minimum voltage (V)
126.0	427.6	-5888.0
129.0	430.6	-5888.0
129.0	432.0	-5920.0
127.0	434.2	-5904.0
130.0	435.2	-5904.0
Avg:128.1± 1	Avg:431± 3	Avg:-5900± 10

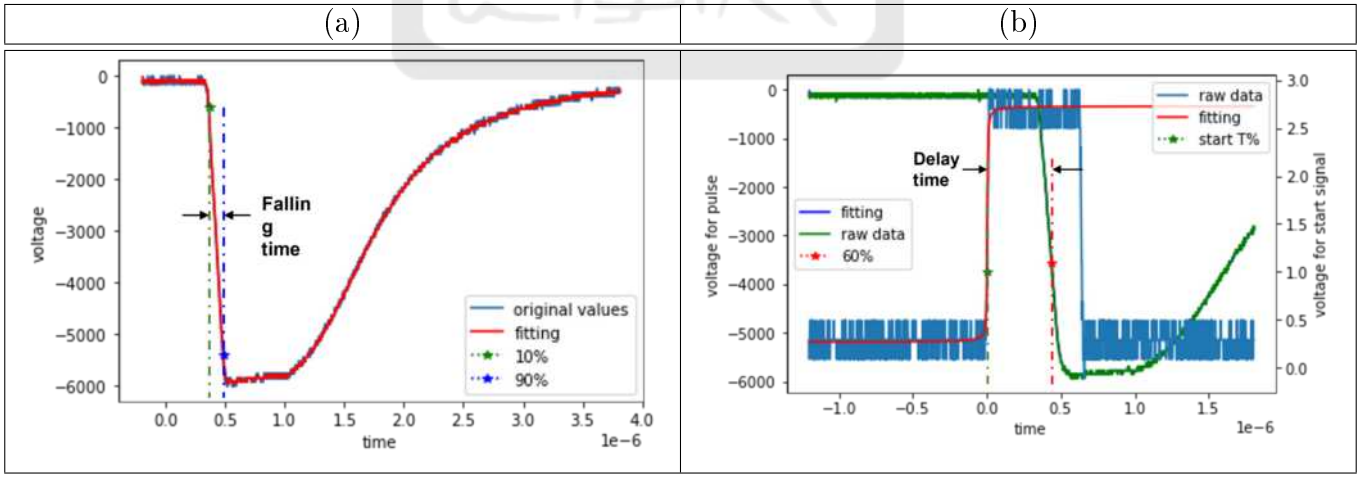

Figure 21: (a)The output with risetime. (b)The output with start signal and output

2.5 Timeline of the pulsed-power system

As a result, the pulsed-power system functions robustly. We collected all delay time between the current output and the TTL trigger pulsed as shown in Table 5. The averaged delay time

was 230 ± 90 ns. In other words, the jitter of the pulsed-power system was reduced to ±90 ns.

Table 5: The delay of the system.

Experiment data	delaytime(ns)
20230313	195
20230313	187
20230313	129
20230313	95
20230313	228
20230313	213
20230314	239
20230315	319
20230317	160
20230320	188
20230321	502
20230322	229
20230324	192
20230328	233
20230329	250
20230330	166
20230407	232
20230411	308

To trigger the pulsed-power system, we use a delay generator to generate two delay signals. One is for triggering the laser. The other one is for triggering the pulsed-power system. In order to provide a stable laser output, the flashlamp of the laser needs to flash in 10 Hz. In addition, to provide a fixed laser intensity, the Q-switch signal needs to be 370 μs after each flash. Further, the shutters of camera open 15 seconds during each shot, the laser can only be triggered once. Therefore, the delay generator needs to operate in External & single-shot mode. The trigger flow is shown in Figure 23. When we press the Enter key of the delay generator, the single-shot mode is activated. Then, it is triggered when the first 10-Hz signal fiducial is sent from the function generator. Afterwards, one delay signal TTL 1 with a proper delay is sent to trigger the eight-stage high-voltage pulse generator, while the other delay signal TTL 2 is sent to trigger the Q-switch laser with a delay of 370 μs (Delay T2). Therefore, we can change the delay (Delay T1) of the delay signal TTL 1 to measure the different timing of the experiment. Figure shows when the laser coming out compared to the pulsed-power system current.

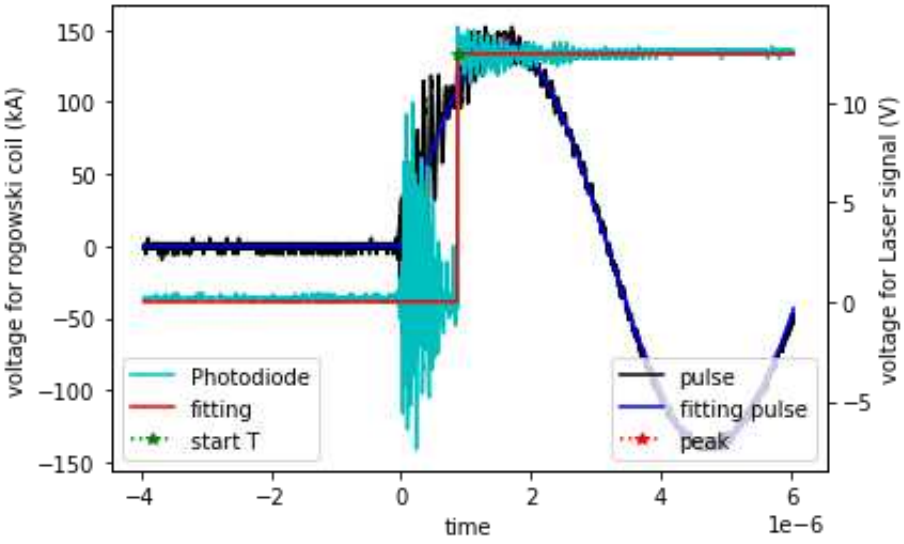

Figure 22: The laser timing compare to the pulsed-power system current.

Notice that we need to consider the delay of triggering the system defined as $T_{system} = 230 \pm 90\,ns$. Hence we can define the actual delay between the two delay signal as $\Delta t = Delay\,T2 - (Delay\,T1 + T_{\text{system}})$. Figure 24 shows the time relation diagram between the trigger flow.

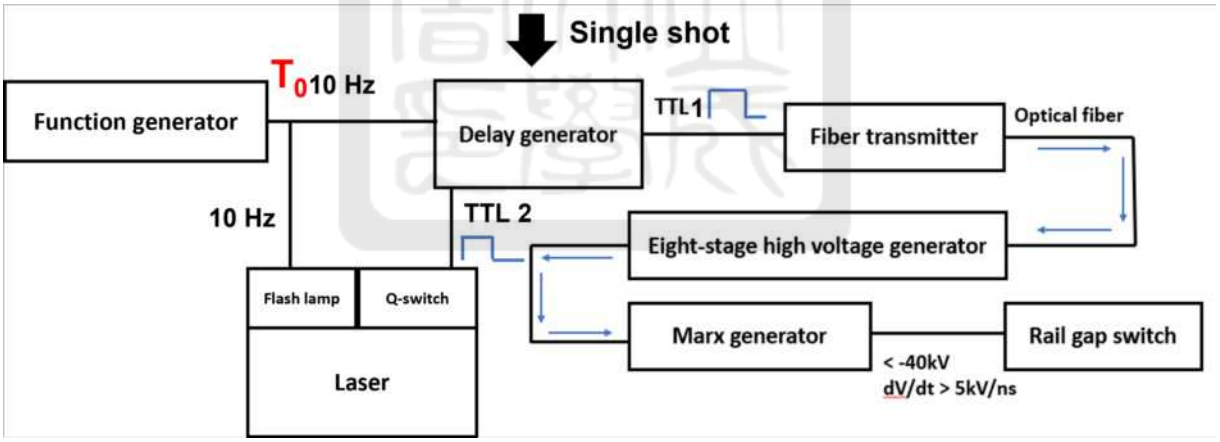

Figure 23: Trigger flow of the pulsed-power system.

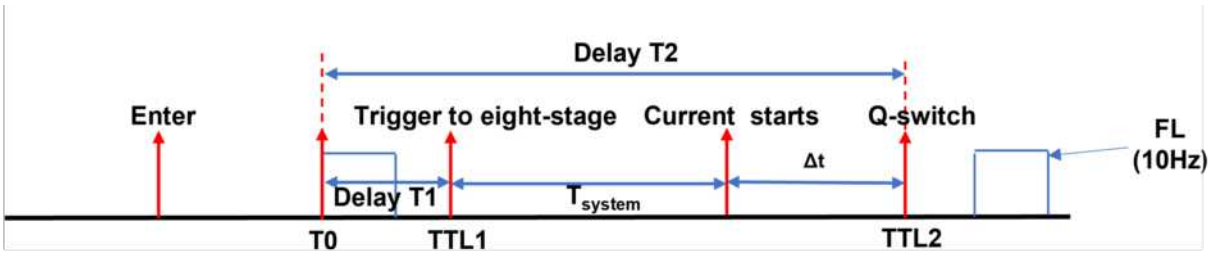

Figure 24: The time relation diagram of trigger the pulsed-power system.

2.6 Diagnostics

We used the pulsed-power system to do experiments. We used an ND:YAG Q-switch laser with a ∼5 ns pulse width at 532 nm (Quantel Q-switch 850-SLM) to take the time-resolved shadowgraphs, schlieren, and interferometer images from the side[6]. Moreover, the visible-light cameras take time-integrated images from the side and the top. All cameras are Raspberry Pi 4B with HQ camera module. They are powered by batteries and put in aluminum boxes as Faraday cages for shielding EMP noises. They are all controlled by computers via wifi. After testing, camera shutters need to open 15 second to survive from the EMP noise generated by the pulsed-power system[16].

2.6.1 Camera system

The camera system consists of two subsystems. One is the laser-camera system. The other one is the visible-camera system. Figure 25 shows the laser beam path and the positions of cameras. Figure 26 shows the photo of the diagnostics of the pulsed-power system.

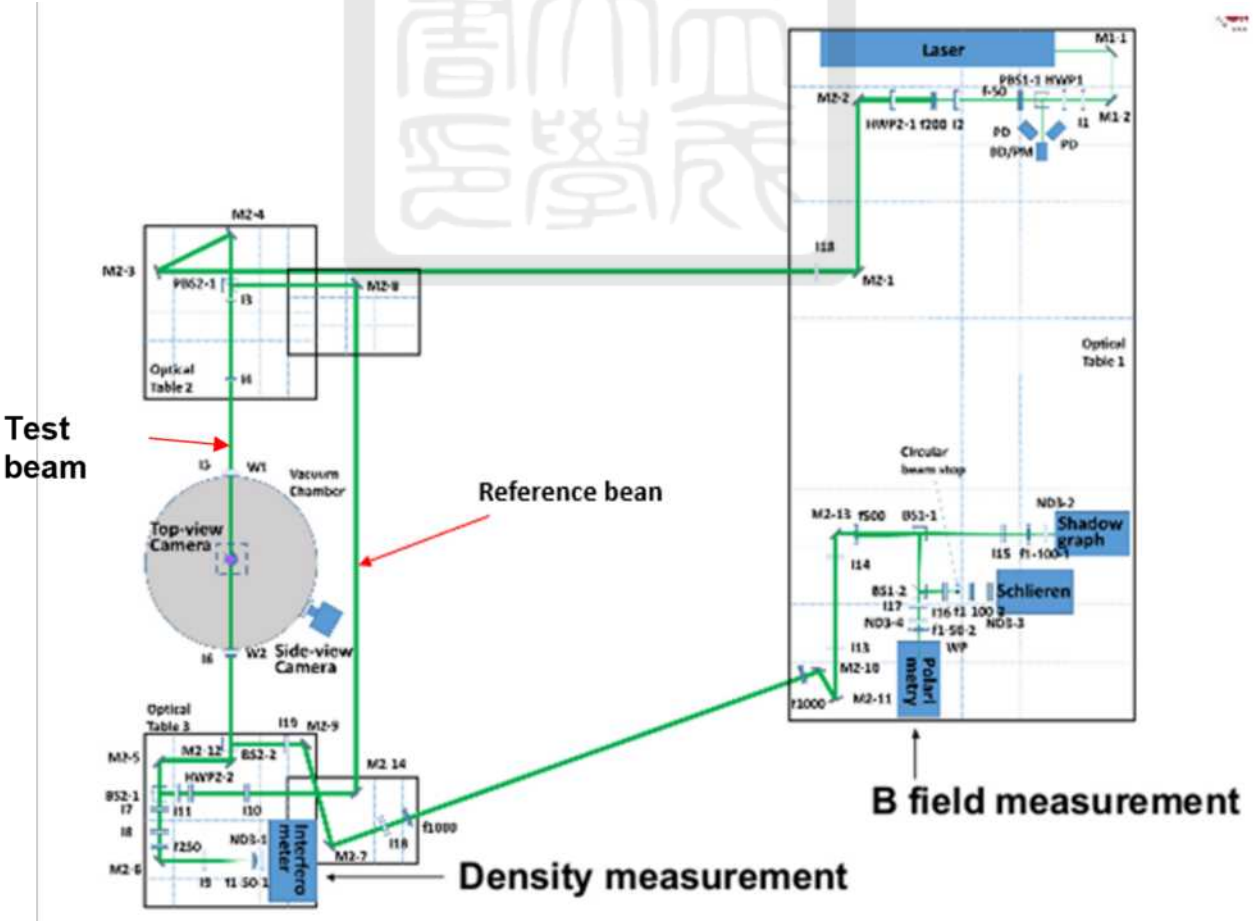

Figure 25: The laser path and the postion of the camera.[8]

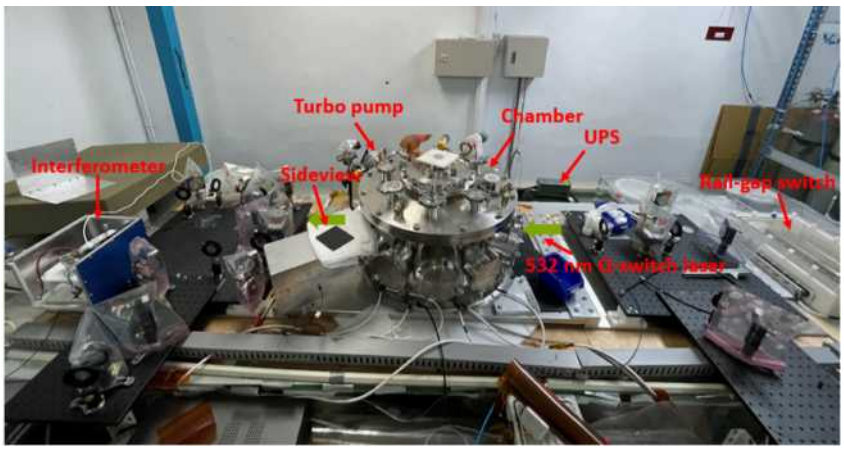

Figure 26: The diagnostics for the pulsed-power system.

Since the system still has a large jitter (±90 ns provided by section 2.5), photodiodes (PD in Figure 25) are used to measure the timing of the laser relative to the current output of the system. The laser beam is splitted into two beams called the test beam and the reference beam. The test beam is splitted into four beams after passing through the experimental region at the center of the chamber. One of the splitted test beam is recombined with the reference beam for interferometer. The other three splitted test beams are used for shadowgraph, schlieren, and polarimetry. The beam path are show in Figure 25. The interferometer is used for measuring the density of the plasma. For example, Figure 27(a) shows the image without plasma captured by the interferometer. Figure 27(b) shows the image with plasma captured by the interferometer. Density can be obtained analying by the distortion of the interferometer fringes.

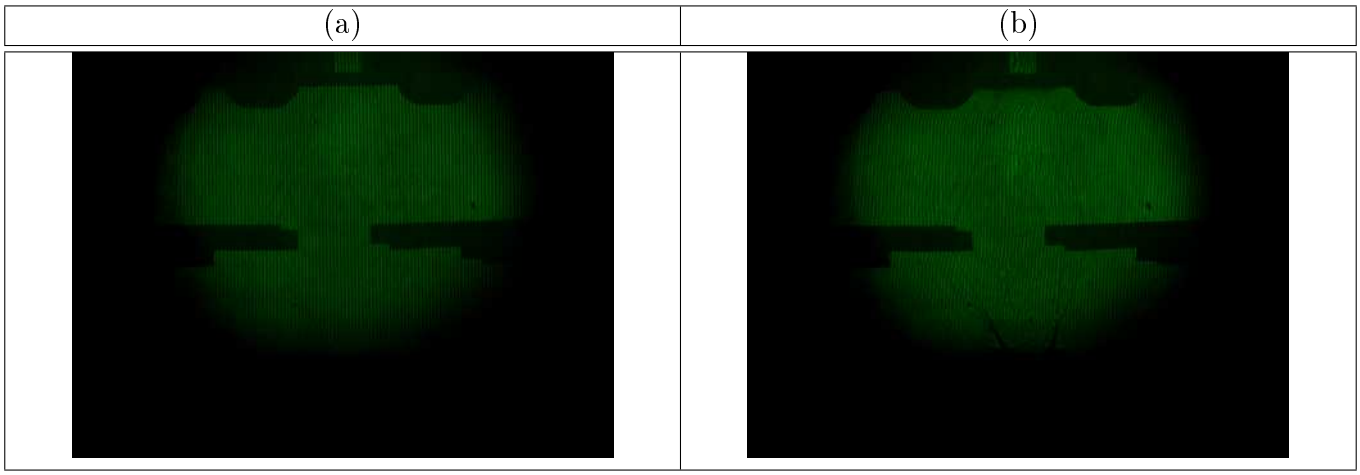

Figure 27: (a)Interferometer image without plasma on 03/14. (b)Interferometer image with plasam on 03/14.

Furthermore, the schlieren and shadowgraph are used to visualize the plasma fluid. In our schlieren camera, we would like to have the edge enhancement in all directions. Therfore, in

stead of using a knife-edge, a plastic attenuator at the focus plane is used. The high intensity laser at the focal point damaged the attenuator and made the damaged point opaque. In other words, a 360-degree knife edge was self-generated. Therefore, plasma edges in all directions are enhanced. Furthermore, the shadowgraph uses the laser as backlighter. The plasma alters the path of laser light as it passes through, causing refraction, and also absorbs a portion of the light, resulting in the formation of a shadow in the shadowgraph image. Figure 28(a) shows one example of the schlieren images taken on 2023/3/20. Figure 28(b) shows one example of the shadowgraph images taken on 2023/3/20. The brightness, exposure, contrast of the images were adjusted to +80%, +30%, and -60%, respectively, in the powerpoint.

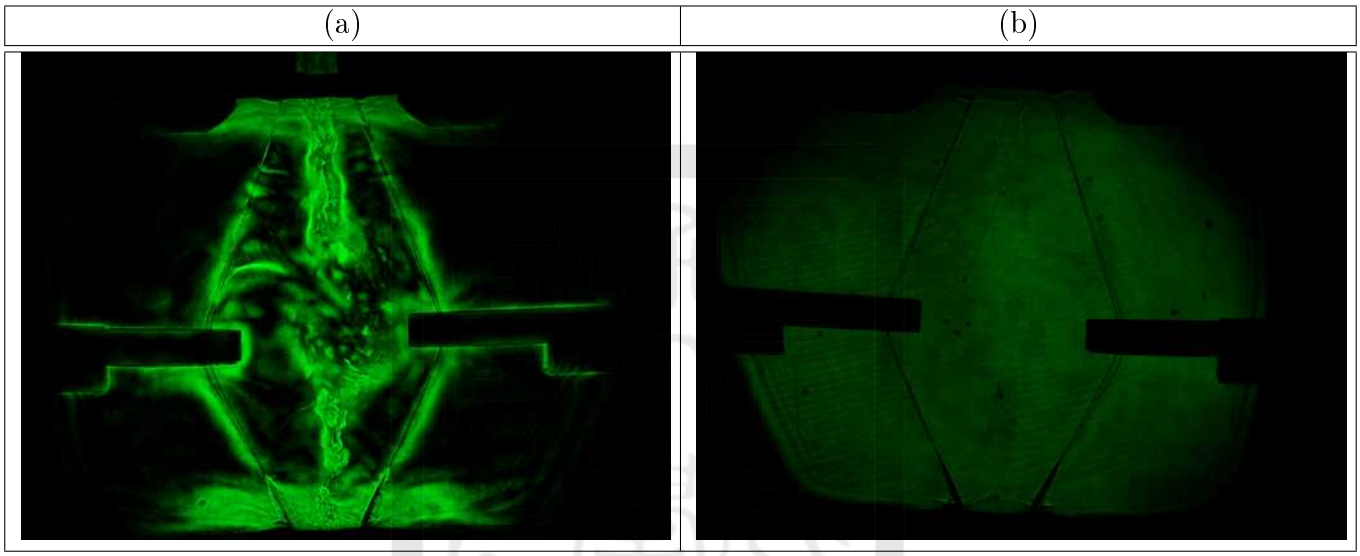

Figure 28: (a) The schlieren image with plasma. (b) The shadowgraph image with plasma.

Finally, two visible-light cameras are used. One takes time-integrated images at the middle of the chamber from the top (top-view camera). The other one takes time-integrated images from the side (side-view camera). Figure 29(a) shows the example of images taken from the top-view camera on 2023/3/29. Figure 29(b) shows the example of images taken from the side-view camera on 2023/3/29.

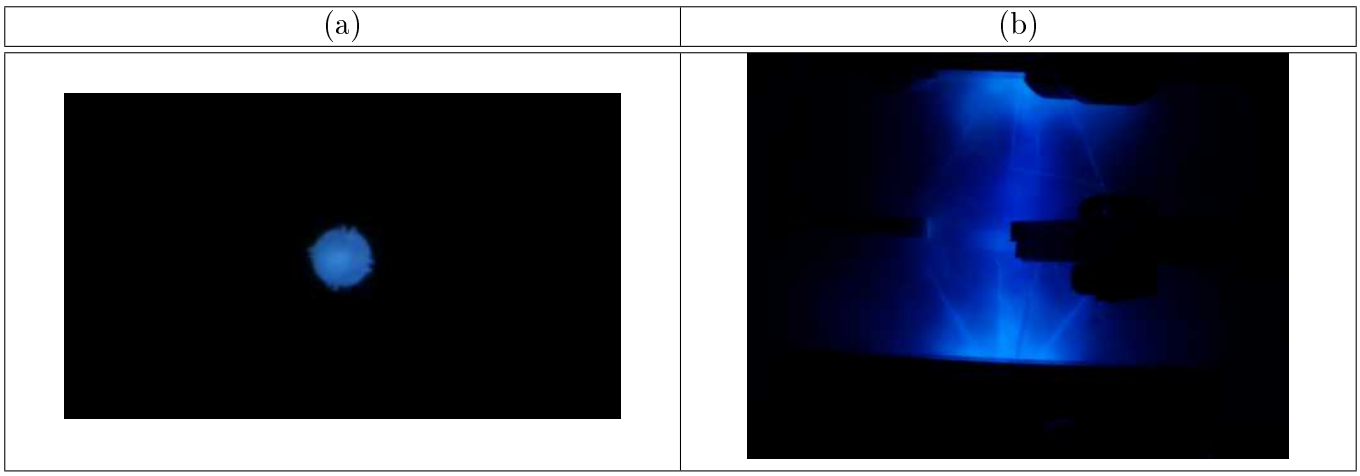

Figure 29: (a)The topview image with plasma. (b)The sideview image with plasam.

2.6.2 Analysis of the interferometer images

The intensity of the interferometer image $I(x, y)$ can be represented by Eq 7 where $I_0(x, y)$ is the averaged background intensity, $m(x, y)$ is the contrast of the fringes, v_0 is the spatial frequency of the pattern, and $\phi(x, y)$ is the phase shift. The phases shift $\phi(x, y)$ we want to retrieve is hidden in c(x,y) defined in Eq 8. Therefore, the phase shift can be caculated using Eq 9 if $c(x, y)$ is known. Since the intensity oscillates in x direction, $c(x, y)$ can be obtained using fourier transform. As shown in Figure 30, the Fourier transform of $c(x)$ is defined as $\hat{c}(f_x)$. Notice that the fourier transform is applied in x direction only. Similary, the Fourier transform of $\hat{I}(x, y)$ is $\hat{I}(f_x, y) = \hat{I}_0(f_x) + \hat{c}(f_x - v_0) + \hat{c^*}(f_x + v_0)$. Figure 30 shows how we retrieve $c(x, y)$ from $I(x, y)$ in frequency space.

$$I(x, y) = I_0(x, y) + m(x, y)cos[2\pi v_0 x + \phi(x, y)], \tag{7}$$

$$= I_0(x, y) + c(x, y)e^{i2\pi v_0 x} + c^*(x, y)e^{-i2\pi v_0 x},$$

$$c(x, y) = \frac{1}{2}m(x, y)e^{i\phi(x,y)}, \tag{8}$$

$$\phi(x, y) = \arctan(\frac{Im[c(x, y)]}{Re[c(x, y)]}). \tag{9}$$

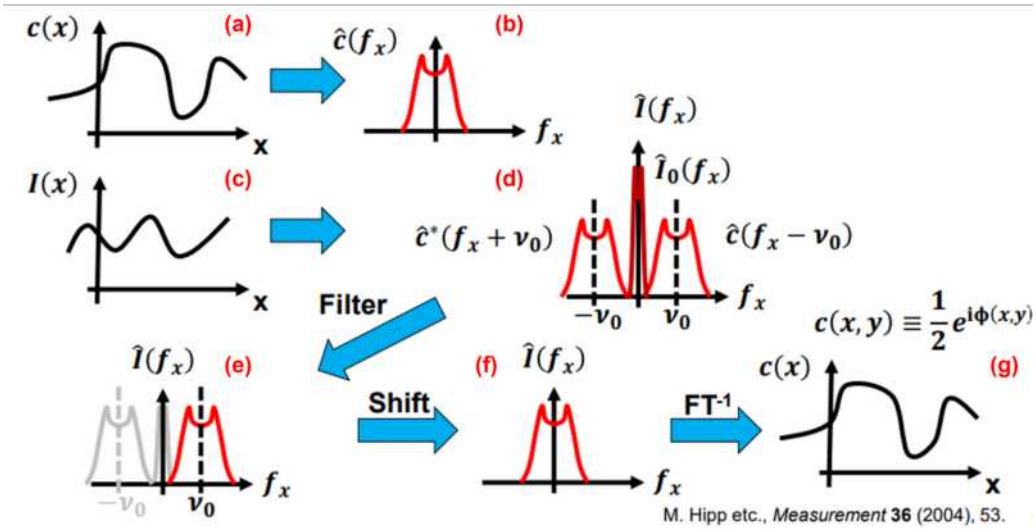

Figure 30: The meaning of taking the fourier transform[9, 10].

First, we will cut out the part in the image we do not need and transform the image to gray value. Figure 31(a) shows the orignal image of the interferometer. Figure 31(b) shows the cropped region of the interferometer image.

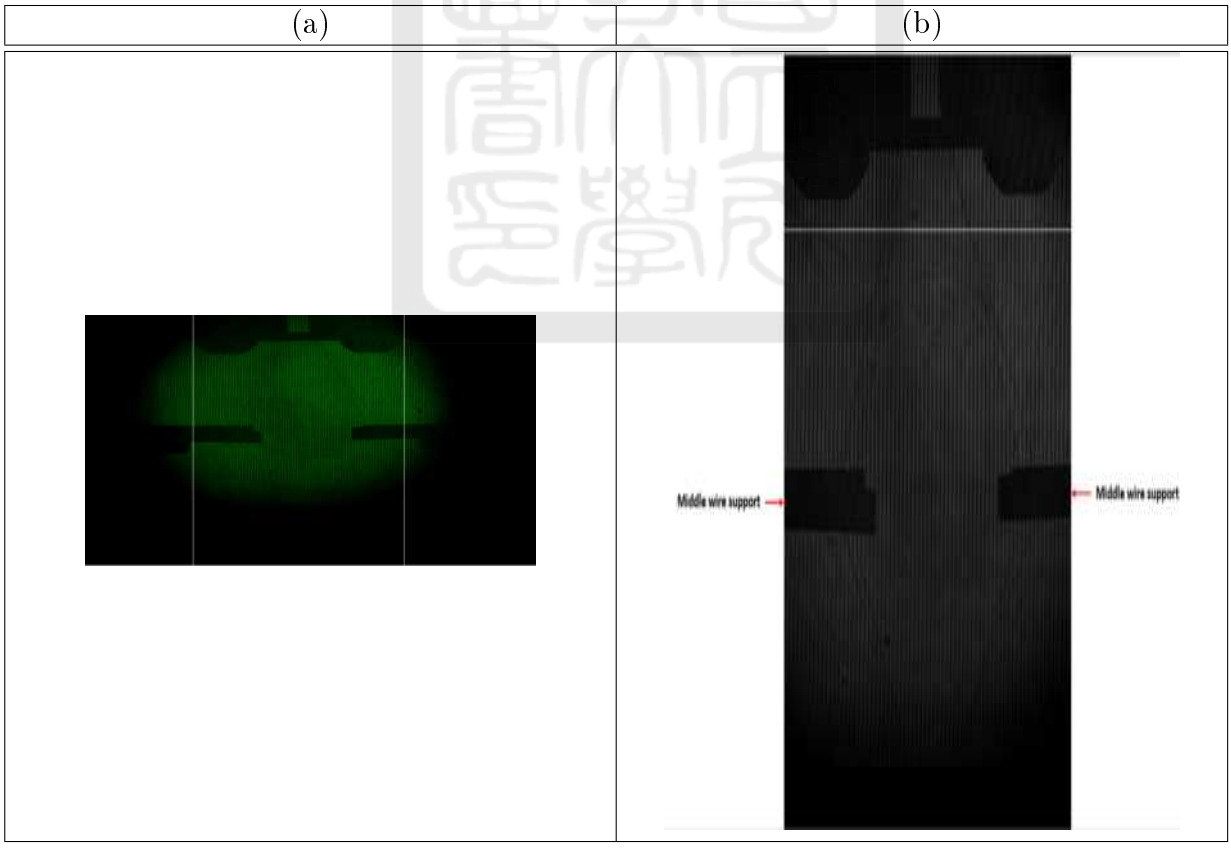

Figure 31: (a)The orignal image of the interferometer 03/30. (b)The resize image of the interferometer 03/30.

To show the process, we draw the profile along the horizontal line in Figure 31(b) as an

example. Figure 32(a) shows the intensity profile along the horizontal line. Then, we take the fourier transform of the intensity profile, shown as the blue line in Figure 32(b). Comparing to Figure 30(d), the $\hat{c}(f_x - v_0)$ can be identified. Therefore, we use a super-gaussian function as a filter as shown in the orange line in Figure 32(b) to keep the spectrum we need.

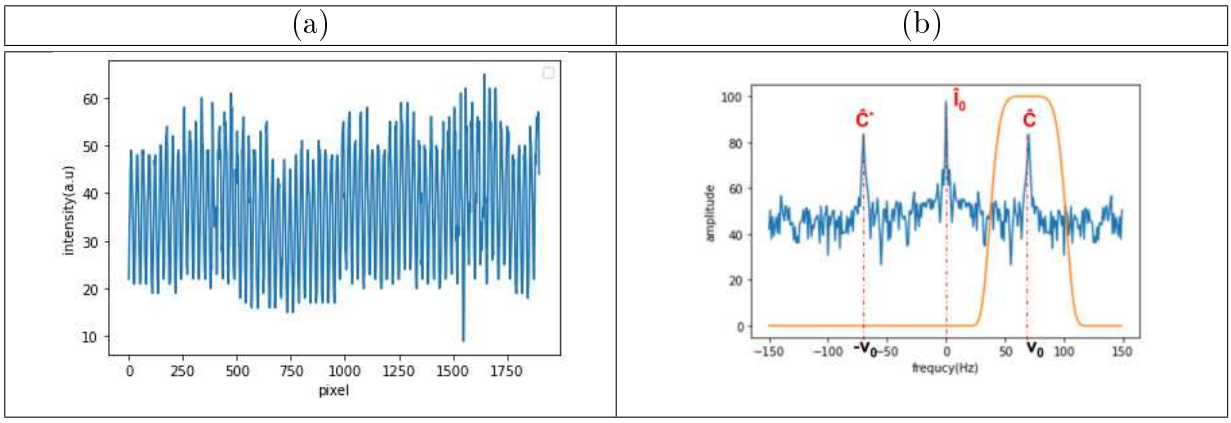

Figure 32: (a)The intensity profile. (b)The data after FFT show as blue line.

After filtering the spectrun, we shift the remaining spectrum, center at $f_0 = v_0$ to $f_0 = 0$. By taking the inverse fourier transform of the shifted function, $c(f_x)$ is obtained. Finally, the phase changes $\phi(x)$ can be obtained using Eq 9. However, the phase may jump $\pm\pi$ since arctangent function gives a number within $\pm\frac{\pi}{2}$. Therefore, if the phase jumps more than $\pm 0.9\pi$ between neighboring point, we need to add $\mp\pi$ to make it a smooth phase changes. Figure 33 shows the for loop used to adjust the phase jump over $\pm\pi$. Figure 34 shows the phase retrieved from the interferometer image.

```
for i in range(0,1898):
    coun = i+1
    a = background_data[coun] - background_data[i]
    if a < (-0.9 * np.pi):
        for i in range(coun,1898):
            background_data[i] += np.pi
    elif a > (0.9 * np.pi):
        for i in range(coun,1898):
            background_data[i] -= np.pi
```

Figure 33: The code for adjust the phase drop over $\pm\pi$.

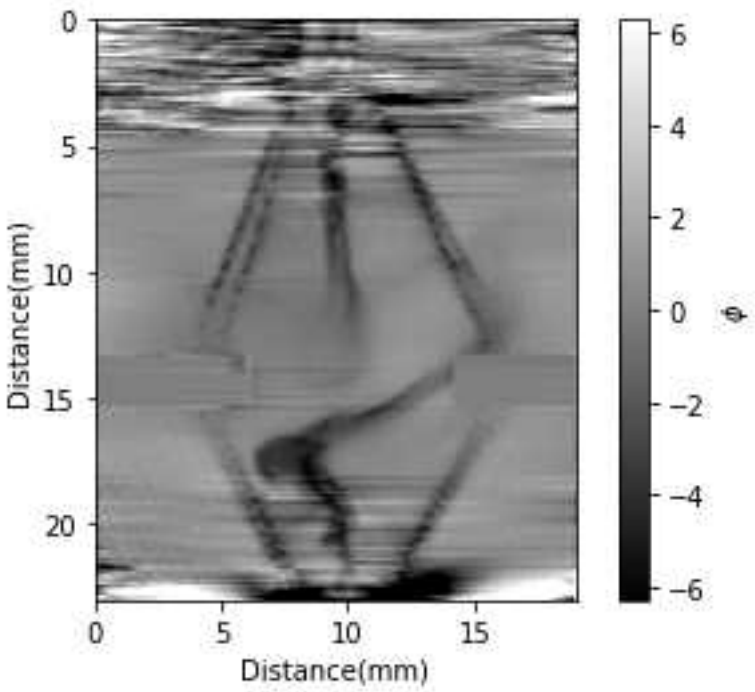

Figure 34: The interferometer image after transform to phase 03/30.

2.6.3 Filling fringers

In the cropped image shown in Figure 31(b), the middle wire support pointed by the red arrows blocked the test beam. It caused a lot of noise in data anaysis. Therefore, we artificially added an uniform fringes with the same spatial frequency to the background. To generated the uniform pattern for filling up the gap, we fitted the interference fringes right above the middle wire support by Eq 10, where b is the spatial frequency, c is the offset, and d is the background.

$$F(x) = d + 20cos(b(x + c)). \tag{10}$$

Then, we can use Eq 10 to generate the interference fringes to fill up the gap caused by the middle wire support. The result is shown in Figure 35.

Figure 35: The middle wire support cover by the generated interference fringes 03/30.

3 The stagnated plasma

We are studying laboratory and space science by the head-on collision of two plasma jets. The plasma jets were generated by the bi-conical-wire array which was driven by the pulsed-power system. The plasma jets and the stagnated plasma are used to simulate astronomical phenomena. Therefore, we measured the plasma density of the stagnated plasma at the middle of the bi-conical wire array. The measured density was 10^{22} per m^3. The bi-conical-wire array will be introduced in section 3.1. The way of analyzing the data will be explained in section 3.2. Finally, the conclusion will be covered in section 3.3.

3.1 The bi-conical-wire array

To study the head-on collision of two counter-propagating plasma jets, we used the bi-conical-wire array which consisted of two identical conical-wire arrays facing each other as shown in Figure 36(a). According to the experiments done by the former student Ming-Hsiang, Kuo, we found that the plasma jet self-emission intensity was lower after 10 mm[13]. Therefore, we changed the height of each conical-wire array from 15 mm to 10 mm. Both conical-wire arrays shared the same four tungsten wires with 20 μm in diameter. The inclination angles and the height of the conical-wire array were 30° and 10 mm, respectively. The plasma was generated by the Ohmic heating when currents flew though the tungsten wires. Then, the plasma was pushed toward the center of the conical-wire-array due to the Lorentz force and form the plasma jet at the center as shown in Figure 36(b). Figure 37 shows the computer-aided-design (CAD) drawing of the bi-conical-wire array with the current path shown in red arrows. Figure 38 shows the CAD drawing of the cross-section of the bi-conical-wire array. The engineering drawing of the bi-conical-wire array is shown in Appendex 1.7. Figure 39(a) shows the image of the bi-conical-wire array before being imploded from the side-view camera. Figure 39(b) shows the time-integrated self-emission image of the bi-conical-wire array during the implosion from the sideview camera. Figure 39(c) shows the time-integrated self-emission image of the bi-conical-wire array during the implosion from the to-pview camera. Figure 40 shows the schlieren images taken at different time during the implosion. Figure 41 shows the phase changes calculated from interferometer images at different time during the implosion. The analysis method of interferometer images were given in section 2.6.2 and 2.6.3. We are

studying the dynamics of the plasma jets and the stagnated plasmas when two plasma jets collide.

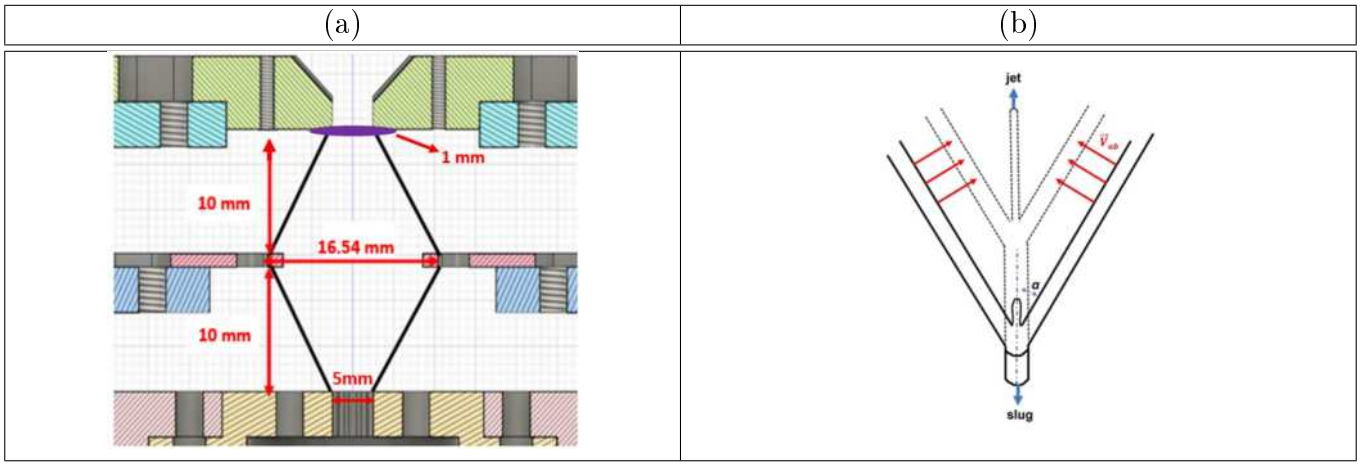

Figure 36: (a)The cross section of the bi-conical-wire array. (b)The schematic of generating the plasma jet[5].

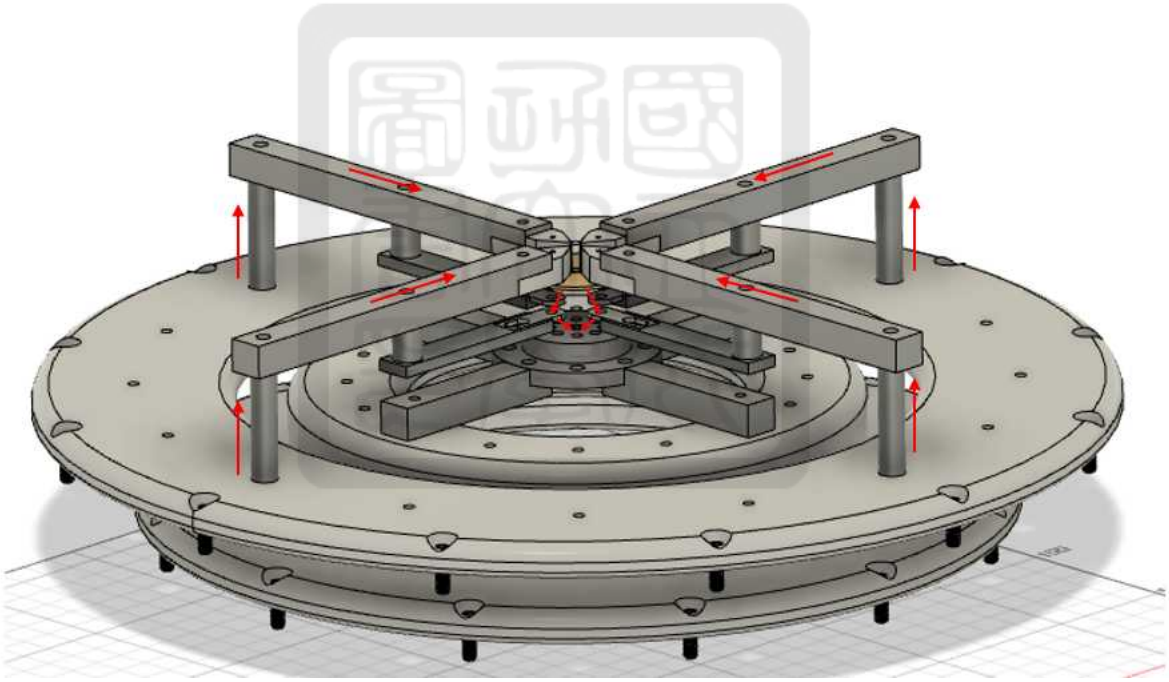

Figure 37: The bi-conical-wire array with current path.

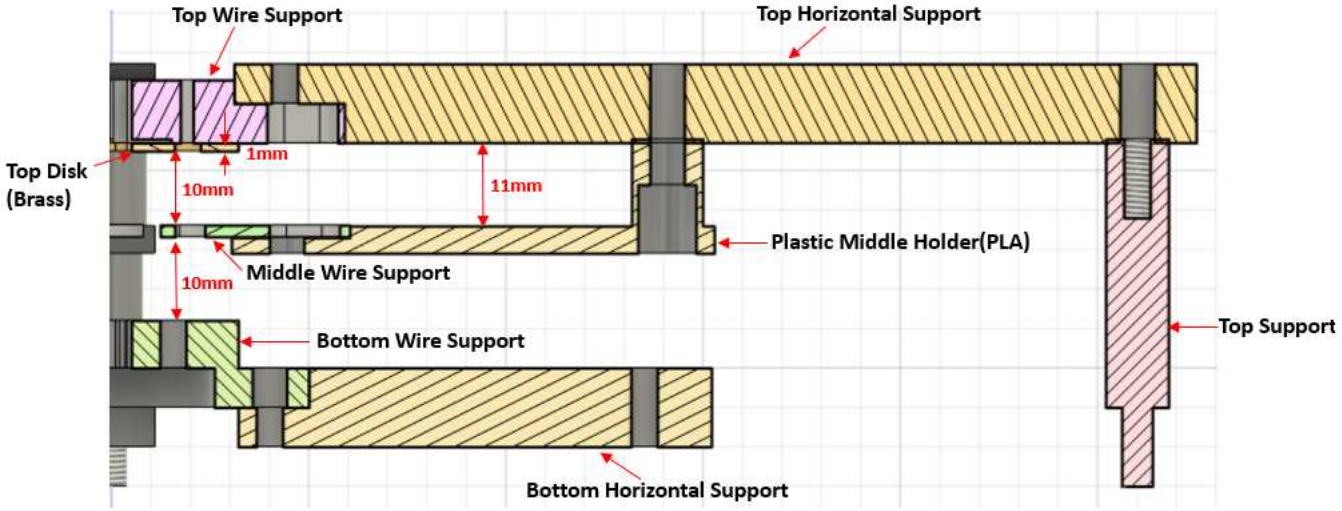

Figure 38: The CAD drawing cross-section of the bi-conical-wire array structure.

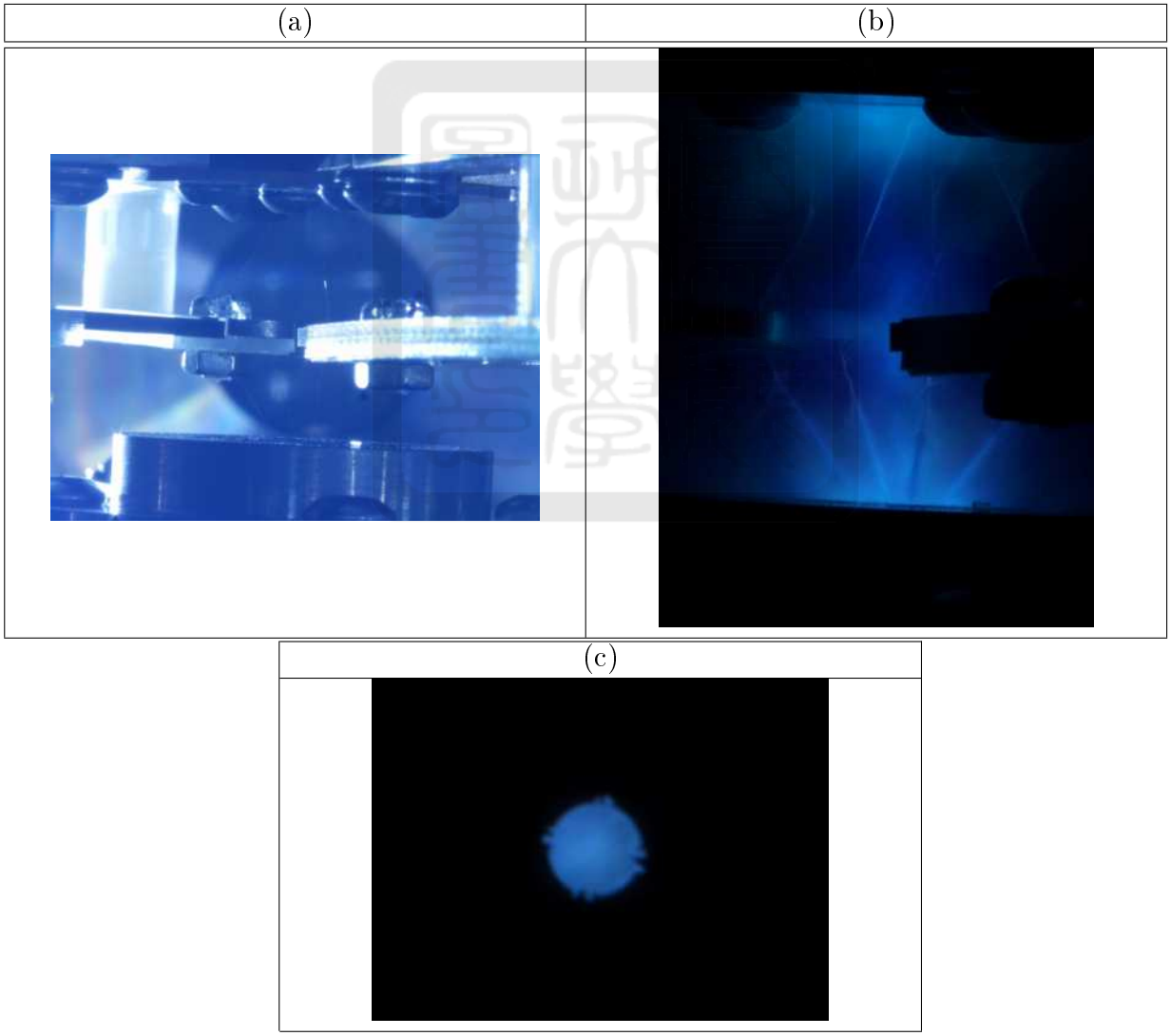

Figure 39: (a) The bi-conical-wire array from sideview camera. (b) The bi-conical-wire array with plasma from sideview camera. (c) The image from the topview camera.

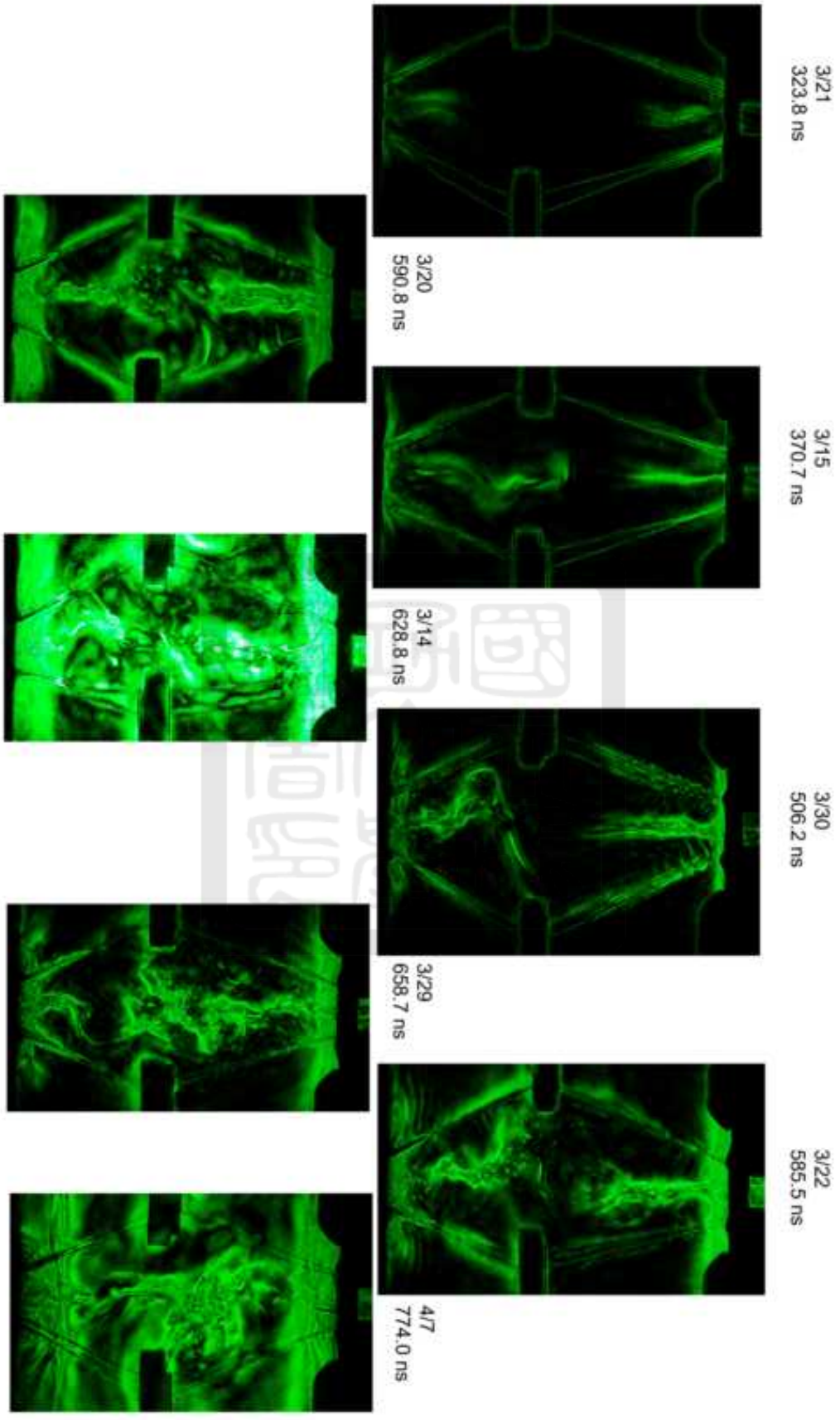

Figure 40: The schlieren images in different timing of the bi-conical-wire array.

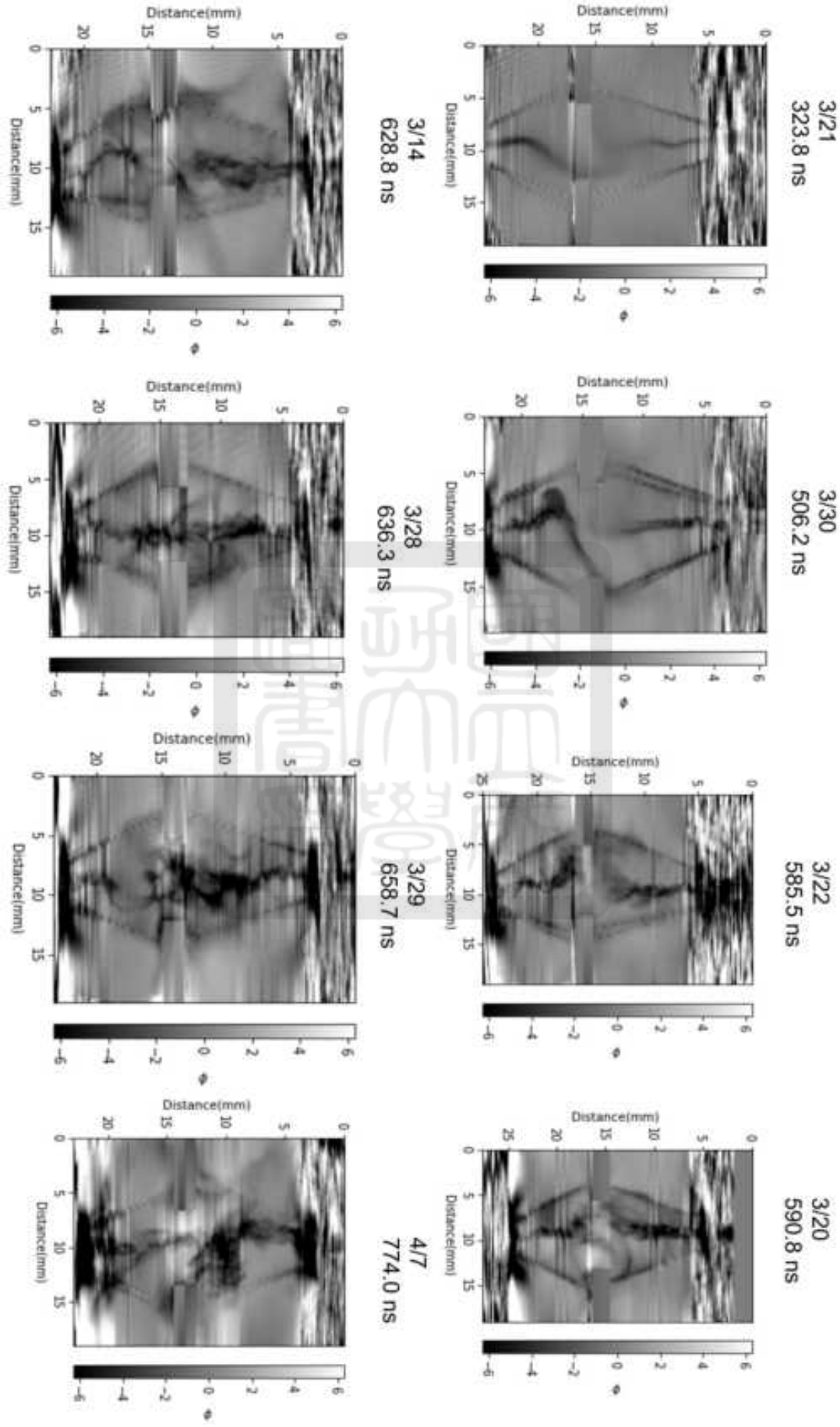

Figure 41: The phase different image of the bi-conical-wire array.

3.2 Data analysis

To understand details of the plasma jets and the stagnated plasmas, we took images of the interferometer, schlieren, and shadowgraph images at different time as shown in Figure 40 and 41. The interferometer images were used to obtain the density of the plasma, and the schlieren images were used to analyze the traveling speed of the plasma jets. The analysis were done by using Python. One of the interferometer images is used as an example of how we analyze the data. The other analyzed results are given in appendex A.8.

3.2.1 Spatial conversion ratio

To obtain the conversion ratio between 1 pixel and mm, we need to find an object in the image that we know it's dimension as the spatial fiducial. We used the thickness of the top disk (1mm) as the fiducial. Therfore, we cut the region above and below the top disk as shown in Figure 42. The averaged profile of column 875 to 1000 (in x direction) is shown in Figure 43.

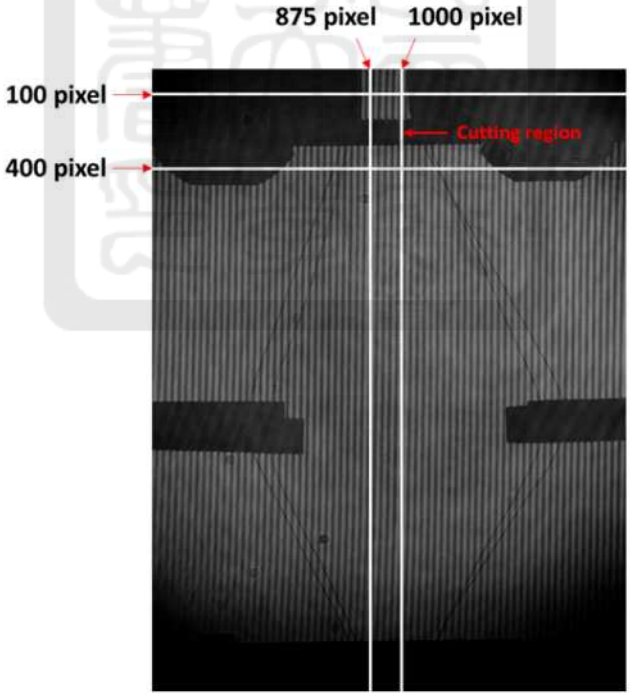

Figure 42: The cutting region of the top disk on 03/30.

Then, we fitted the profile with the high power super-gaussian function shown in Eq 11 where x_0, b, c, and d were the center of the super-gaussian function, value of the peak, width of the super-gaussian function, offsett in the y axis. Figure 43 shows the data with the fitted

curve.

$$SG(x) = d + b \times exp(-Abs\frac{1}{2}(\frac{x - x_0}{c})^{15}). \tag{11}$$

As a result, the full width half max (FWHN) of the super-gaussian function was 112.2 pixel defined as the width of the top disk. Hence, we could calculate the conversion ratio of mm to pixel number by 1 mm divided by the width of the top disk in pixels. For example, the conversion ratio in this example was 1 mm/112.2 pixel=0.0089 mm/pixel. Table 6 shows the conversion ratio of each data.

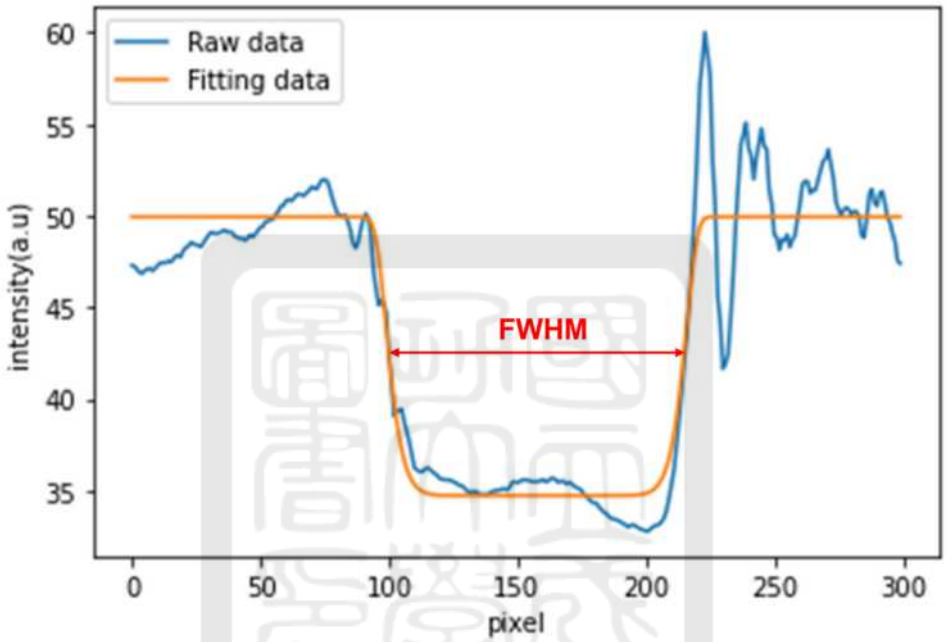

Figure 43: The fitting data of the top disk.

Table 6: The conversion ratio of each data.

data	R (mm/pixel)
0314_interferometer	0.0090
0315_schlieren	0.0081
0320_interferometer	0.0092
0320_schlieren	0.0071
0321_interferometer	0.0099
0321_schlieren	0.0070
0322_interferometer	0.0080
0322_schlieren	0.0078
0328_interferometer	0.0086
0329_interferometer	0.0073
0329_schlieren	0.0066
0330_interferometer	0.0089
0330_schlieren	0.0074
0407_interferometer	0.0077

3.2.2 Timings of the laser probing

From section 2 we knew the pulsed-power system has a jitter of 90 ns. Therefore, to know when the laser came out relative to the current in experiments, we used photodiodes to measure the laser timing and compared to the current signal measured from the rogowski coil. Figure 44 shows the photodiode signal in light blue and the current in dark blue of the shot on 3/14 as an example. The current signal from the rogowski coil was fitted by Eq 12 where a, b, c, w, and heaviside are the max value of the current, start of the current, the decay of the current, frequency of the current, a step function, respectively. It is the formula of an underdamped RLC oscillation. The signal from the photodiode signal was fitted by Eq 13 where a, b, c are the max voltage of photodiode, the start time of the photodiode signal, how fast the function rises. Eq 13 is just for smoothing.

$$I_{fit}(t) = c \times exp[-a \times (x-b)] \times sin[w \times (x-b)] \times \text{heaviside}(x-b). \tag{12}$$

$$I_{nt}(t) = a \times \frac{1}{1+exp[-c \times (x-b)]}. \tag{13}$$

As a result, the T0 (b in Eq 12) can be defined as the starting time of the current after fitting. Further, we defined the laser timing as the time for the photodiode signal rises to half of the peak (green star). Then, the measured timing $\mathrm{T_{measure}}$ can be defind $\mathrm{T_{measure}} = \mathrm{T_{Laser}} - \mathrm{T0}$.

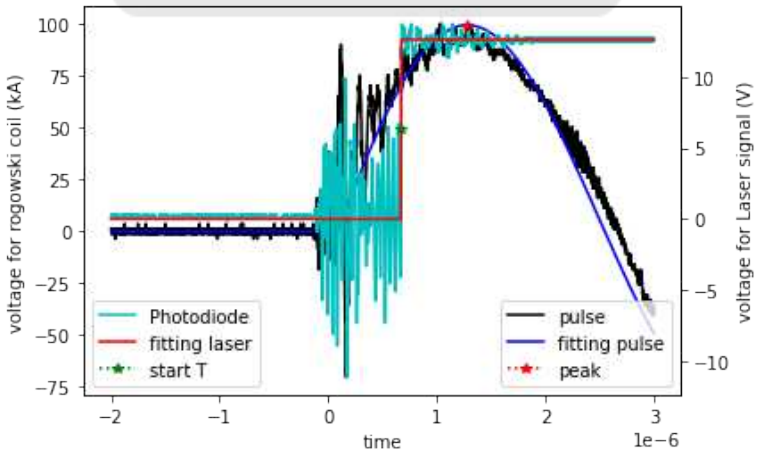

Figure 44: The relation between laser and current at 03/14.

3.2.3 The length of the plasma jet

To measure the averaged traveling speed of the plasma jet, we used the schlieren images to find out the length of the plasma jet at different time. Then, we fit the data of length versus time by a liner function and the slop is the speed. Here, we use the schlieren image taken on shot 03/30 and show in Figure 45(a) as an example of getting the length of the plasma jet. First, we need to find the postion of the top disk to be the starting point of the top plasma jet. Therefore, we average the cutting region in x direction as shown in the blue line in Figure 45(b). Then we fit the data with Eq 13. The postion of the starting point can be difined as the step function falling down to half of the peak (green point).

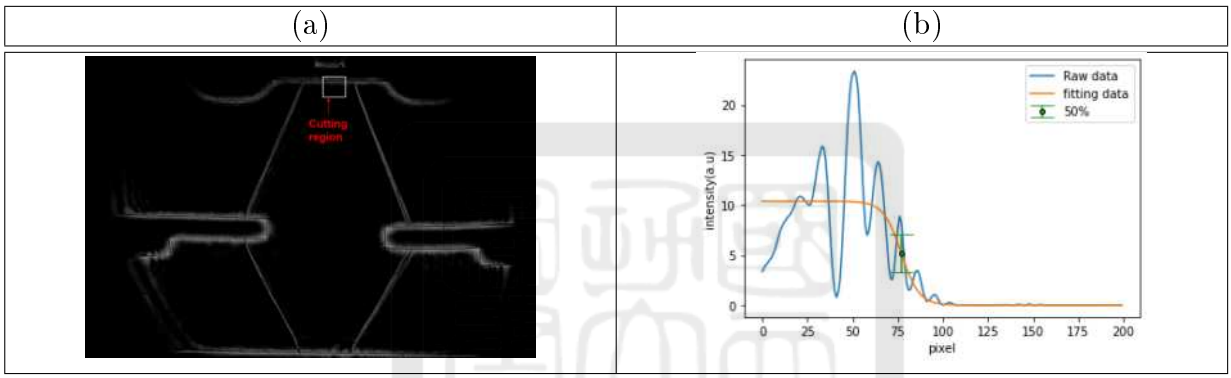

Figure 45: (a) The cutting region. (b) The data with fitting.

After getting the starting point, we cut the region wider than the jet as shown in Figure 46(a) which is the schlieren image. Then, we averaged the data in x direction and fit it by Eq 13. The fitted curve is the red line in Figure 46(b). Therfore, we used Figure 46(b) to find the end of the plasma jet defined as the step function falling down to half of the peak (green point) as the end point. Further, the jet length can be defined as end point substracted by the starting point. Notice that Figure 46(a) was the image taken right before the shot to provide a clean edge of the top disk.

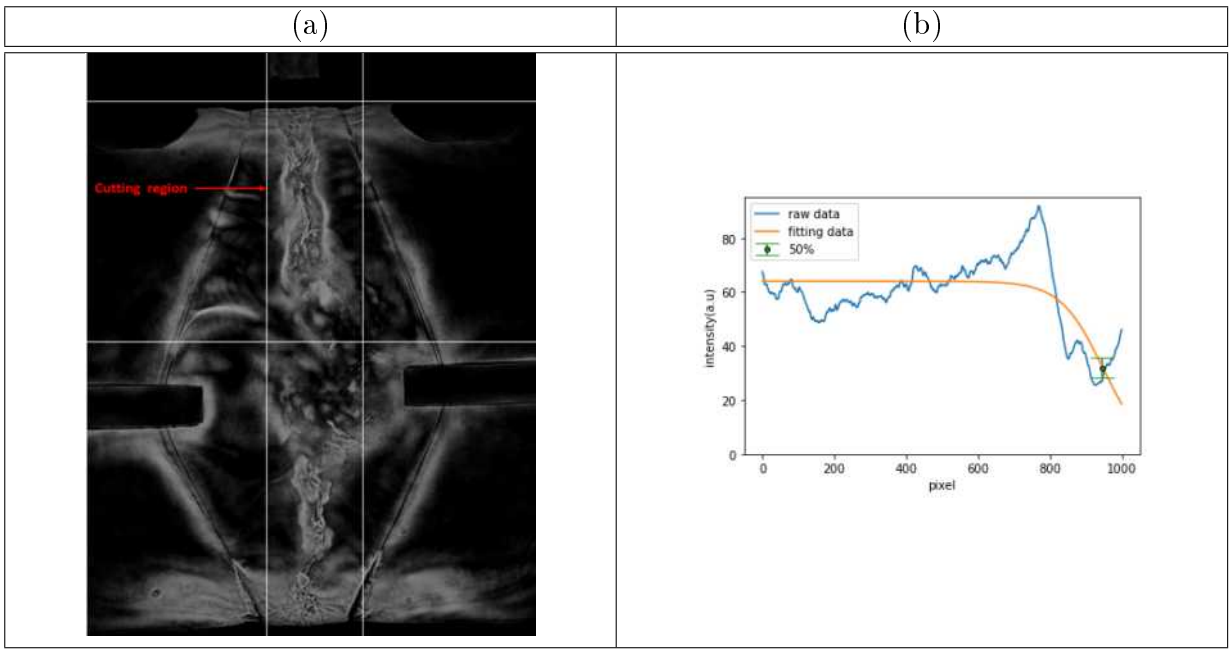

Figure 46: (a)The cutting region of the up jet. (b)The average top jet data with fitting.

Finally, the jet lengths at different times are shown in Figure 47. Figure 47(a) and 47(b) are lengths obtained from the top plasma jets and the down plasma jets, respectively. The averaged speed of the jet generated from the top is 17.2 ± 4 km/s and the error bars were defined as the error from the fitting. Unfortunately, the lengths of the down plasma jets were not clear.

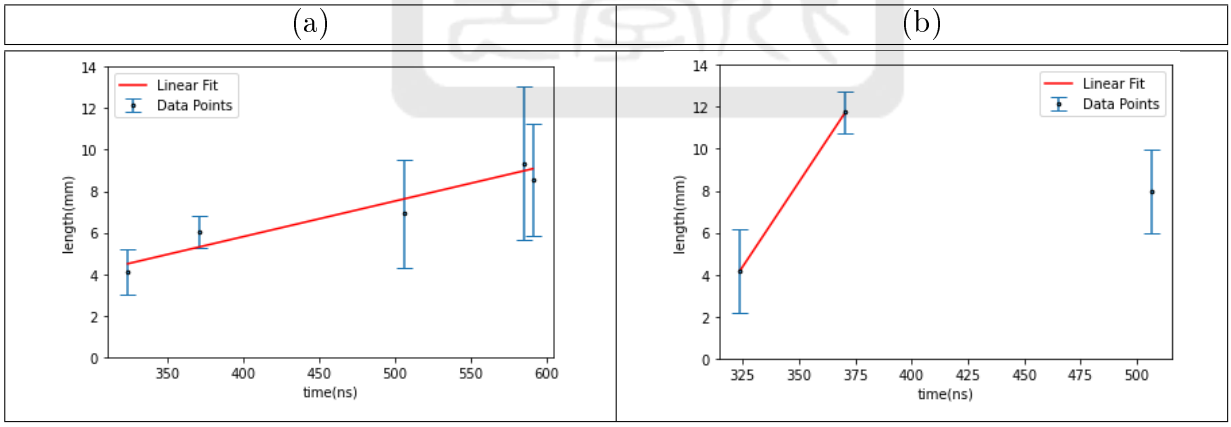

Figure 47: (a)The length of the top plasma jet in each timing. (b)The length of the down plasma jet in each timing.

The speed of down plasma jet was higher than that of the top plasma jet. The down plasma jet passed through the middle wire support at 370.7 ns. The discrepancy in speed of the two jets might come from the structural asymmetry of the bi-conical-wire array. It was because the middle horizontal support was printed by a low-cost 3D printer and is made of PLA, which is

not rigid. Therefore, the inaccuracy in assembly might cause the top wires and the down wires have different inclination angles.

3.2.4 The width of the plasma jet

We used phase changes calculated from the interferometer images to find the widths of the plasma jets. Therefore, we cut the region of the plasma jet as shown in Figure 48 and took the average in the y direction as shown in Figure 49.

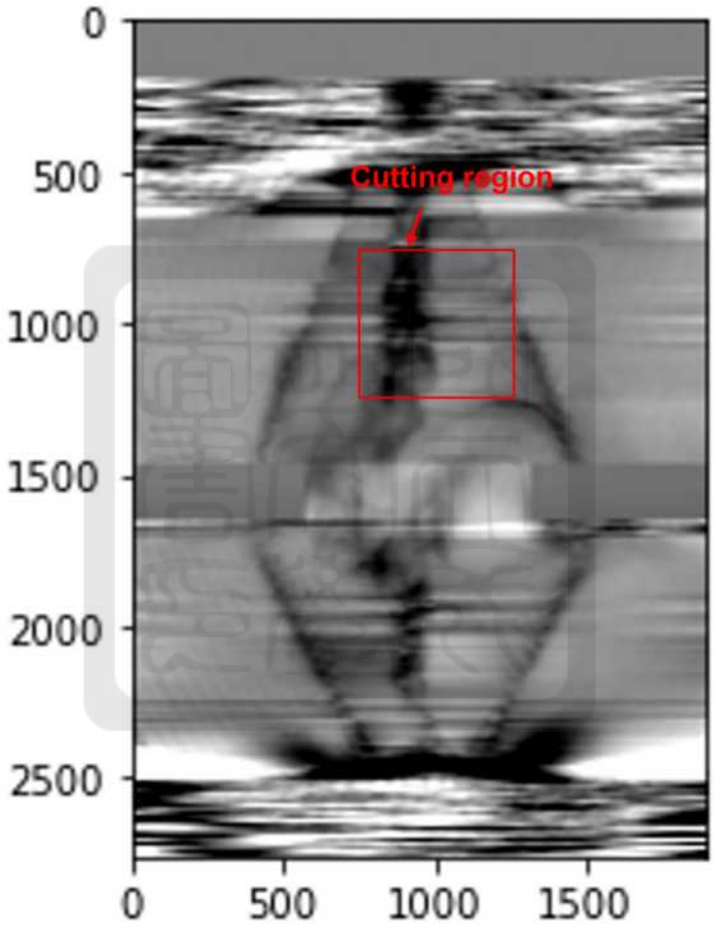

Figure 48: The cutting region of the top jet.

Then, we fit the data with the gaussian distribution function given in Eq 14 where a, b, c are the height of the peak, the postion of the peak, and the width of the function, respectively.

$$W(x) = \frac{a}{c\sqrt{2\pi}} exp(\frac{x-b}{2c})^2. \tag{14}$$

As a result, we used 4c to be the width of the jet.

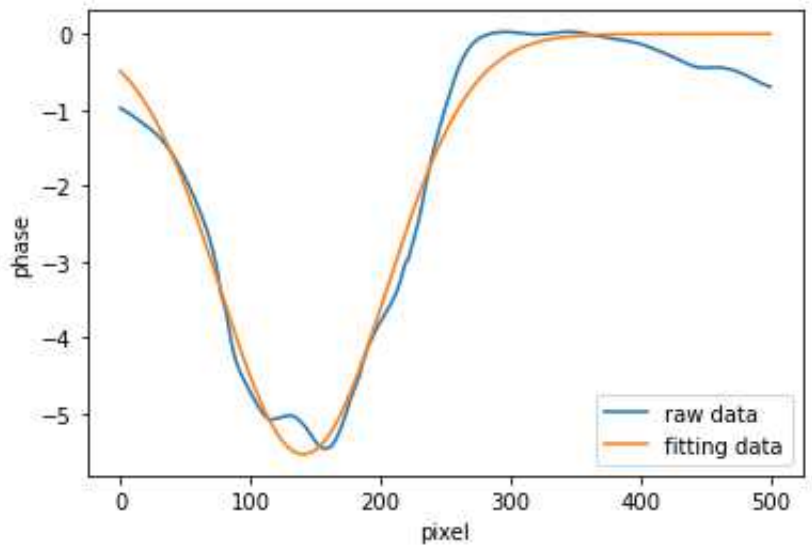

Figure 49: The data and the fitting data of the cutting region.

As a result, we can draw the width of the plasma jet as a function of time. Figure 50(a) shows the width of the top plasma jet measured at different times. Figure 50(b) shows the width of the top jet at different time. The error bars are defined as the fitting error from c. The width of the jet increased with time but reduced after 628.8 ns which suggests that the plasma might stagnate in the middle of the bi-conical-wire array. Therefore, the current no longer went though the tungsten wires. In stead, it might have gone through the top plasma jet and the down plasma jet. Therefore, plasma jets were compressed by Z-pinch effect.

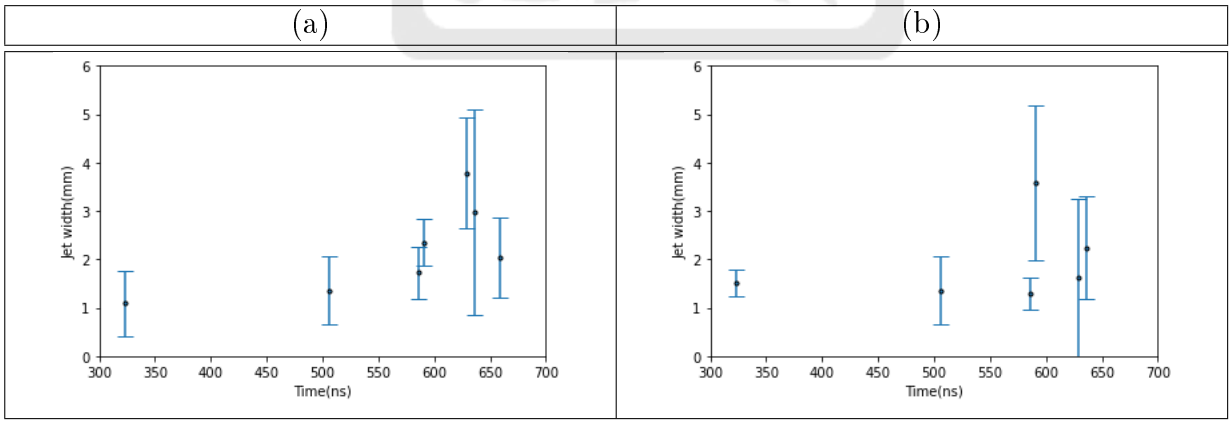

Figure 50: (a)The width of the top jet change in time. (b) The width of the bottom jet change in time.

3.2.5 The density analysis

We used the interferometer images to obtain and the phase changes to obtain the plasma density. The plasma density n_e can be calculated by Eq 15, where c is the light speed, n_c is the

laser critical density, ϕ is the phase changes, and l is the length of the plasma[9, 10].

$$n_e = -\frac{2cn_c\phi}{\omega l}. \tag{15}$$

In our experiment, our laser wavelength was 532 nm. Therefore, laser critical density $n_c = 3.94 \times 10^{27}\ m^{-3}$ caculated using Eq 16 where $\epsilon_0 = 8.854 \times 10^{-12}\ F/m$ is the permittivity of free space, $m_e = 0.91 \times 10^{-30}\ kg$ is the electron mass, $\omega = 2\pi f$ is the angular frequency of the laser.

$$n_c = \frac{\epsilon_0 m_e \omega^2}{e^2}. \tag{16}$$

Figure 51 shows the phase-change image take on 03/30 as an example. To study the dynamic of the head-on collision of the plasma jets, the phase-change image was divided in seven regions. Therefore, we can obtain the densities at different y locations.

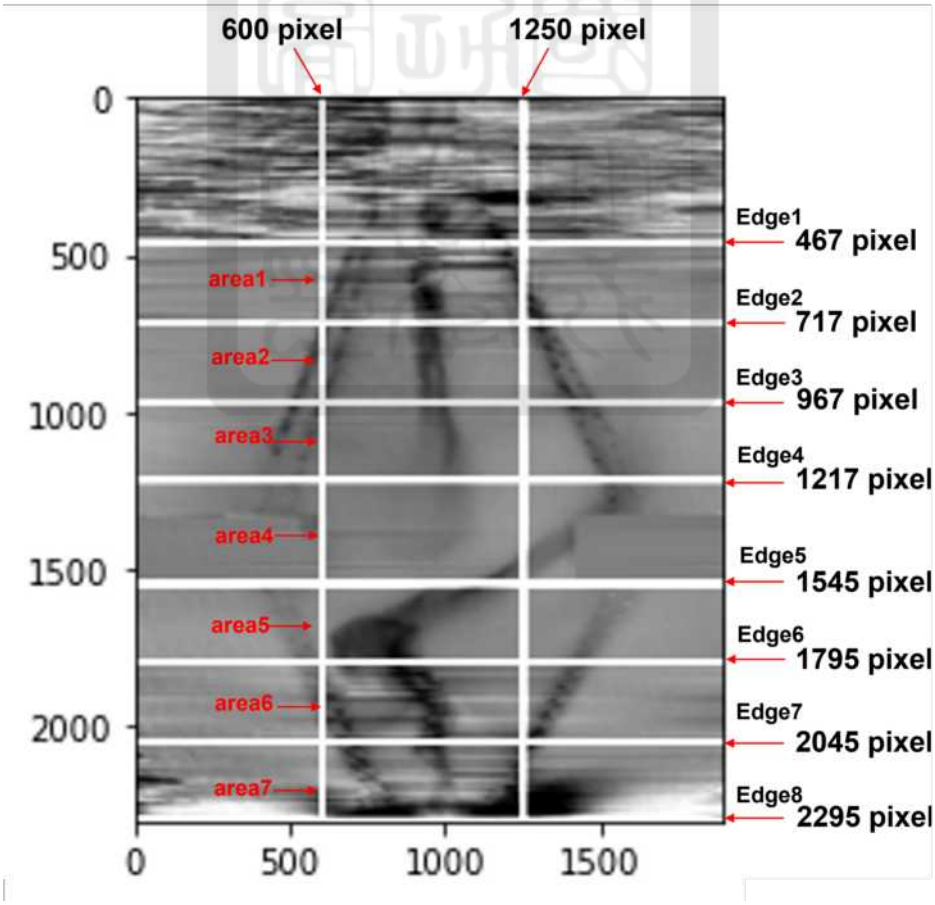

Figure 51: The seven regions we cut.

Since the screws interfered the analysis, we used the edge of the screw as the start of area 1, i.e., Edge1. In addition, we used the bottom wire support to be the bottom edge of the

analyzed area. First, we found the postion of the edge of the screw by using the cutting region shown in Figure 52(a). Then, we averaged the data in x direction as shown in the blue curve in Figure 52(b). Finally, the data will be fitted by Eq 13 shown as the red line in Figure 52(b) and the top edge of area1 (Edge1) was the location of 50% (red star) of the fitted function.

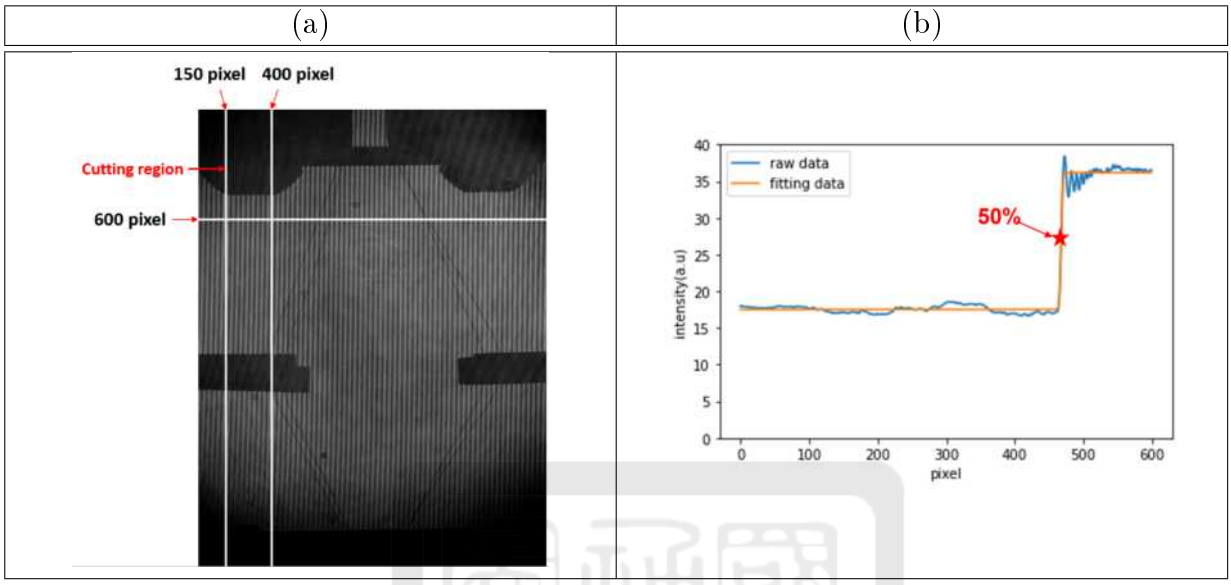

Figure 52: (a)The cutting region of the screw. (b)The fitting data of the screw.

Then, we need to find the postion of the middle wire support, i.e., Edge5. Therefore, we cut the region of the middle wire support as shown as the cutting region in Figure 53(a). The averaged in x direction is shown in Figure 53(b). Eq 11 was used to fit the data to find the postion of the middle wire support. It was defined as the location of 50% of the supergaussion amplitude (start point).

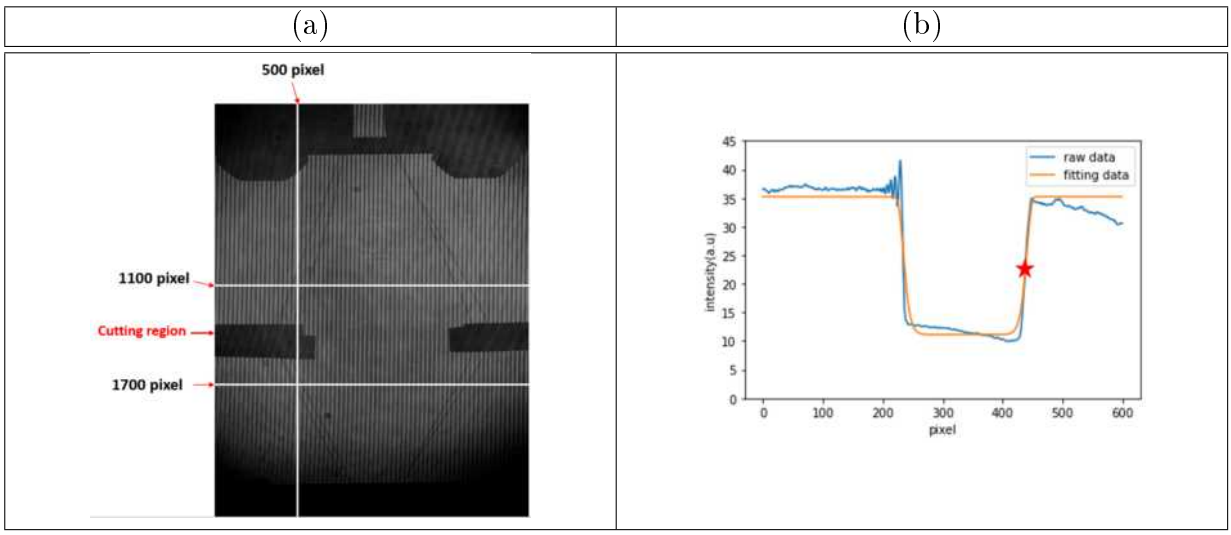

Figure 53: (a)The cutting region of middle wire support. (b)The fitting data of middle wire support.

Further, the cutting region of finding the postion of the bottom wire array (Edge8) is shown in Figure 54(a). The average of the cutting region in x direction is shown in Figure 54(b). Then, we fit the data with Eq 13 to find the postion of bottom wire support defined as the location of the 50% (red star) shown in Figure 54(b).

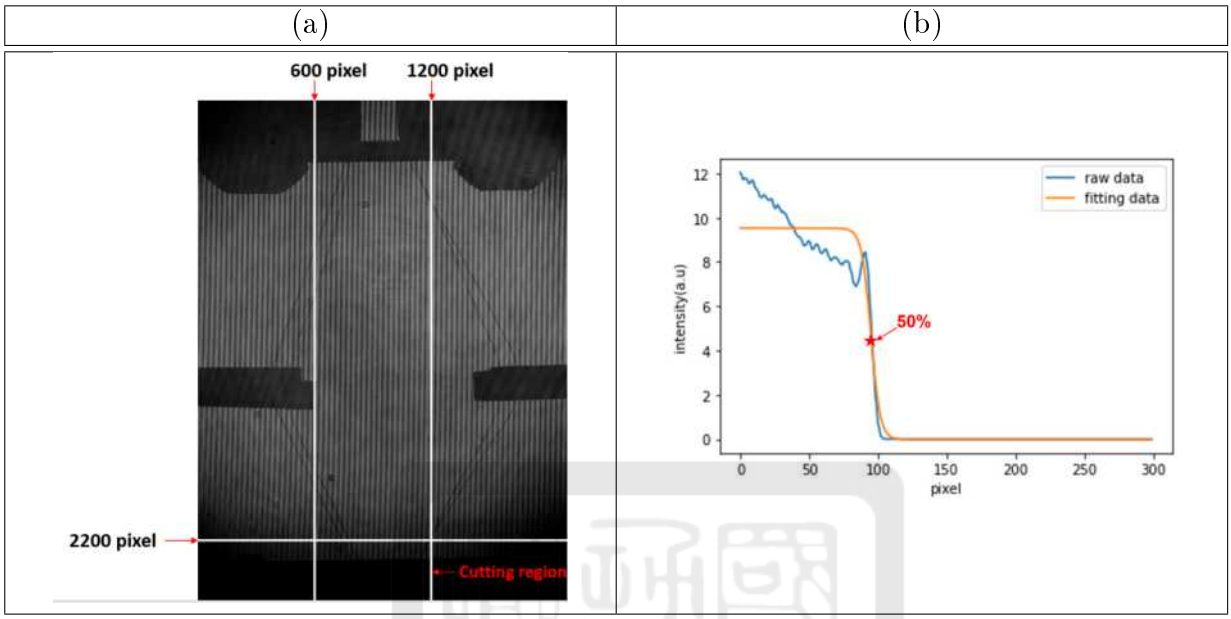

Figure 54: (a)The cutting region of bottom wire support. (b)The fitting data of bottom wire support.

As a result, we cut the area 1 to 3 starting from Edge1. Similary, we cut the area 5 to 7 started from Edge8. The heights of area1 to 3 and area5 to 7 were 250 pixel. Finally, the remaining area was defined as area 4. Then, we averaged each region in y direction and fitted the profile by Eq 17 where a, b, c, d is height of the peak, postion of the middle of the peak, the width of the peak, and the offset in y axis.

$$W2(x) = d + \frac{a}{c\sqrt{2\pi}} exp(\frac{x-b}{2c})^2. \tag{17}$$

We used the peak of the fitting result to be the total phase changes in that area and the width of the gaussian function (Eq 17) to be the diameter of the plasma jet at that area. Figure 55 is the averaged profile in area1 on shot 03/30.

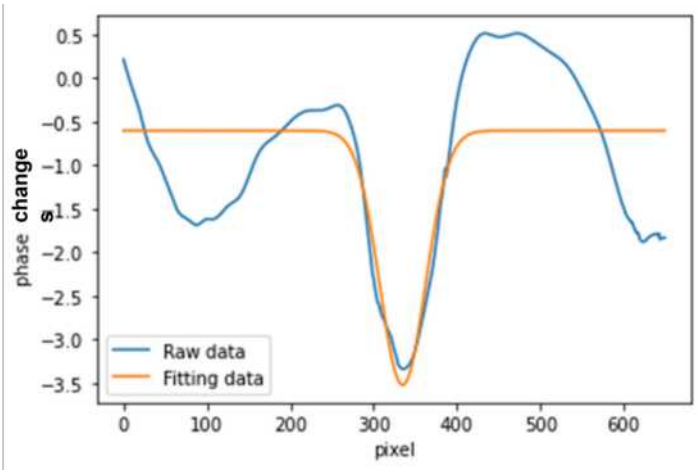

Figure 55: The fitting of the phase of the area1 at 03/30.

As a result, we were able to draw the averaged plasma density $n_e = \phi/\text{diameter}$ in area1 at each time as shown. in Figure 56. We found that the plasma density at the middle plane (area4) increased over time which meant the plasma stagnated in the middle of the bi-conical-wire array. Then we draw the line integrated plasma density $n_e l$ in Figure 57 and try to see if the phase only changed by the density changed. However, there aren't too much information. Therefore, we drew the plasma density respect to differerent y postion at different time in Figure 58. We found that the plasma was pushed into the middle from both the topside and downside so that the density at the middle increased while the density decreased at the top and the bottom at 774.0 ns shown as the gray line in Figure 56. Furthermore, we plotted the density respect to time in each area in Figure 59. At some similar times, the plasma density in area1,area6, and area7 seems to behave differently. This might come from the the shot-to-shot variation. Nevertheless, we can see the plasma density in area3 and area4 increased over time.

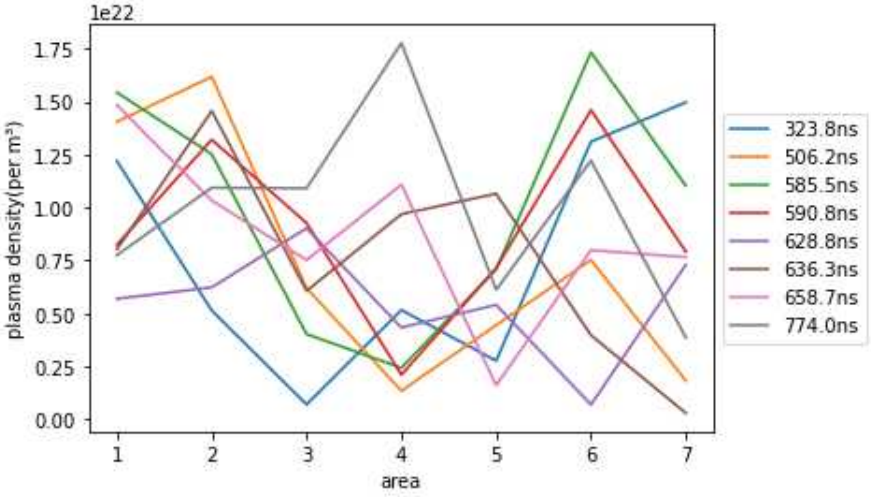

Figure 56: The plasma density ne changed from the upper jet to the down jet in different time.

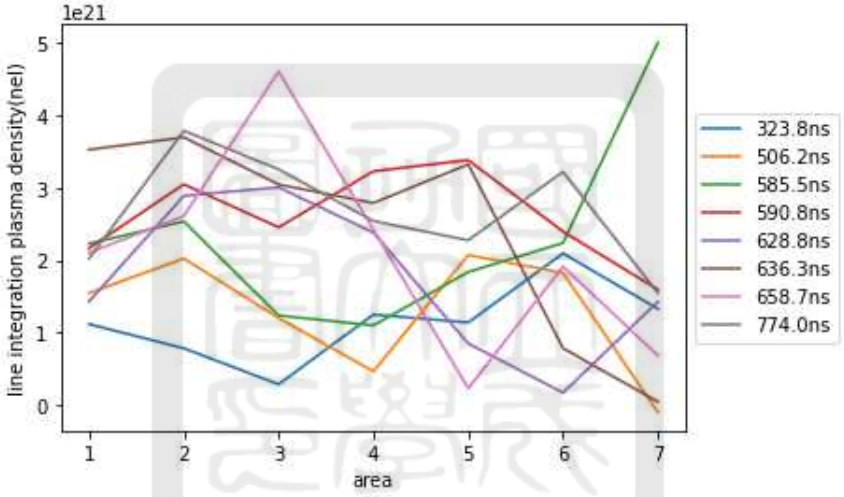

Figure 57: The plasma density nel changed from the upper jet to the down jet in different time.

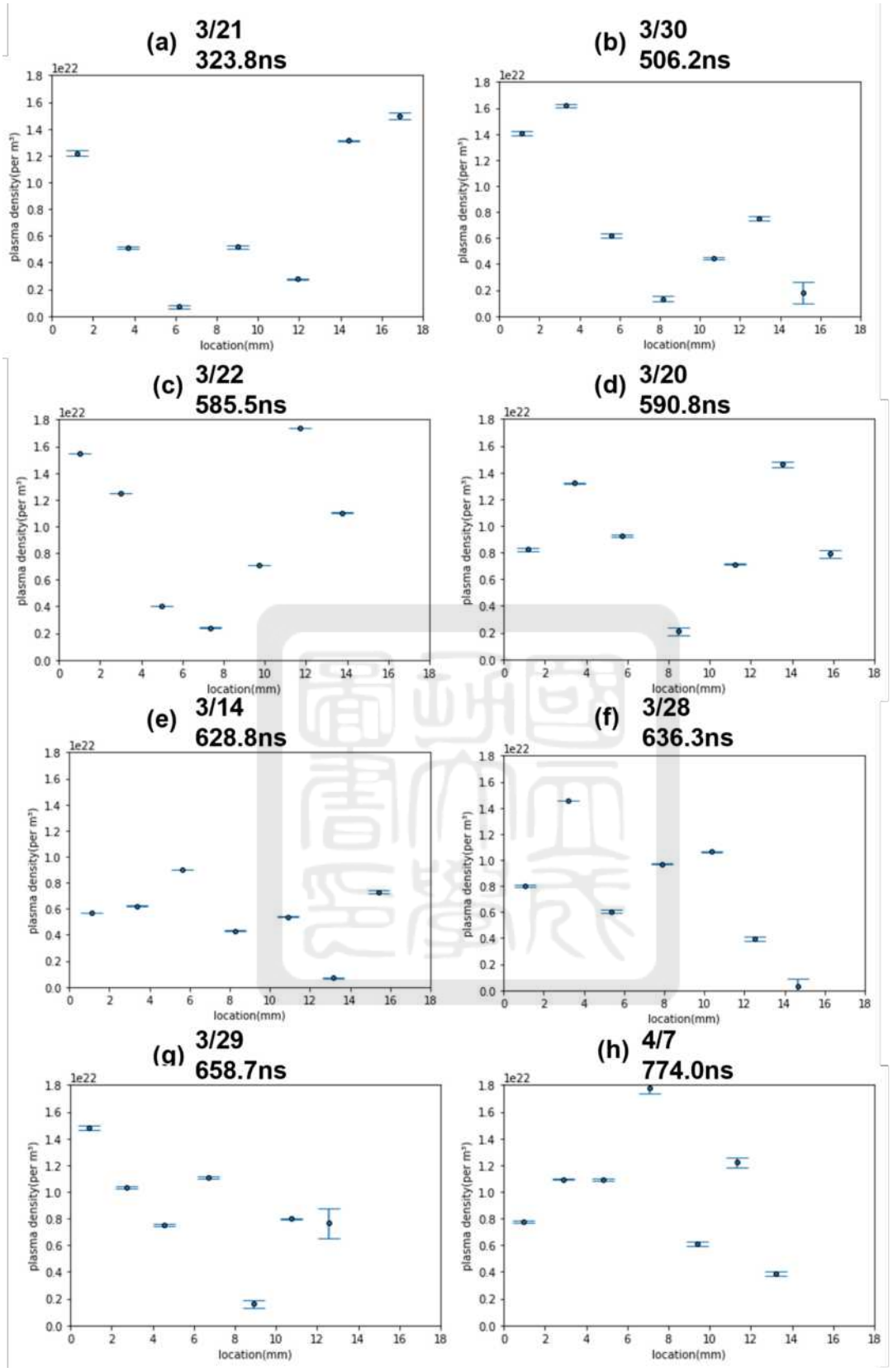

Figure 58: The density changed from the upper jet to the down jet of each time.

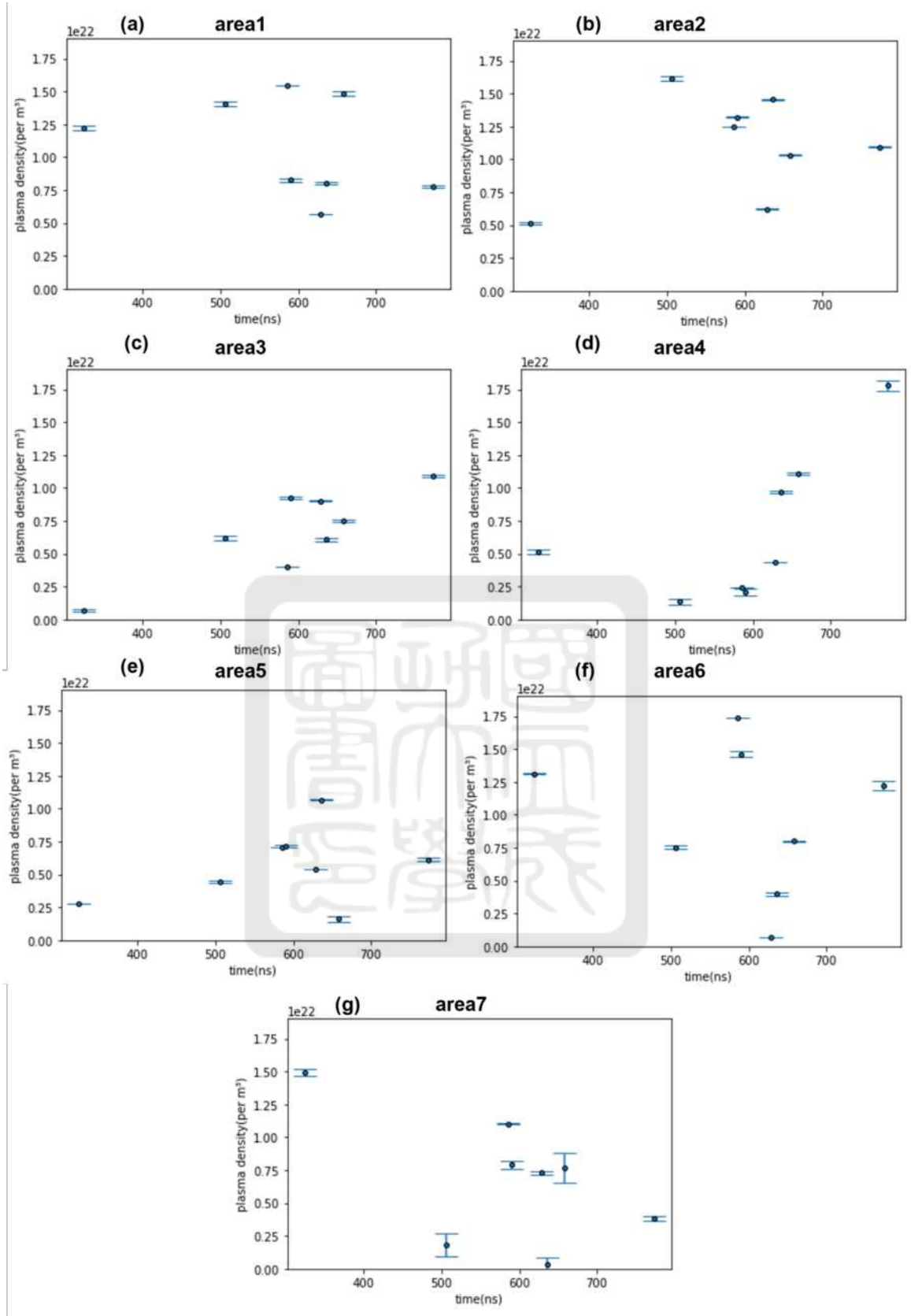

Figure 59: The plasma density changed in each area with time.

The experimental result presented in Ref.[17] shows the head-on collision of two plasma jets can generate a plasma disk. We found the structure of the bi-conical-wire array used in

Ref.[17] was different from the one we used. As shown in Figure 60(a), they separated two conical-wire arrays in the bi-conical-wire array using the green block. The red arrows show the current path. In between, they used two apertures at the middle to ensure only plasma jets went into the gap. Therefore, the green block will block the plasma pushed from the side then the collimated plasma jet generated from the top and bottom can form a plasma disk shown in Figure 60(b). Contraily, in the bi-conical-wire array we designed the plasma kept being pushed so that the plasma stagnated at the middle as shown in Figure 61(a). The stagnated plasma in our experiment is more similar to the experiment done by Plasma Jet Driven Magneto-Inertial Fusion (PJMIF) where they used lots of plasma guns surrouning the spherical chamber to drive magneto-inertial fusion[11] as shown in Figure 61(b). A stagnated plasma was formed at the center of the spherical chamber just like the stagnated plasma formed at the middle of our bi-conical-wire array.

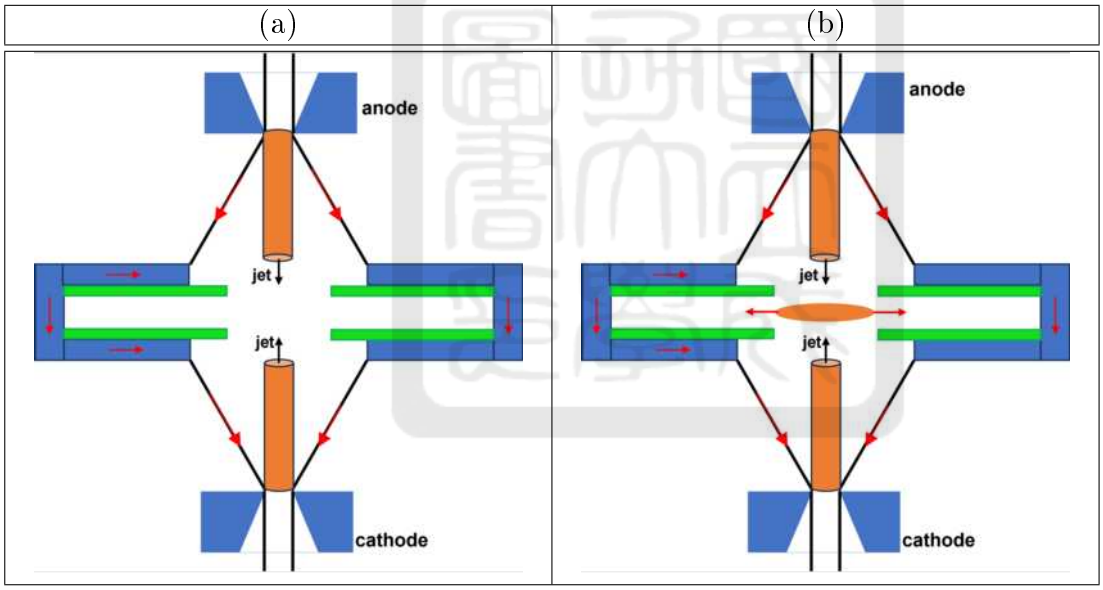

Figure 60: (a)The conical-wire array other used. (b)The conical-wire array with disk.

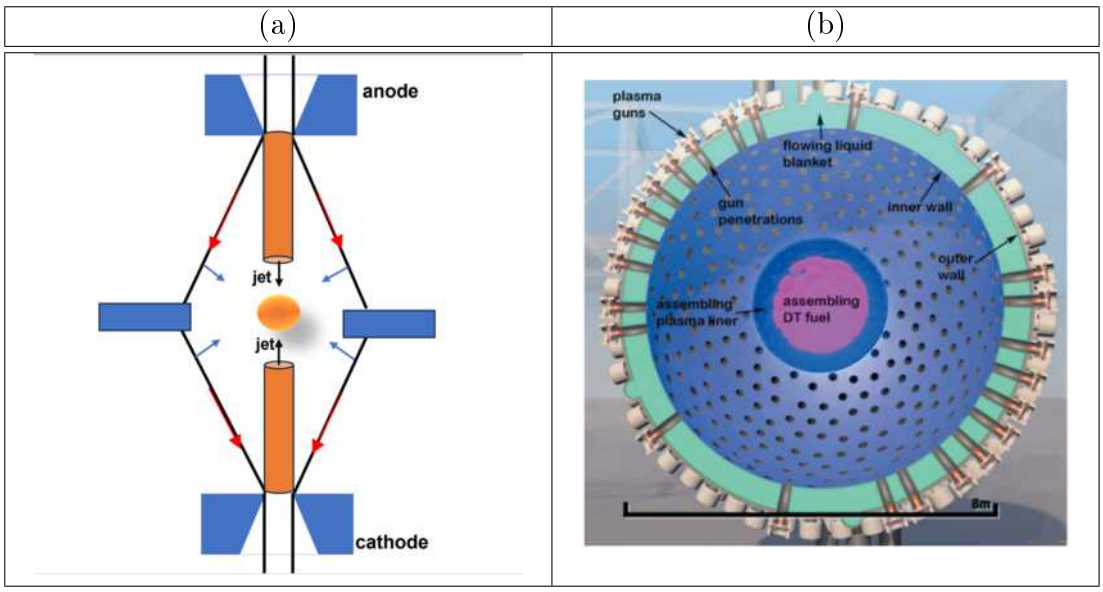

Figure 61: (a)The generated of . (b)The PJMIF fusion concept[11].

3.3 Summary

We demonstrated that the head-on collision of two counter propagating plasmas jets caused the plasma stagnates using the bi-conical-wire array. At the middle of the bi-conical-wire array, the plasma density reached the order of 10^{22} per m^2. The top jet and the down jet propagated at different speeds. The top jet traveled with an averaged speed of 17.2 ± 4 km/s. Unfortunately, the speed of the down jet can not be analyzed since there were only two reasonable data points. In fact, the down jet reached the middle of the bi-conical-wire array at 370.7 ns. The width of both the top jet and the down jet increased first and became thinner after 628.8 ns suggested that current flew through the plasma jets so that they were compressed by the Z-pinch effect. Finally, density at the middle where two jets collide increased over time showing that plasma stagnated at the collision region.

4 Future work

We have successfully generated counter-propagating plasma jets. We also observed that plasma was stagnated when two plasma jets collided. However, there are several improvements and unfinished works needed. They are:

1. To solve the asymmetry of the bio-conical-wire array. It was because the plastic middle holder was not rigid enough. New material may be used.

2. To measure the magnetic field using the polarimetry to study where the current flows. Does it flow through tungsten wires or the plasma jet?

3. Qualitative measurement the temperature of the plasma by using the Thomson scattering.

4. To verify the experiment results using simulations.

5. Finally and most importantly, we want to study the head-on collision of two rotating plasma jets to understand the angular momentum conservation of the system. Twisted bi-conical-wire arrays will be used.

5 Summary

In this thesis, we are studying the stagnated plasma generated by the head-on collisions of two plasma jets. First, to prevent the laser from the EMP, we design a Faraday cage to cover the laser. Then, to improve our pulsed-power system, the eight-stage high-voltage pulse generator was built to replace the slow high-voltage pulse generator which was the second stage of the multistep high-voltage trigger system. The eight-stage high-voltage pulse generator can generated a pulse of about -5600 V with a falling time of 128 $\pm$ 1 ns. To make the trigger of the Marx generator, which is the third stage of the multistep high-voltage trigger system, more stable, we adjusted the first stage of the marx generator from 10 mm to 8.5 mm. As a result, the delay of the new multistep high-voltage trigger system is 230 $\pm$ 90 ns. Thus, the trigger of the system now is simply using the delay generator to send two signals, one to the eight-stage high-voltage pulse generator and the other one to the Q-switch laser. The laser we use in the laser camera system is an ND:YAG Q-switch laser with a 5 ns pulse at 532 nm for taking the time-resolved interferometer, shadowgraph, schlieren, and polarimetry images from the side.

To generate two counter-propagated plasma jets with enough plasma density, we used bi-conical-wire arrays with a height of 10 mm. It was driven by a pulsed current provided by our pulsed-power system. The pulse current was 123.5 $\pm$ 1 kA with a risetime of 1592 $\pm$ 3 ns. First, we measured the plasma jet speed using the time-resolved schlieren images. The averaged speed of the top jet was 17.2 $\pm$ 4 km/s. The speed of the down jet was not measured accurately. Nevertheless, it reached the middle of the bi-conical-wire array at 370.7 ns. Finally, the plasma stagnated in the middle of the bi-conical-wire array when two plasma jets collided with each other. The density of the plasma jet were in the order of 10^{22} per m^2. We found that both the top and the bottom plasma jet become thinner after 628.8 ns. In addition, we divided the bi-conical-wire array in seven regions from the top to the bottom to observe the change of the plasma density. We found that after about 600 ns, the plasma started to pile up in the middle plane of the bi-conical-wire array and formed a stagnanted plasma with a density of about 10^{22} per m^3. It suggests that the stagnated plasma not only came from the plasma jets but also from the ablated plasma from the tungsten wires of the bi-conical-wire array.

References

[1] F. Macchetto J. A. Biretta, W. B. Sparks. Hubble space telescope observations of superluminal motion in the m87 jet. *The astorophysical*, 1999.

[2] Shinji Koide, Kazunari Shibata, Takahiro Kudoh, and David L. Meier. Extraction of black hole rotational energy by a magnetic field and the formation of relativistic jets. *Science*, 295(5560):1688–1691, mar 2002.

[3] A. Casner, T. Caillaud, S. Darbon, A. Duval, I. Thfouin, J.P. Jadaud, J.P. LeBreton, C. Reverdin, B. Rosse, R. Rosch, N. Blanchot, B. Villette, R. Wrobel, and J.L. Miquel. LMJ/PETAL laser facility: Overview and opportunities for laboratory astrophysics. *High Energy Density Physics*, 17:2–11, dec 2015.

[4] National technology and engineering solutions of sandia. *https://www.sandia.gov/news/image-gallery/*, 2023.

[5] D. J. Ampleford, S. V. Lebedev, S. N. Bland, S. C. Bott, J. P. Chittenden, C. A. Jennings, V. L. Kantsyrev, A. S. Safronova, V. V. Ivanov, D. A. Fedin, P. J. Laca, M. F. Yilmaz, V. Nalajala, I. Shrestha, K. Williamson, G. Osborne, A. Haboub, and A. Ciardi. Dynamics of conical wire array z-pinch implosions. *Physics of Plasmas*, 14(10):102704, oct 2007.

[6] Po-Yu Chang, Yen-Cheng Lin, Ming-Hsiang Kuo, Cheng-Han Du, Chih-Jui Hsieh, Mei-Feng Huang, Ming-Cheng Jheng, Jia-Kai Liu, Sheng-Hua Yang, I-Lin Yeh, and Frank J. Wessel. One-kilojoule pulsed-power generator for laboratory space sciences. *Review of Scientific Instruments*, 93(4):043505, apr 2022.

[7] Po-Yu Chang, Chih-Jui Hsieh, Mei-Feng Huang, Ming-Cheng Jheng, Yen-Cheng Lin, Jia-Kai Liu, and Sheng-Hua Yang. Rail-gap switch with a multistep high-voltage triggering system. *Review of Scientific Instruments*, 91(11):114703, nov 2020.

[8] Po-Yu Chang. Nstc report, project most-111-2112-m-006-013.

[9] M. Hipp, J. Woisetschläger, P. Reiterer, and T. Neger. Digital evaluation of interferograms. *Measurement*, 36(1):53–66, jul 2004.

[10] Chang Po-Yu. Application of plasma phenomena (la50800).

[11] Y. C. Francis Thio, Scott C. Hsu, F. Douglas Witherspoon, Edward Cruz, Andrew Case, Samuel Langendorf, Kevin Yates, John Dunn, Jason Cassibry, Roman Samulyak, Peter Stoltz, Samuel J. Brockington, Ajoke Williams, Marco Luna, Robert Becker, and Adam Cook. Plasma-jet-driven magneto-inertial fusion. *Fusion Science and Technology*, 75(7):581–598, may 2019.

[12] I-Lin Yeh. Theoretical study of the solar wind interacting with an unmagnetized planet in space and in laboratory. *Master thesis*.

[13] Ming-Hsiang Kuo. Study of the plasma disk generated from the head-on collision of two plasma jet. *Master thesis*, 2022.

[14] D. Ryutov, R. P. Drake, J. Kane, E. Liang, B. A. Remington, and W. M. Wood-Vasey. Similarity criteria for the laboratory simulation of supernova hydrodynamics. *The Astrophysical Journal*, 518(2):821–832, jun 1999.

[15] R. J. Baker and B. P. Johnson. Stacking power MOSFETs for use in high speed instrumentation. *Review of Scientific Instruments*, 63(12):5799–5801, dec 1992.

[16] Lin Yen-Cheng. Studies of rotational plasma jets produced by twisted-conical-wire arrays. *master thesis*.

[17] J.C. Valenzuela, G.W. Collins, T. Zick, J. Narkis, I. Krasheninnikov, and F.N. Beg. Counter-propagating plasma jet collision and shock formation on a compact current driver. *High Energy Density Physics*, 17:140–145, dec 2015.

A Appendix

A.1 The location diagram of the eight-stage high-voltage pulse generator circuit board placement

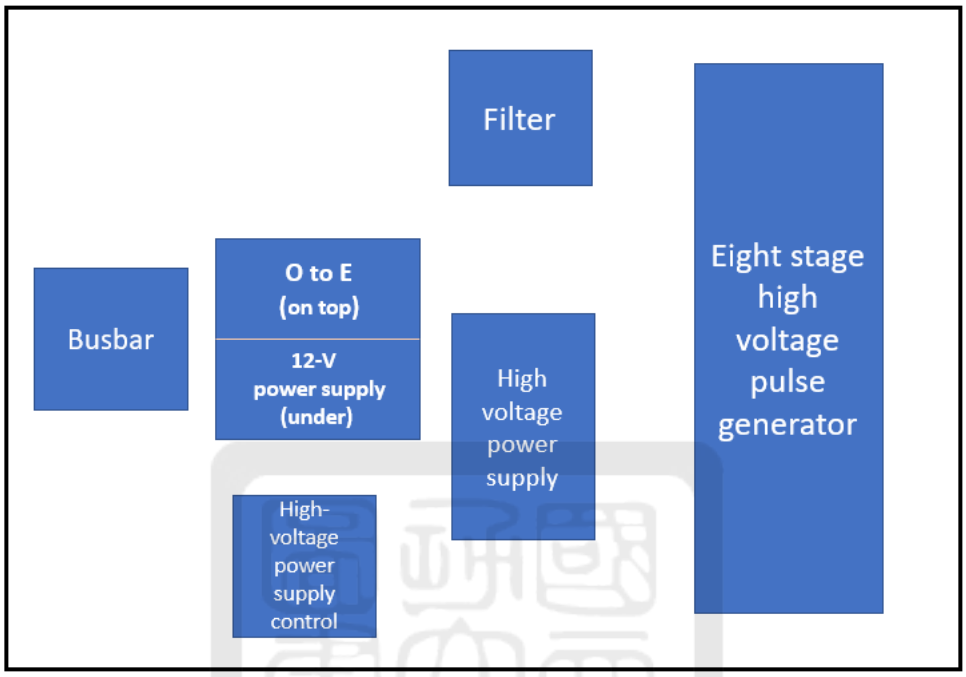

Figure 62: The location diagram of the eight-stage high-voltage pulse generator circuit board placement.

A.2 The layout of the eight-stage high-voltage pulse generator

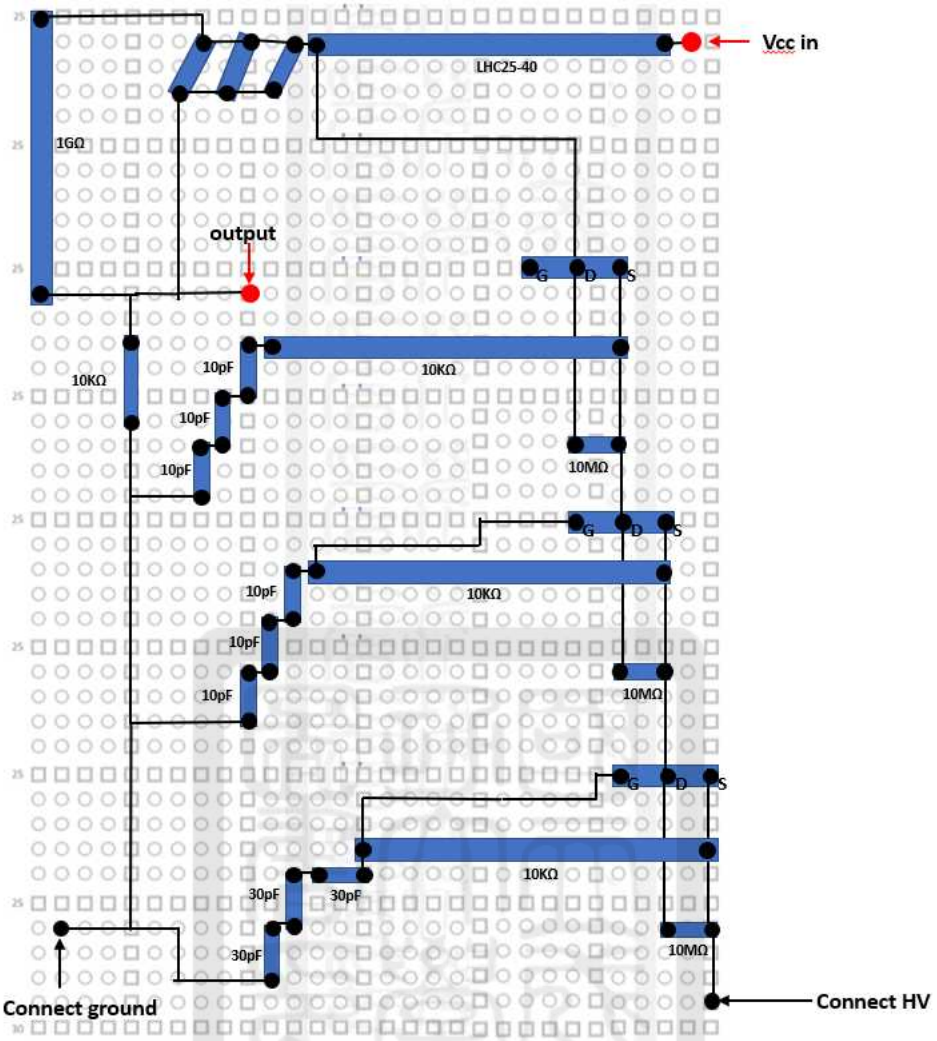

Figure 63: The first circuit board of the eight-stage high-voltage pulse generator.

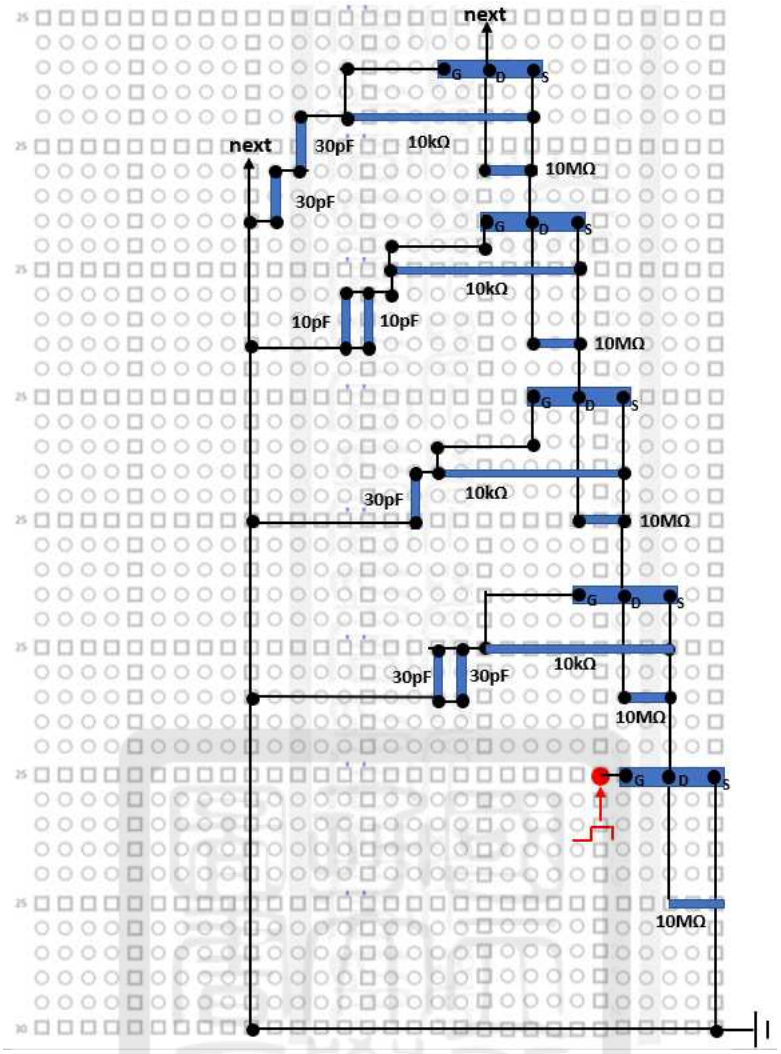

Figure 64: The first circuit board of the eight-stage high-voltage pulse generator.

A.3 The layout of the filter of the eight-stage high-voltage pulse generator

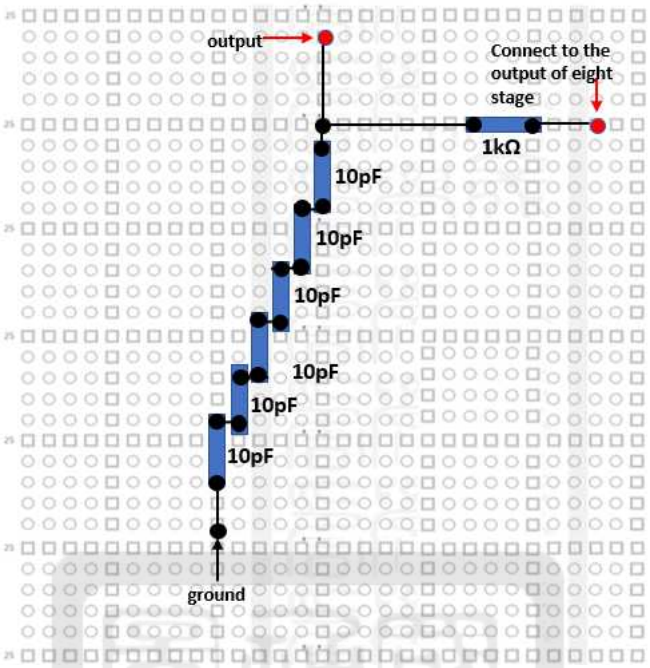

Figure 65: The layout of the filter of the eight-stage high-voltage pulse generator

A.4 The high-voltage power supply control board layout

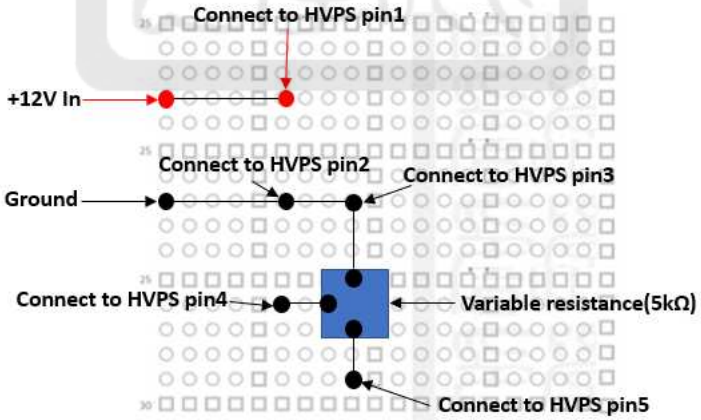

Figure 66: The layout of the contral board for high-voltage power supply.

A.5 The layout of the 12-V power supply

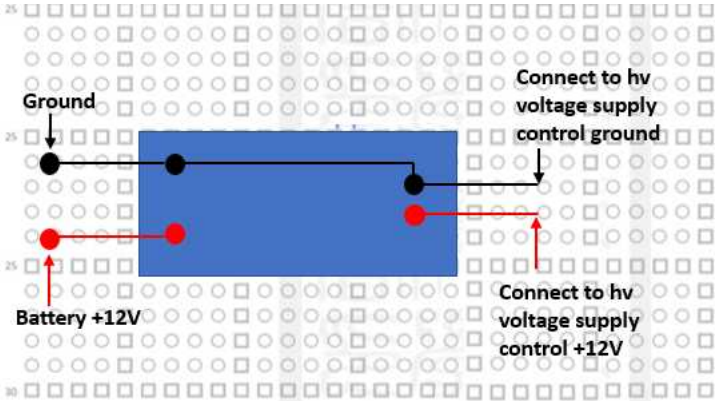

Figure 67: The layout of the 12-V power supply circuit board.

A.6 The bus bar layout

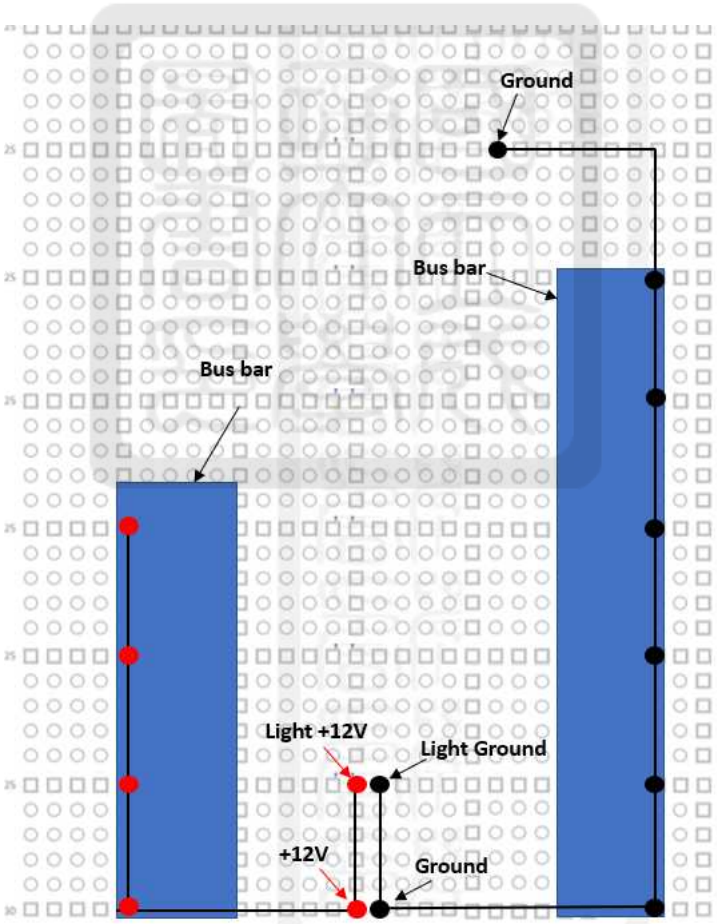

Figure 68: The layout of bus bar.

A.7 Engineering drawing of the bi-conical-wire array

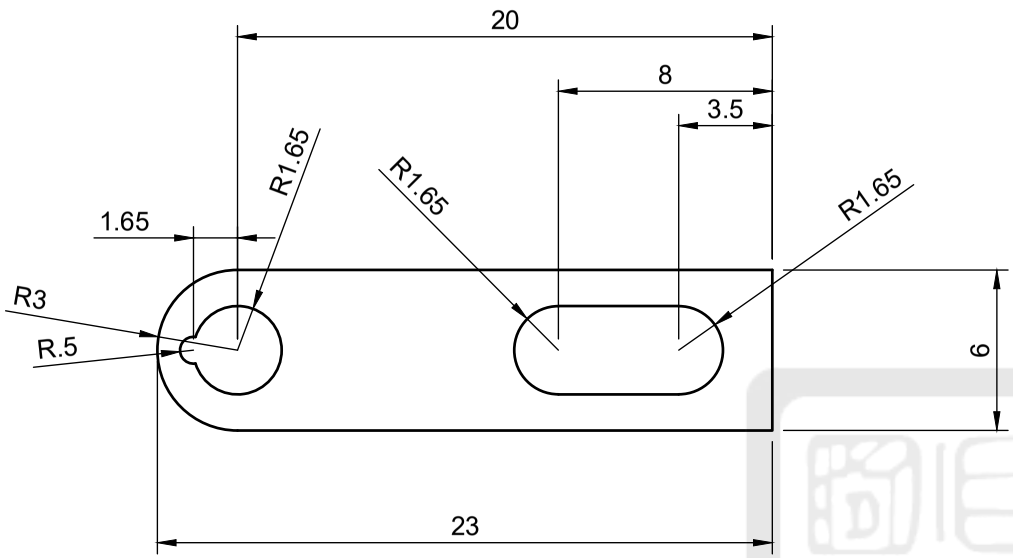

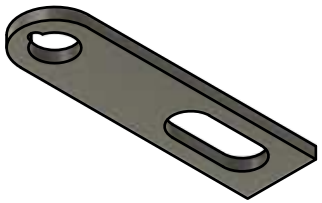

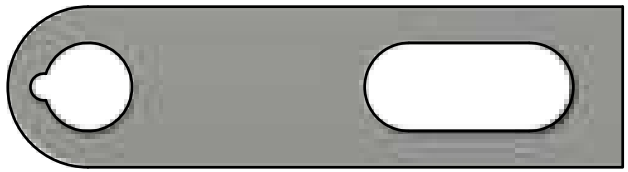

Unit:mm

note:
Unless other wise specified

- Tolerance: 2PL±0.005
- Edge:0.4 x 45°

Dept.	Technical reference	Created by	Approved by
ISAPS		Che-Yu Liu 2022/11/1	
		Document type	Document status
		Title: (1mm)middle wire support	DWG No.: PPL20220003_LCY
		Rev.: A	Date of issue: 2022/11/01 — Sheet: 1/1

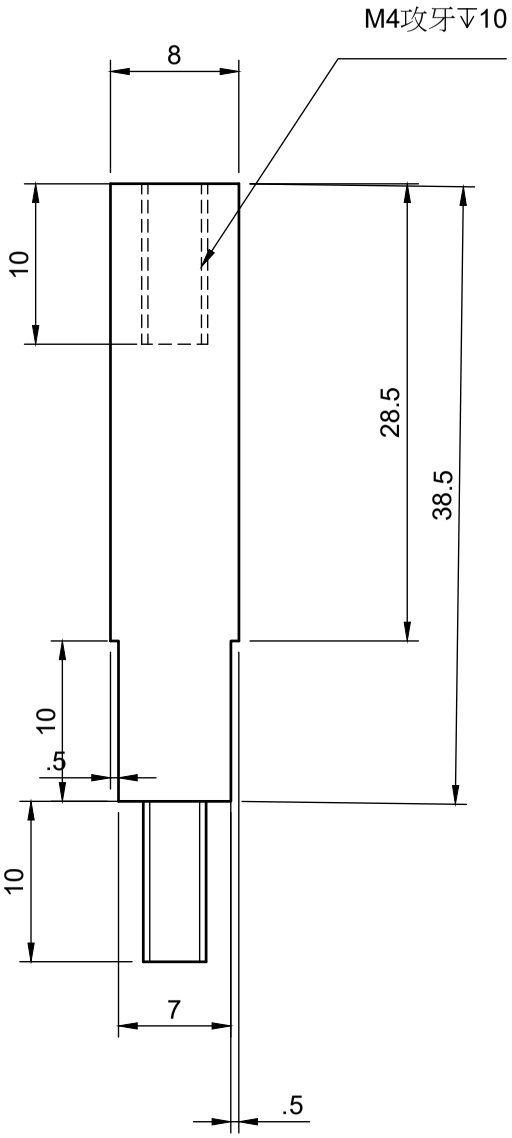

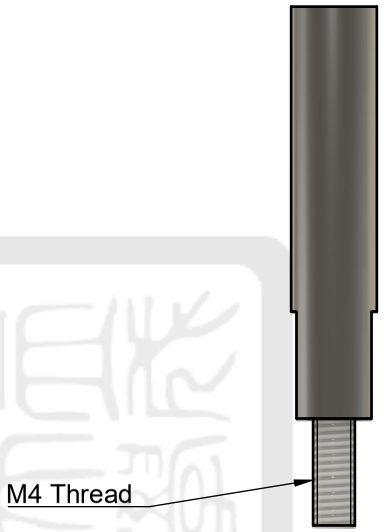

Dept.	Technical reference	Created by	Approved by
ISAPS		Che-Yu Liu 2022/11/1	
		Document type	Document status
		Title: Top support	DWG No.: PPL20220002_LCY
		Rev.: A	Date of issue: 2022/11/01 — Sheet: 1/1

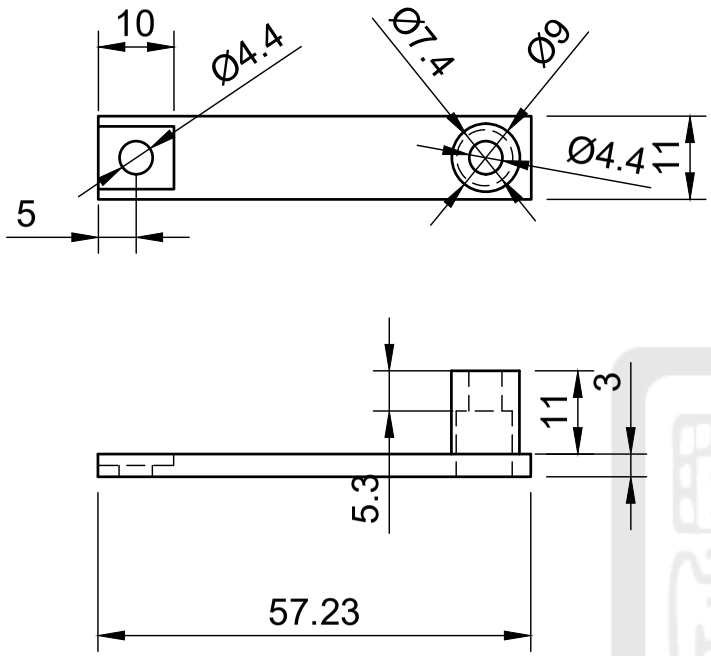

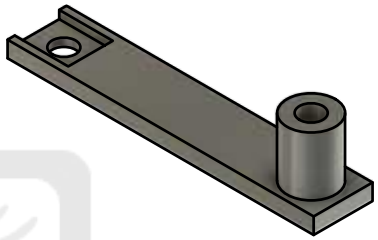

Dept.	Technical reference	Created by 哲宇 劉 2023/6/21	Approved by
		Document type	Document status
		Title: plastic middle holder	DWG No.
			Rev. / Date of issue: 2022/11/20 / Sheet: 1/1

A.8 The anlyze data

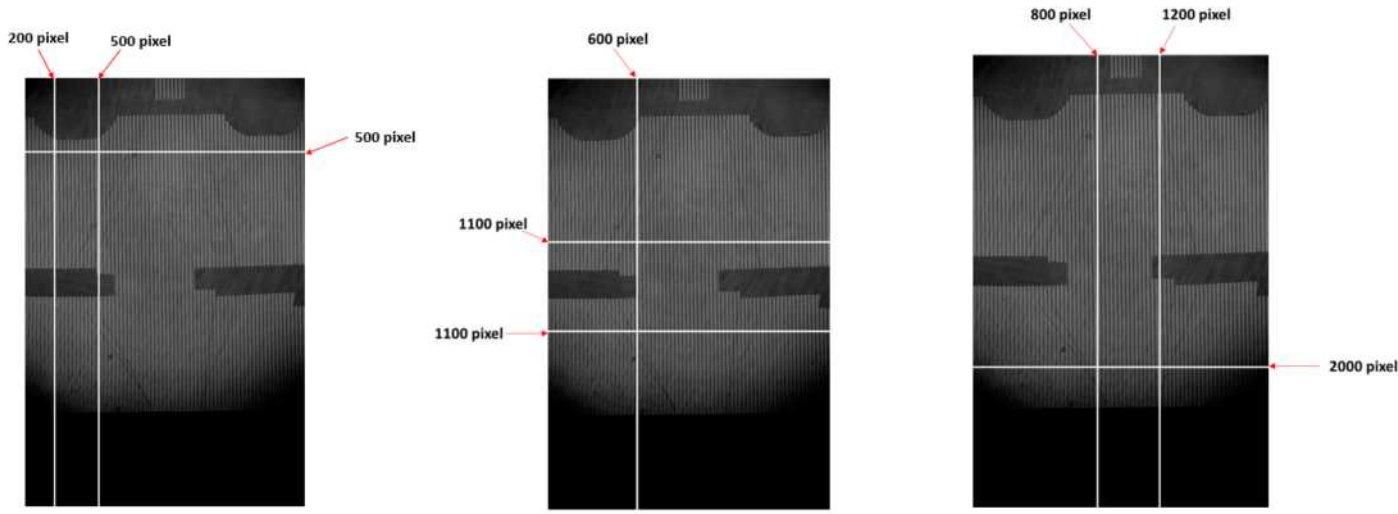

Figure 69: The cutting region for find the bound 03/14 (628.8 ns).

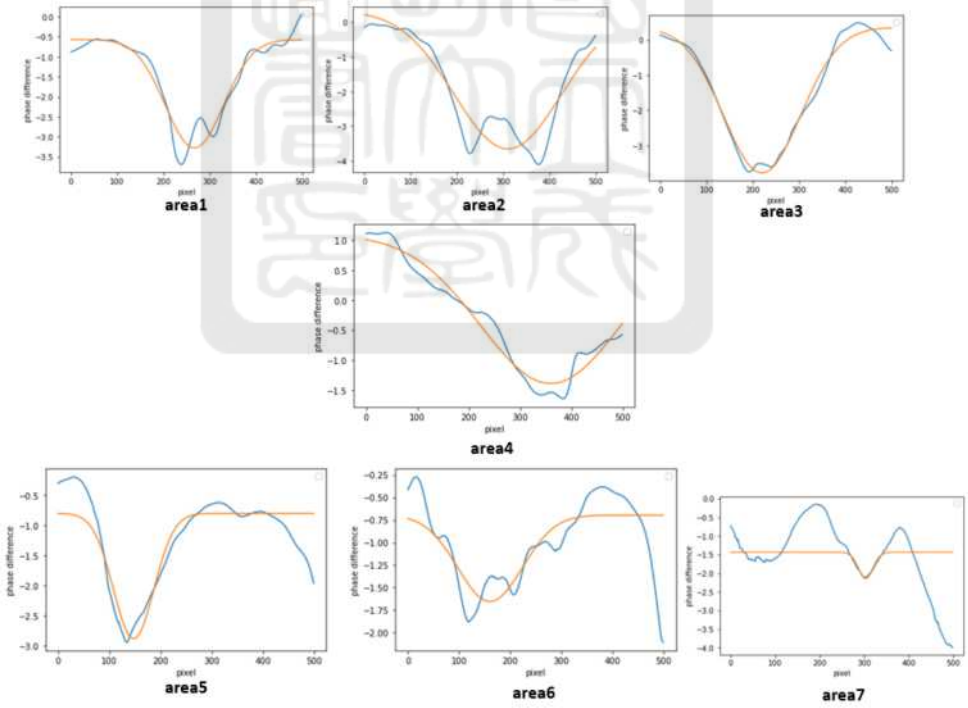

Figure 70: The fitting of each area 03/14 (628.8 ns).

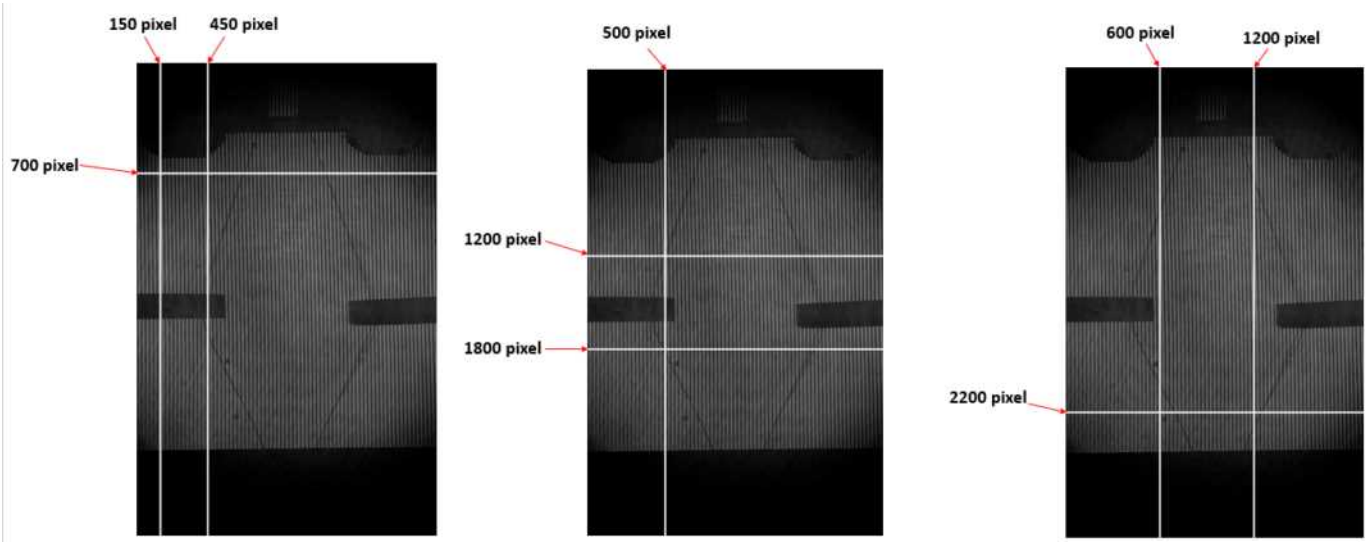

Figure 71: The cutting region for find the bound 03/20 (590.8 ns).

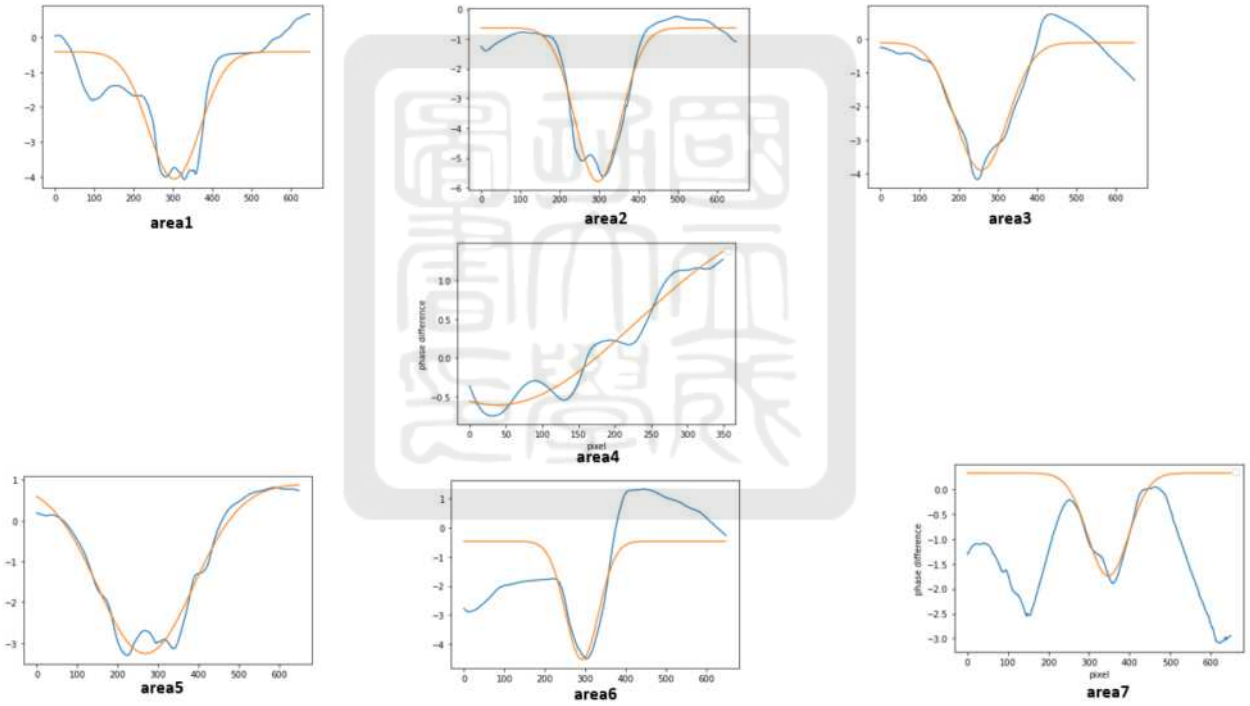

Figure 72: The fitting of each area 03/20 (590.8 ns).

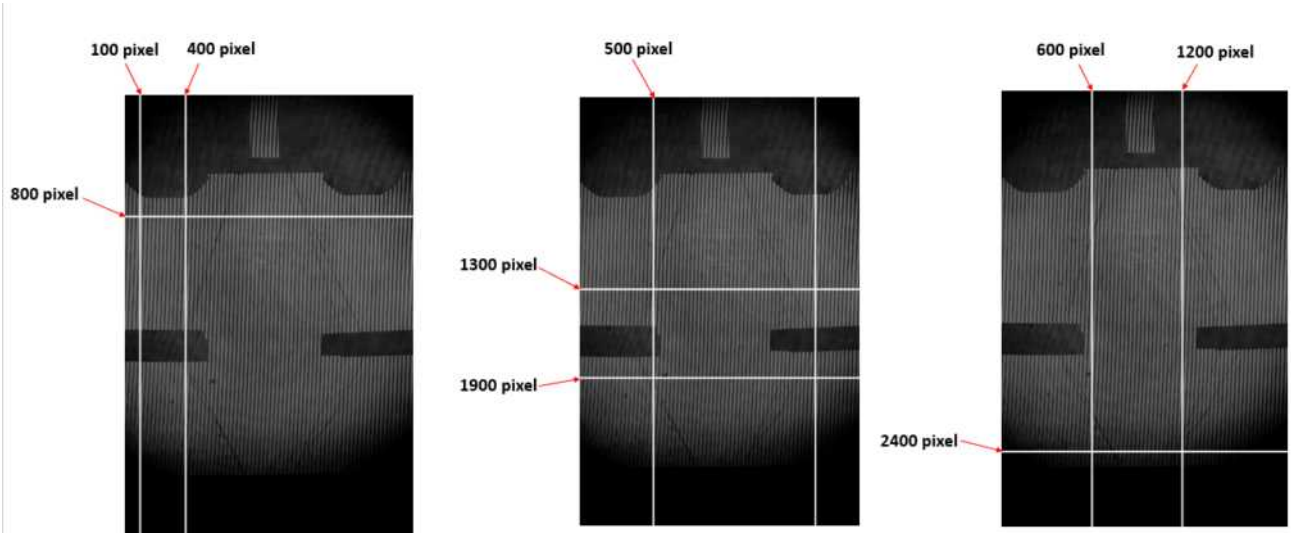

Figure 73: The cutting region for find the bound 03/21 (323.8 ns).

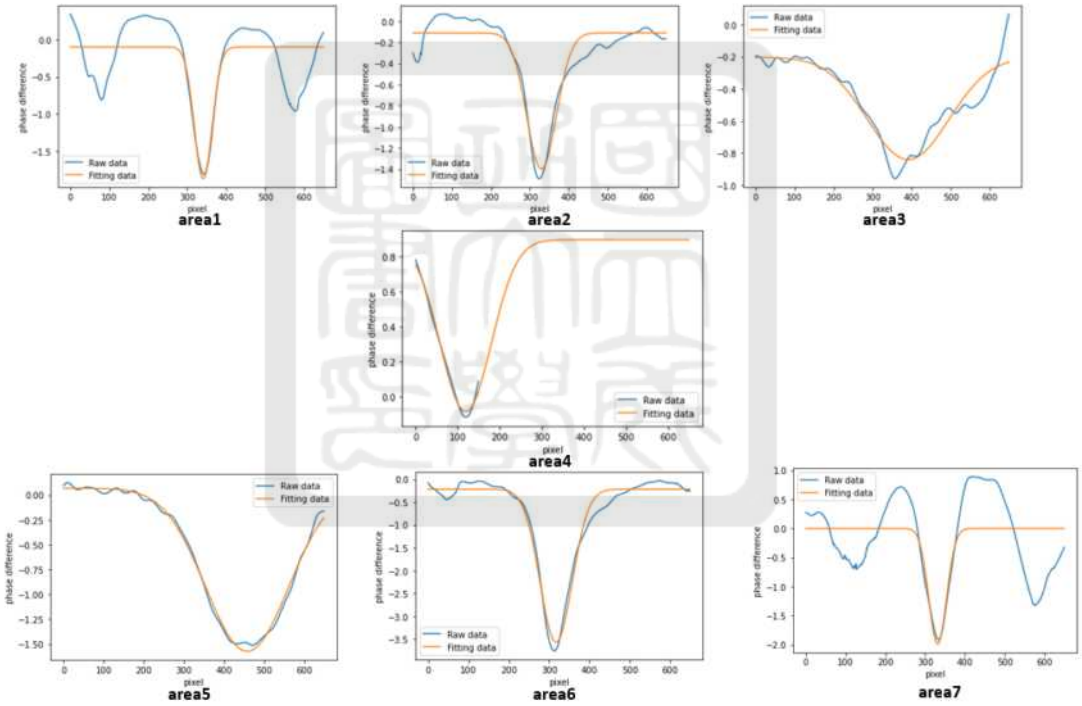

Figure 74: The fitting of each area 03/21 (323.8 ns).

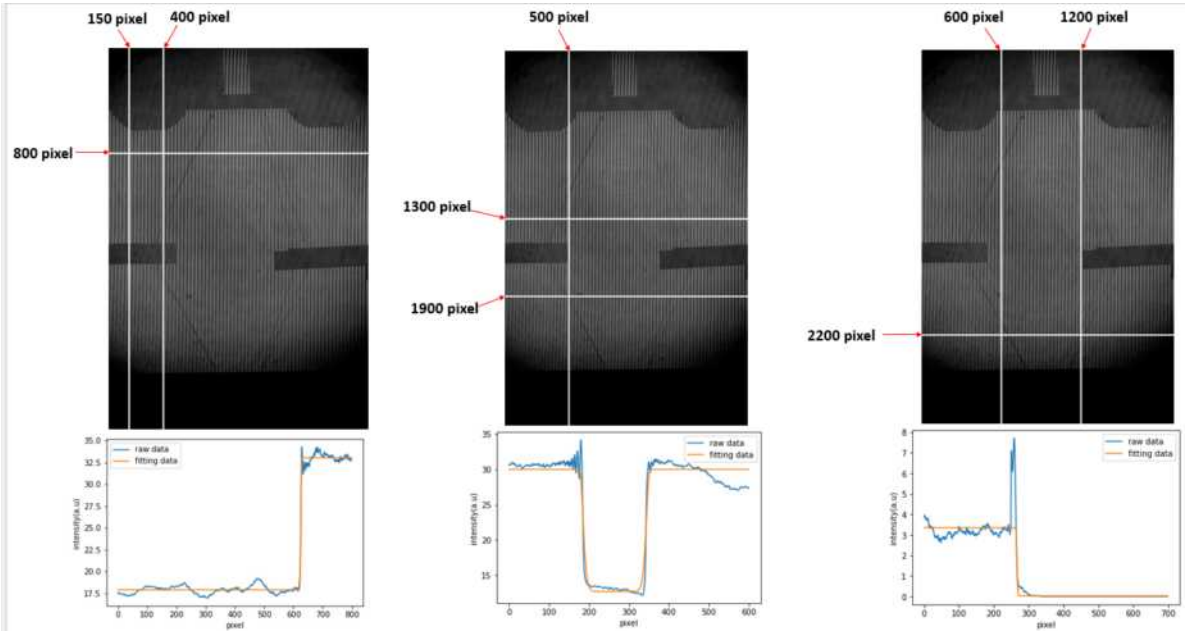

Figure 75: The cutting region for find the bound 03/22 (585.5 ns).

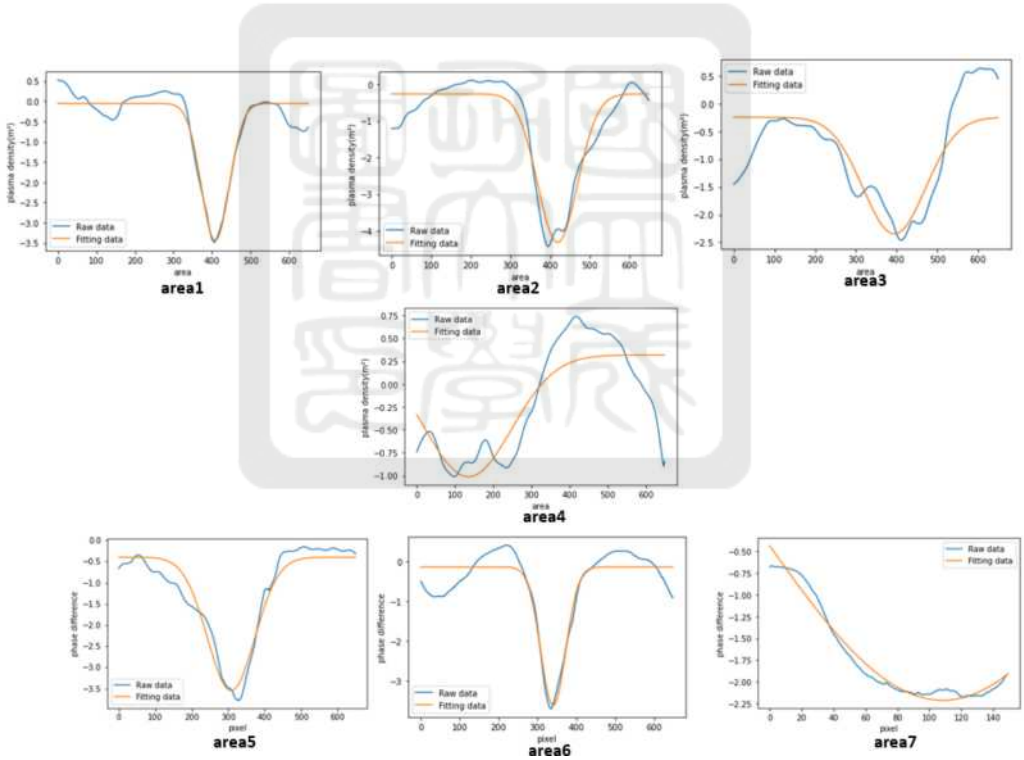

Figure 76: The fitting of each area 03/22 (585.5 ns).

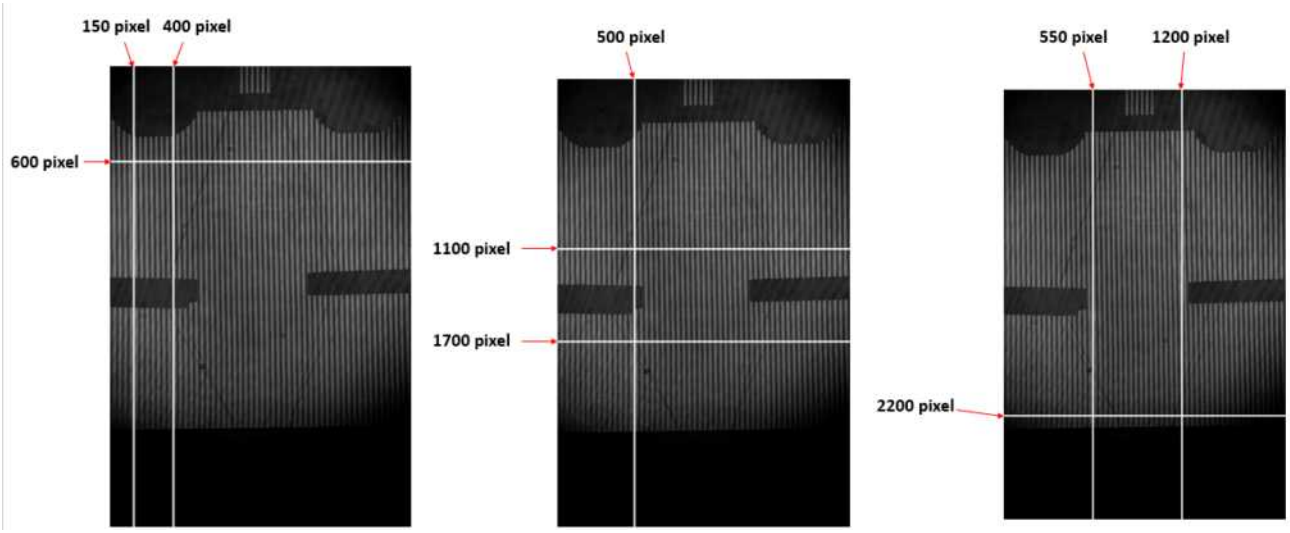

Figure 77: The cutting region for find the bound 03/28 (636.3 ns).

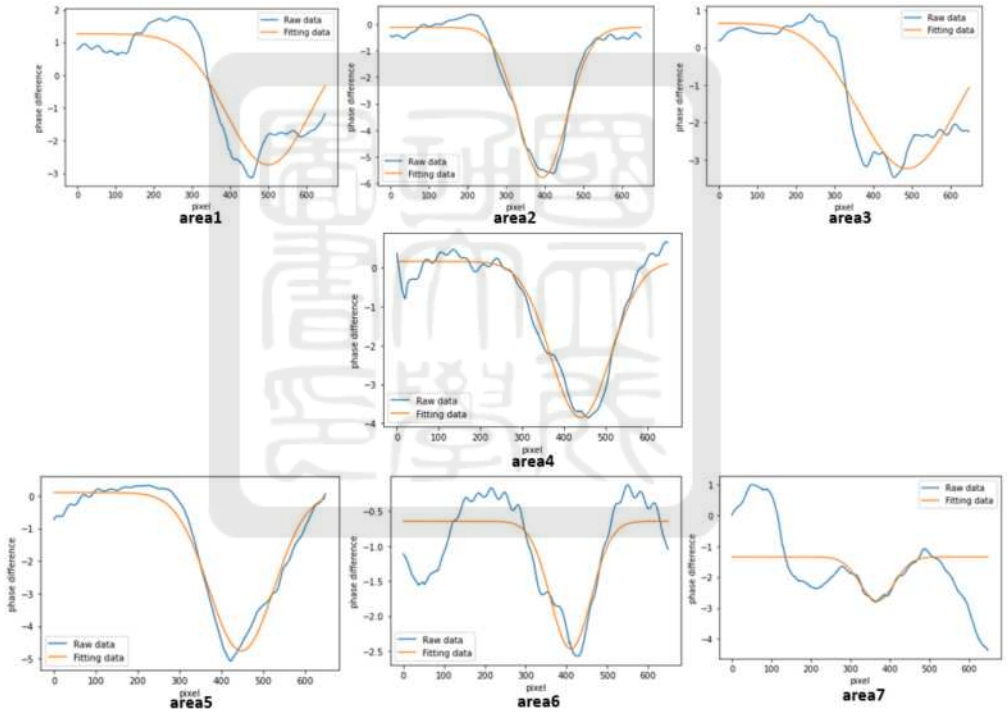

Figure 78: The fitting of each area 03/28 (636.3 ns).

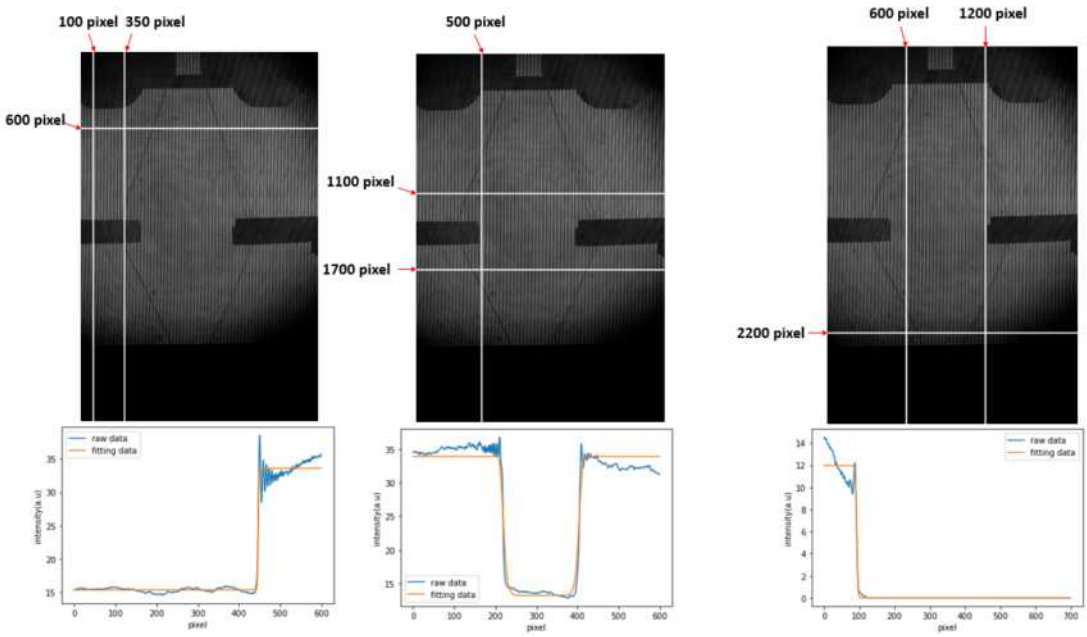

Figure 79: The cutting region for find the bound 03/29 (658.7 ns).

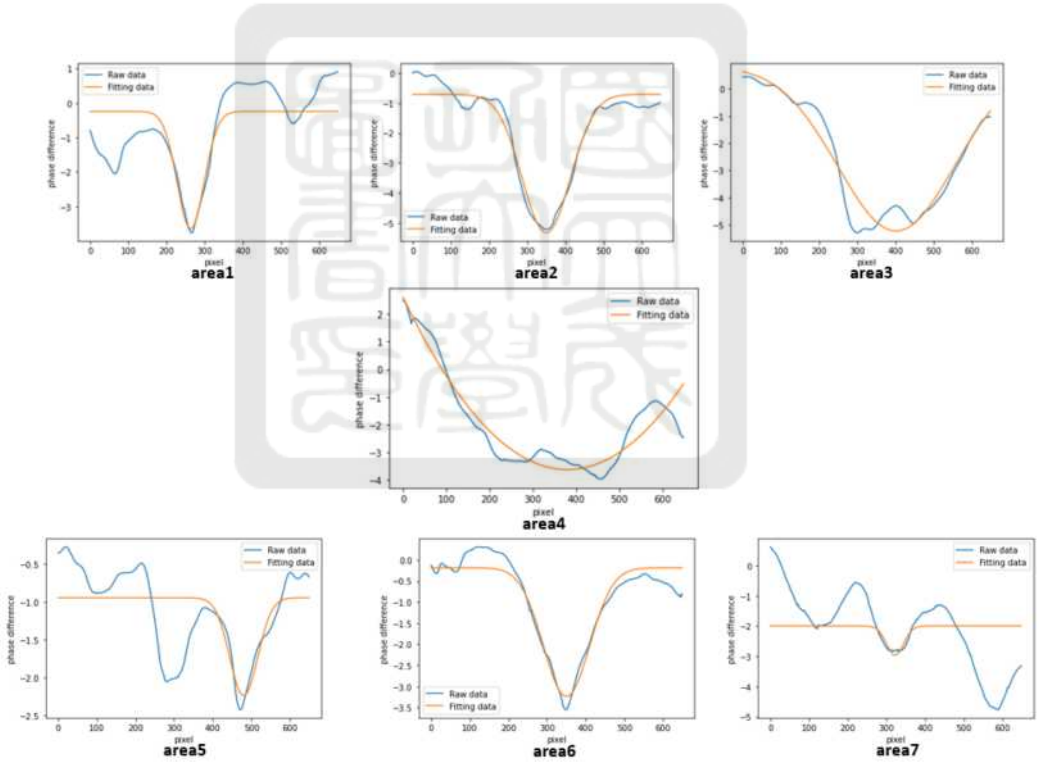

Figure 80: The fitting of each area 03/29 (658.7 ns).

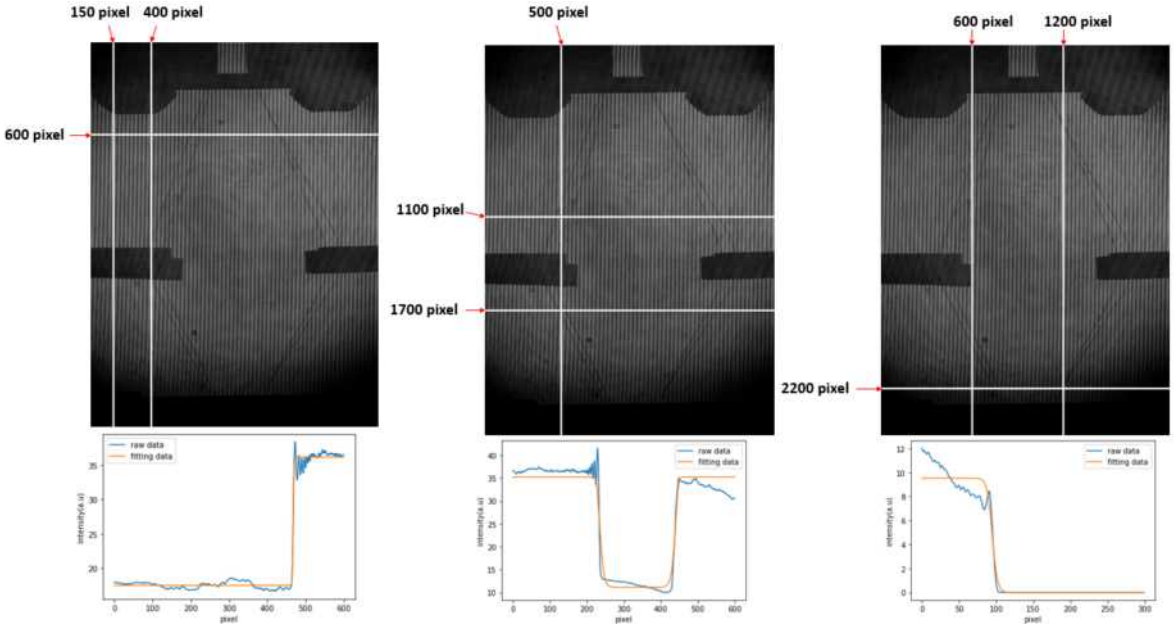

Figure 81: The cutting region for find the bound 03/30 (506.2 ns).

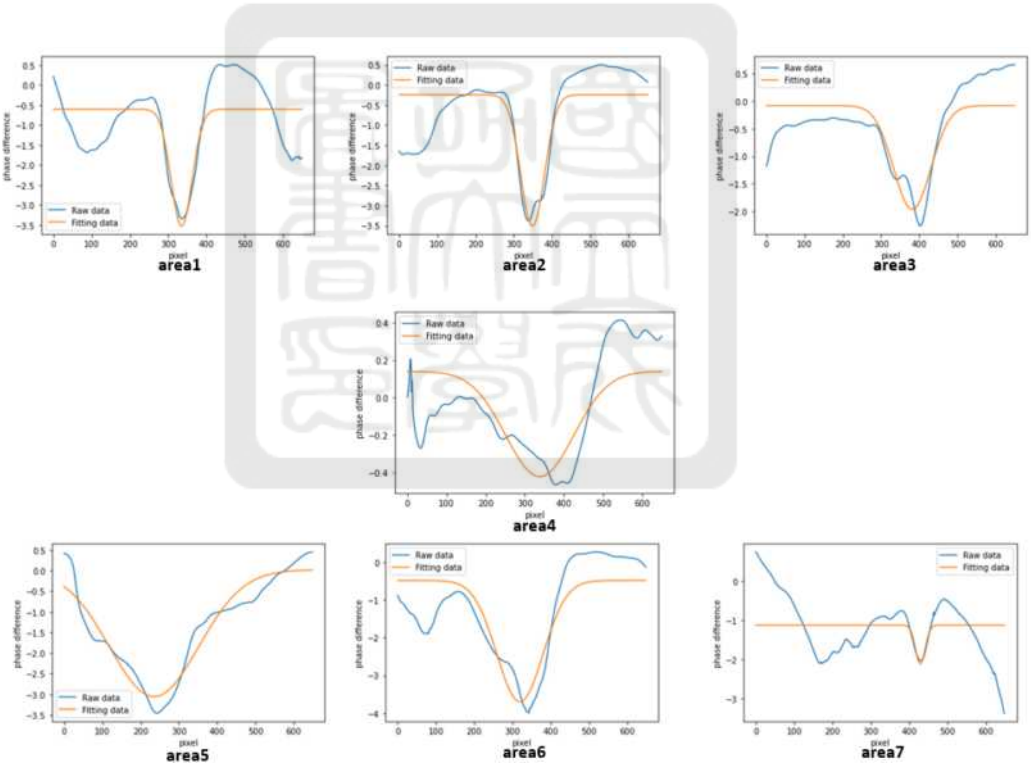

Figure 82: The fitting of each area 03/30 (506.2 ns).

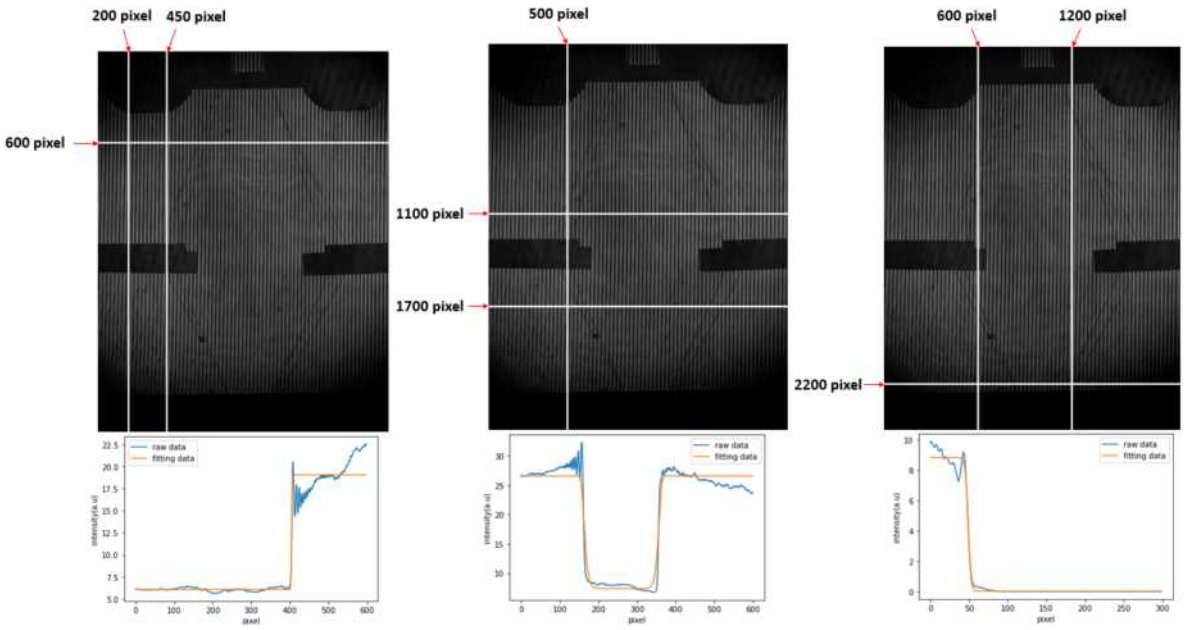

Figure 83: The cutting region for find the bound 04/07 (774.0ns).

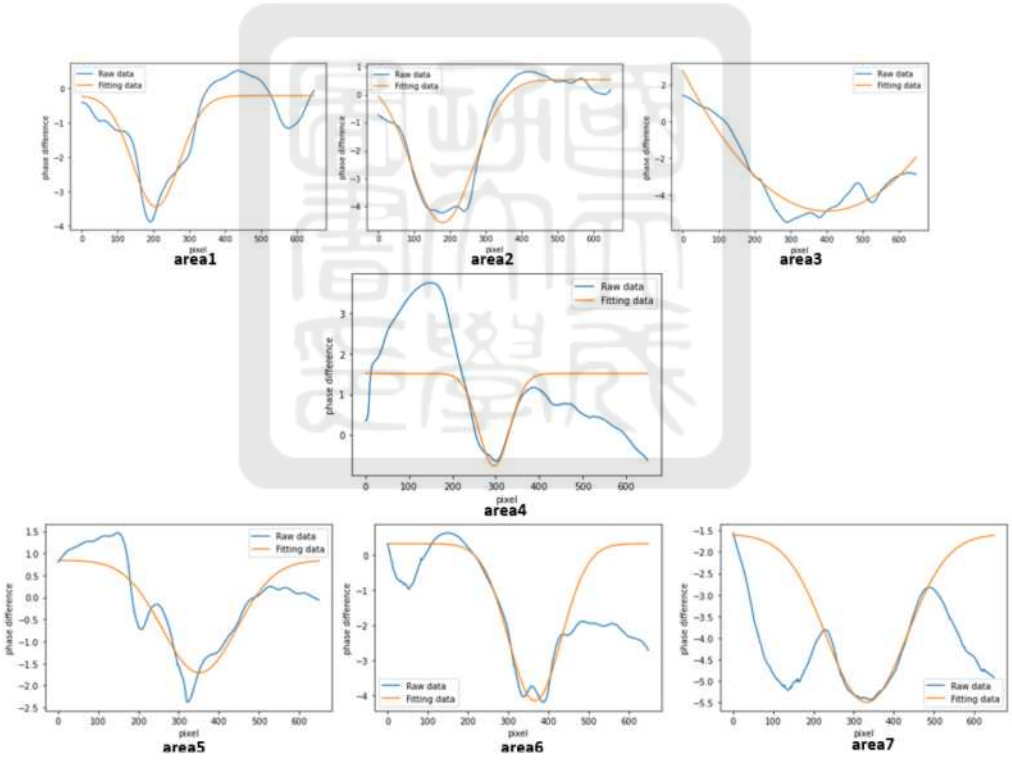

Figure 84: The fitting of each area 04/07 (774.0 ns).

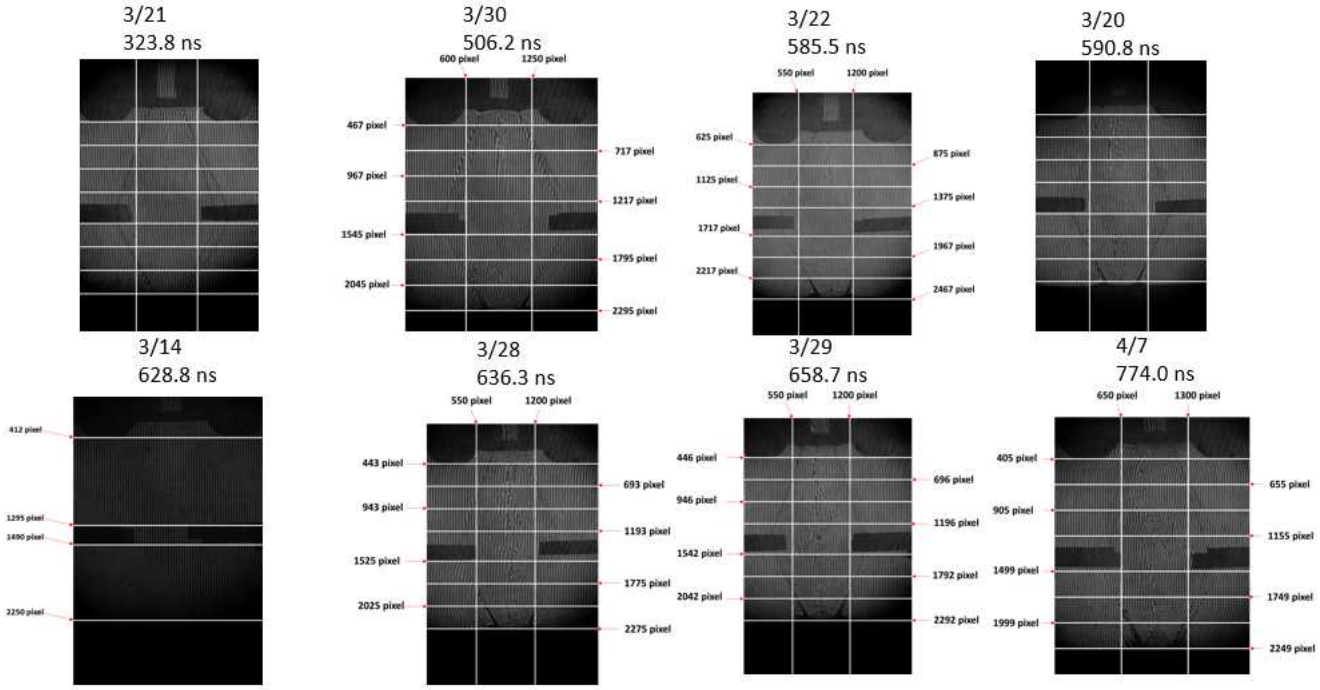

Figure 85: All data cut to 7 area.

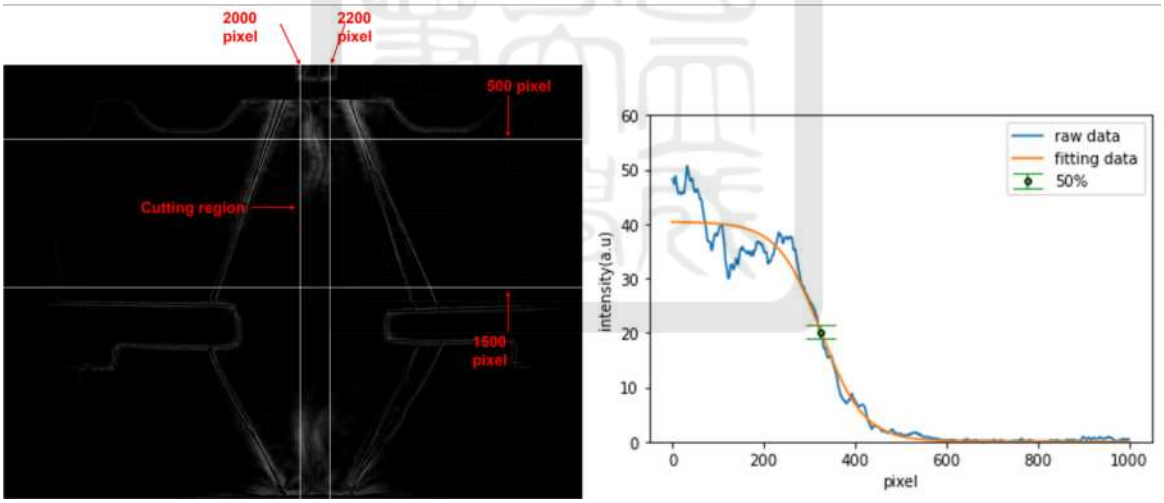

Figure 86: The length of the top plasma jet 03/21(323.8 ns).

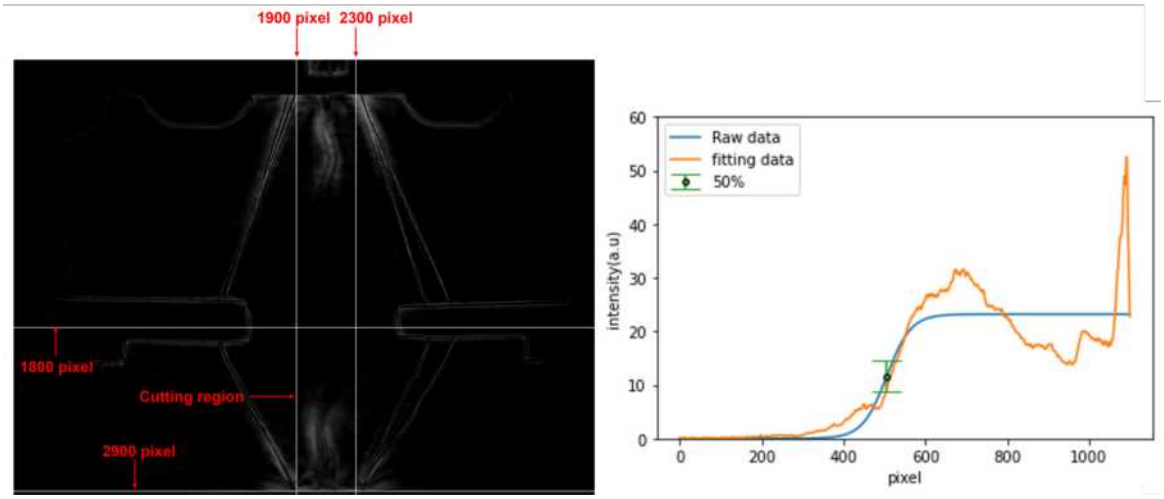

Figure 87: The length of the down plasma jet 03/21(323.8 ns).

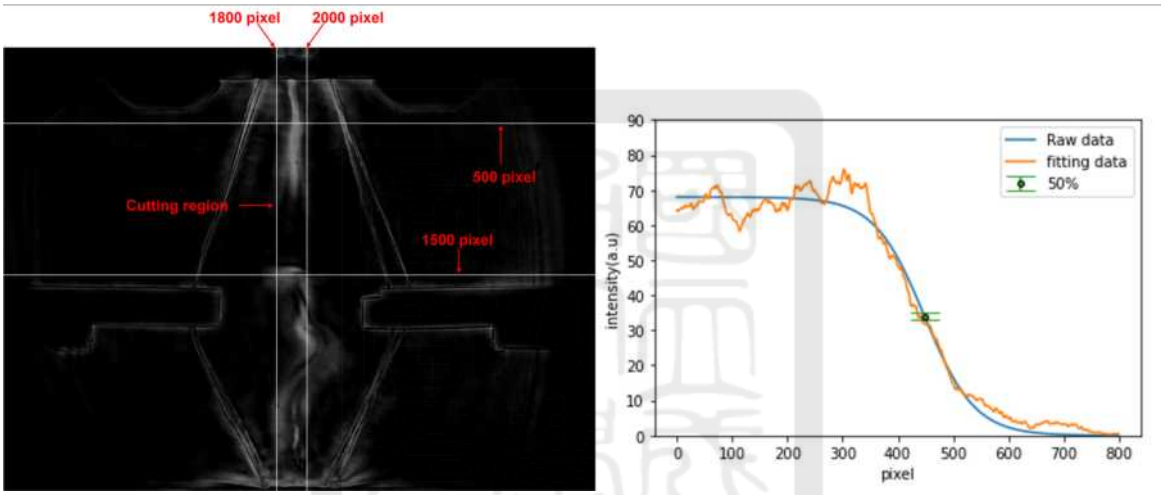

Figure 88: The length of the top plasma jet 03/15(370.7 ns).

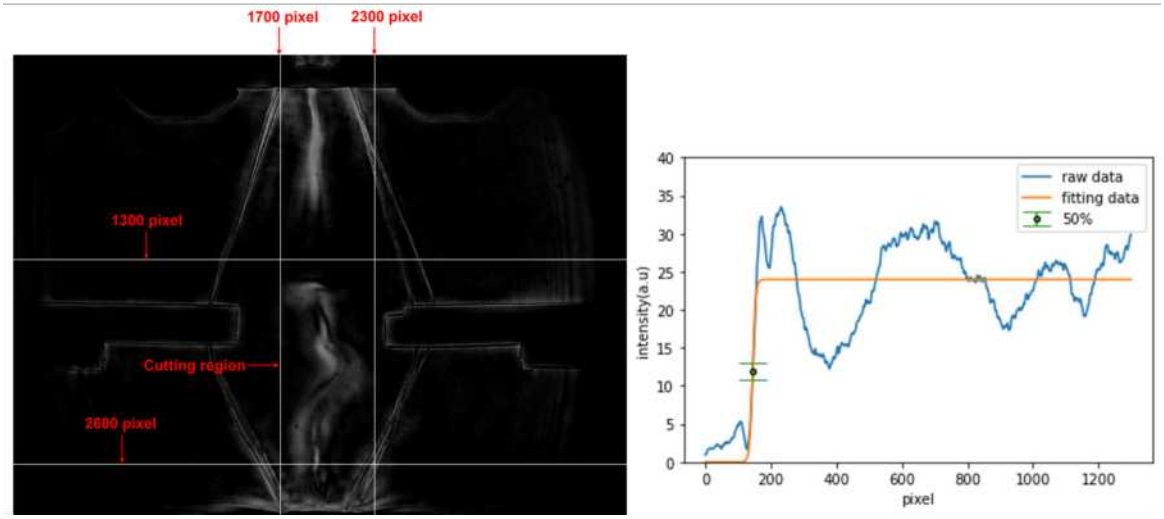

Figure 89: The length of the down plasma jet 03/15(370.7 ns).

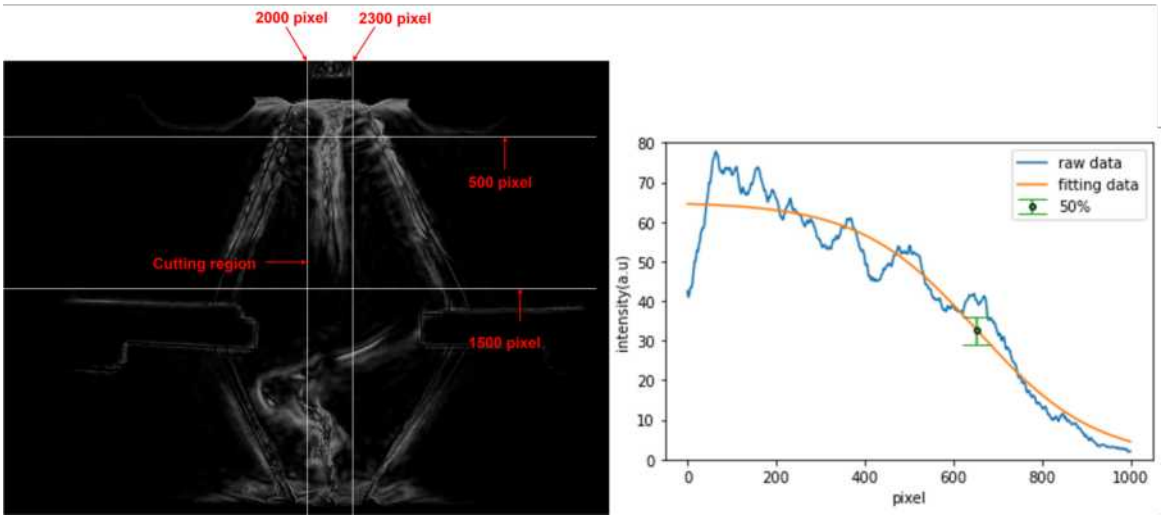

Figure 90: The length of the top plasma jet 03/30(506.2 ns).

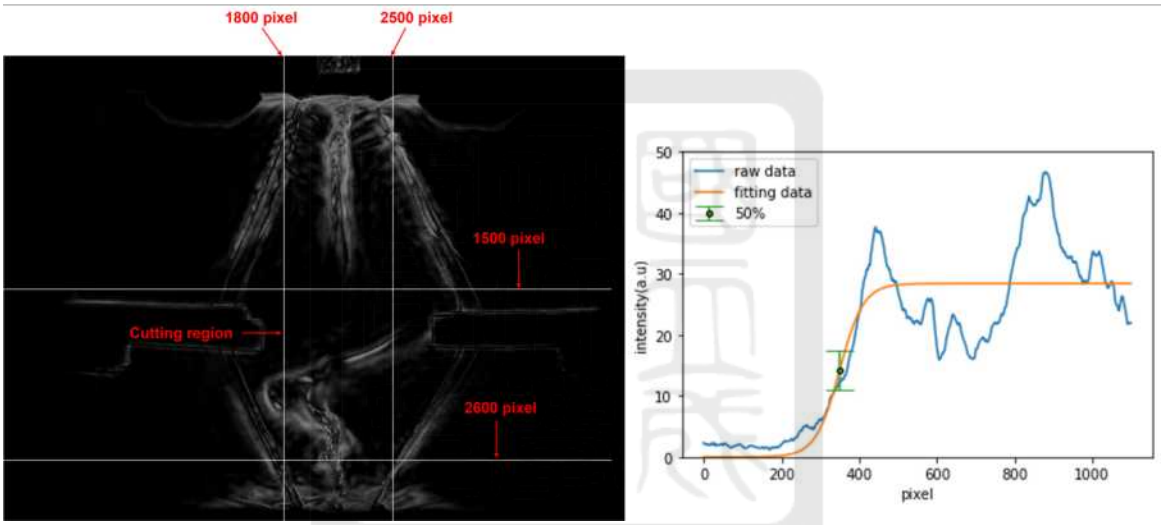

Figure 91: The length of the down plasma jet 03/30(506.2 ns).

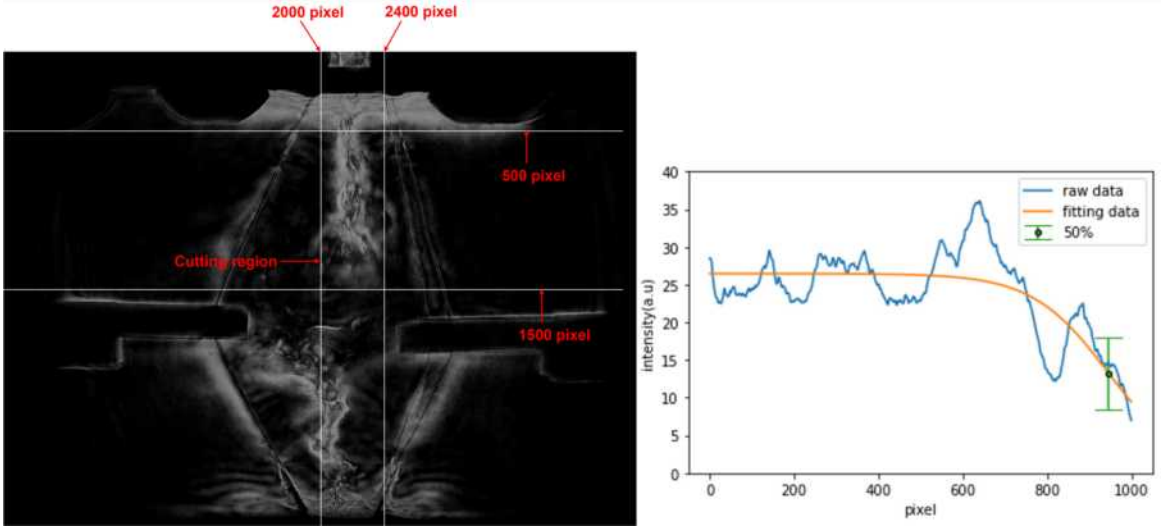

Figure 92: The length of the top plasma jet 03/22(585.5 ns).

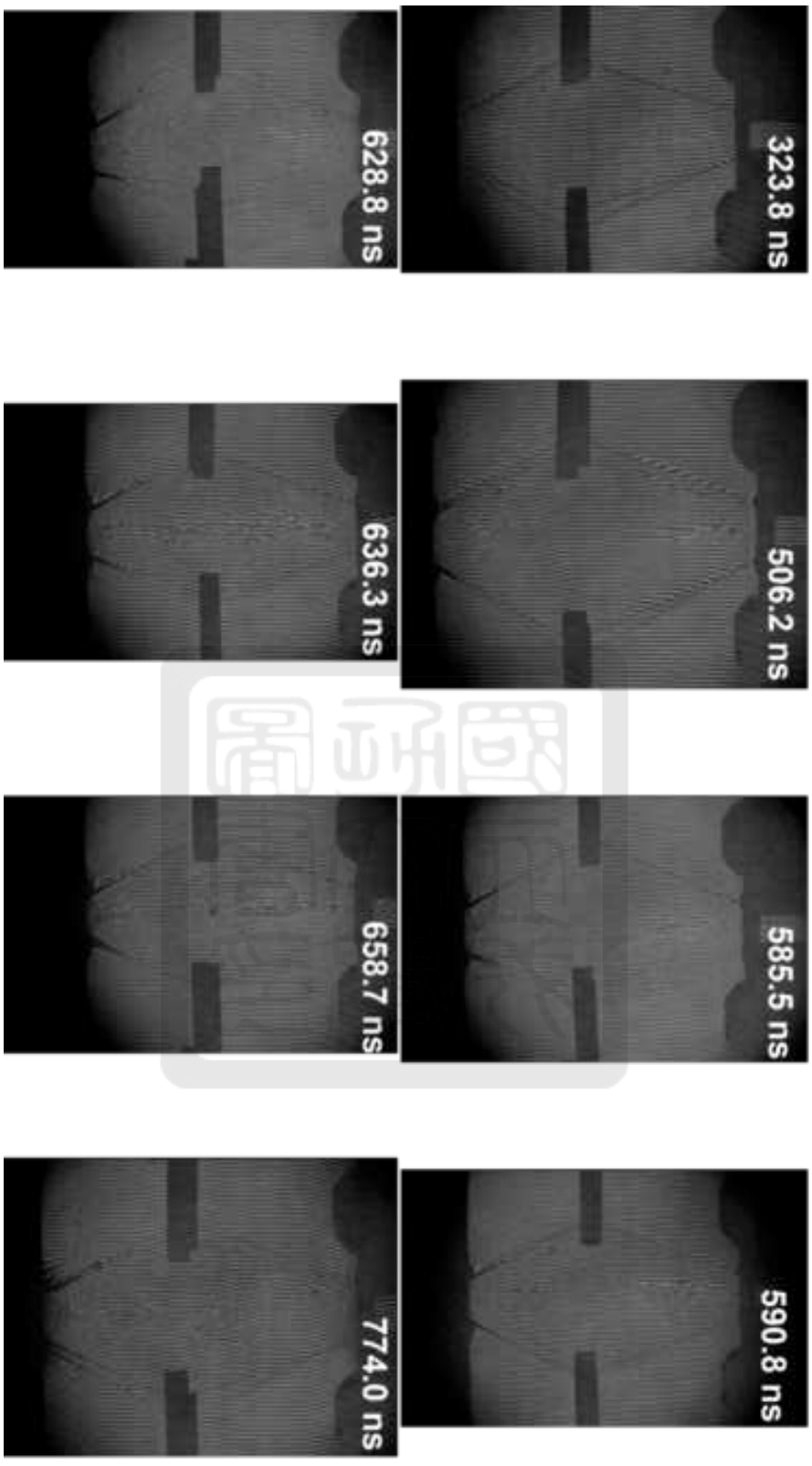

Figure 93: Interferometer images in different time.

A.9 The procedure of set up the non-rotating bi-conical-wire array

Bi-concial-wire array set up(10mm)

劉哲宇

2023/04

所需工具:剪刀，手套，鋁箔膠帶，六角板手組，鑷子，0.02 mm鎢絲，大張無塵紙，手電筒，bi-concial-wire array組合包。

1. 從防潮箱中取出鎢絲。
2. 戴上乳膠手套。
3. 取一張大張無塵紙放置於桌面。
4. 將4個top support 鎖入 chamber 外圈，如圖1紅圈所示。

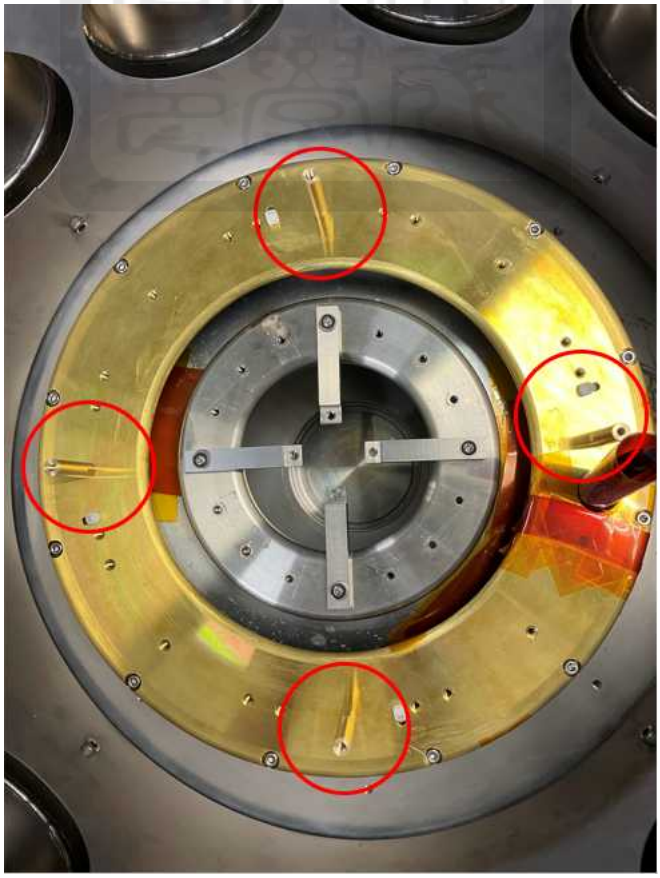

Figure 1: chamber with top support

5. 將組合好的 top wire support 及 top horizontal support 以top disk 朝上將其用螺絲固定於 top support 上，如圖2所示。

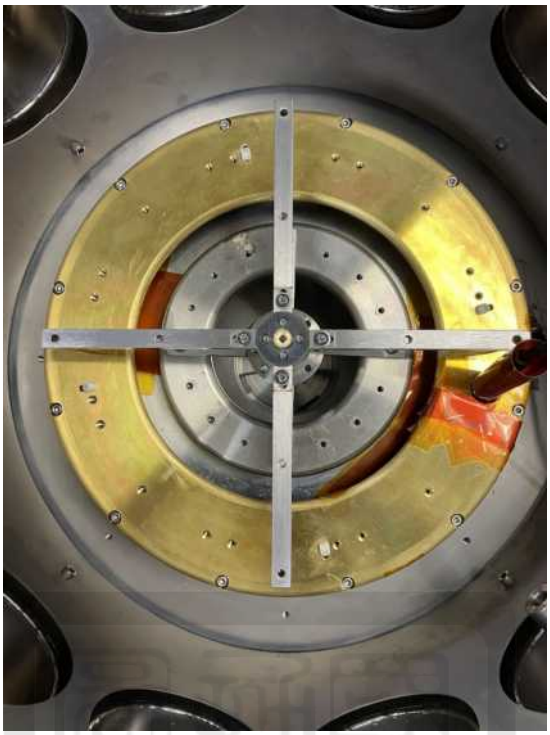

Figure 2: top support with top wire and horizontal support

6. 取出校正用原塊，如圖3所示。

Figure 3: 校正用原塊

7. 將校正用原塊以有凸起面朝上從側邊卡入 top wire support 中。

8. 一手壓著校正用原塊，另一手拿適合的六角板手，將固定top disk 螺絲如圖4紅圈所示略爲轉鬆後再鎖緊。

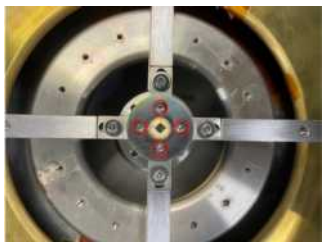

Figure 4: 固定top disk 螺絲

9. 將固定組合好的 top wire support 及 top horizontal support 螺絲鬆開並將其取下，放置於無塵紙上。

10. 將 bottom horizontal support 用螺絲固定於chamber內圈，如圖1內圈所示。

11. 將 bottom wire support 放置於 bottom horizontal support 上並將其用螺絲固定於 bottom horizontal support 上，如圖5所示，如無法四個螺絲皆鎖入，需調整 bottom horizontal support。

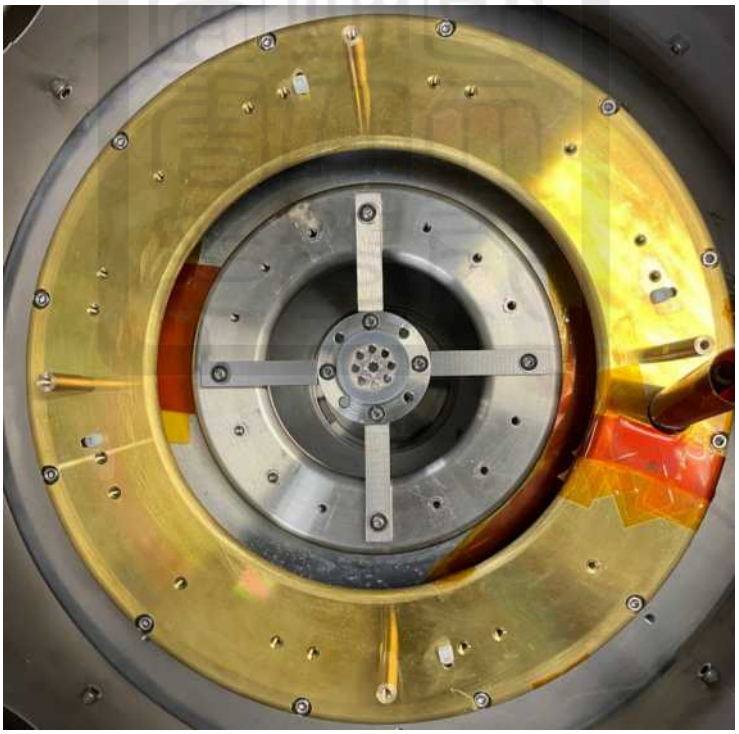

Figure 5: bottom wire support及bottom horizontal support

12. 將 bottom wire support 取下放置在無塵紙上。

13. 將輔助安裝支架及螺絲如圖6(a)所示，固定於 bottom wire support 上，如圖6(b)所示，共有4跟支架。

(a)	(b)
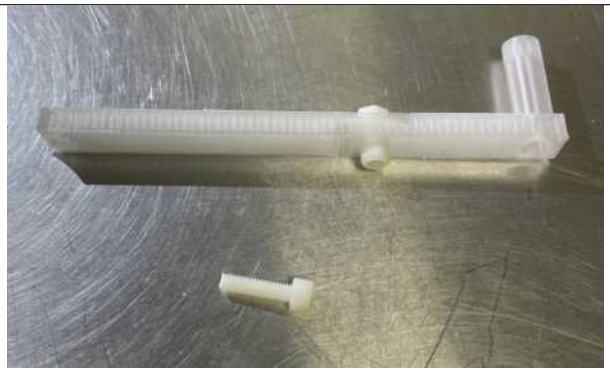	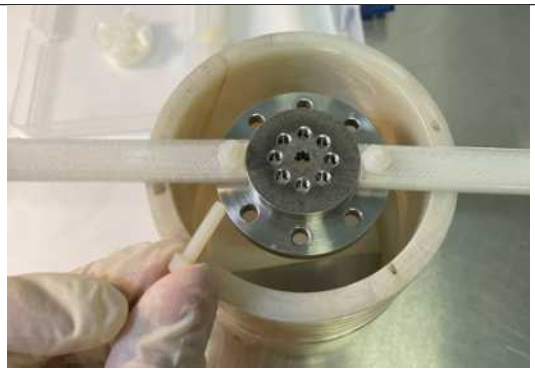

Figure 6: (a)輔助安裝支架及螺絲 (b)bottom wire support安裝輔助支架

14. 將固定組合好的 top wire support 及 top horizontal support 放置且固定於輔助安裝支架上，如圖7所示。

Figure 7: top horizontal support固定於輔助安裝支架

15. 剪取足夠長之鎢絲將其固定於鋁箔膠帶上，並用鑷子輕輕壓過如圖8所示。

Figure 8: 鎢絲固定於鋁箔膠帶

16. 將鋁箔膠帶固定於螺桿上，如圖9所示。

Figure 9: 箔膠帶固定於螺桿

17. 將鎢絲另一端也黏貼鋁箔膠帶如步驟15。

18. 一手拿取 middle support 如圖10(a)所示，一手拿取鎢絲黏貼鋁箔膠帶端，將螺桿穿

過 top disk 中間洞如圖10(b)紅圈所示以及middle support 的洞如圖(a)紅圈所示，再穿過 bottom wire support，將鋁箔膠帶黏貼於top horizontal support上如圖(b)紅色箭頭所示。

(a)	(b)
	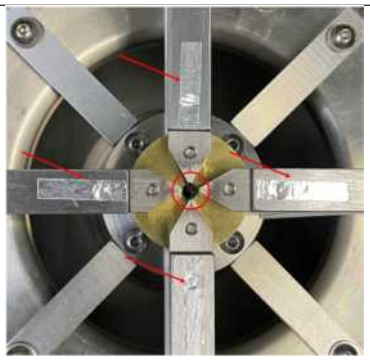

Figure 10: (a)middle support (b)top disk 中間洞

19. 用鑷子輕輕壓過鋁箔膠帶。

20. 重複步驟15~19直到4條鎢絲皆架設完畢

21. 將整組 bi-concial-wire array 放置於 bottom horizontal support上。

22. 並用螺絲將 bottom wire support 固定在 bottom horizontal support 上，如圖11所示。

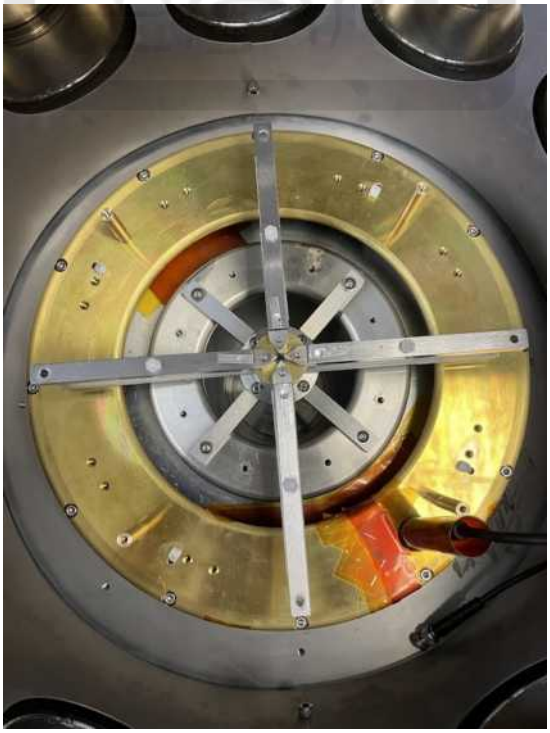

Figure 11: bi-concial-wire array放置

23. 將固定輔助安裝支架與 top horizontal support 的螺絲鬆開。

24. 將其旋轉並使 top horizontal support 放置於 top support 上。

25. 用螺絲將 top horizontal support 固定於 top support 上，如圖12所示。

Figure 12: top horizontal support 固定於 top support 上，輔助支架未拆

26. 以單手一隻手指按住如圖13紅色圈圈瑣事螺帽，一手指輕輕轉動下方螺絲，螺絲鬆動後先取出如圖13紅色箭頭所指處的螺絲。

Figure 13: 輔助支架螺帽位置

27. 繼續以單手一隻手指按住如圖13紅色圈圈瑣事螺帽，一手指輕輕轉動下方螺絲直到螺絲脫離螺帽，讓螺絲掉入 chamber 下方空洞，如螺帽可取出便將其取出，不便取出也可使其掉落 chamber 下方空洞。

28. 重複步驟26~27直到4個扶助安裝支架皆拆下。

29. 以手電筒照射鎢絲有無在對應的 bottom wire support 溝槽內，將梅在溝槽內的鎢絲用最小的六腳板手輕輕勾入對溝漕內。

A.10 The store of the data

Experiment	Storage path
The eight-stage high-voltage pulse generator	NAS:Experments\2021_cliu2
Non-rotating bi-conical-wire array	NAS:Experments\2021_cliu2
Analysis program(python)	NAS:Experments\2021_cliu2\analysis

A.11 The vender of all components

Component	Vender	Note
Rasberry Pi 4B 8G	蝦皮-oursteamtw	
Raspberry Pi HQ-camera Module	蝦皮-oursteamtw	
Rasberry Pi HDMI 線	蝦皮-oursteamtw	
MOSFET(TSM1NB60)	RS	要注意RS網頁上產品會與規格書不相符
高壓電容	RS	
鋁版	三川金屬	要切剛好的尺寸要先講，不然老闆會多切點送你
鎢絲	露天	騰豐金屬
機械加工	蒔岱工業	
電路板	南一電子	
錫線	南一電子	最好帶用完的去比對，這個參雜的比例比較好用